Ruoyu Wang

Integrierte Planare Antennen und Technologien für Millimeterwellen-Anwendungen

Integrated Planar Antenna Designs and Technologies for Millimeter-Wave Applications

UNIVERSITÄT PADERBORN
Die Universität der Informationsgesellschaft

Integrated Planar Antenna Designs and Technologies for Millimeter-Wave Applications

Von der Fakultät für Elektrotechnik, Informatik und Mathematik
der Universität Paderborn

zur Erlangung des akademischen Grades

Doktor der Ingenieurwissenschaften (Dr.-Ing.)

genehmigte Dissertation

von

M.Sc. Ruoyu Wang

Erster Gutachter: Prof. Dr.-Ing. Christoph Scheytt
Zweiter Gutachter: Prof. Dr.-Ing. Jörg Schöbel

Tag der mündlichen Prüfung: 16.12.2014

Paderborn 2015

Diss. EIM-E/307

UNIVERSITÄT PADERBORN
Die Universität der Informationsgesellschaft

Abstract:

Integrated Planar Antenna Designs and
Technologies for Millimeter-Wave Applications

des Herrn Ruoyu Wang

This thesis investigates the design and realization of integrated planar antennas for millimeter-wave applications. The state-of-the-art antenna integration and packaging technologies are extensively studied, and an antenna design flow is proposed.

A number of integrated antenna designs by applying different integration approaches and technologies, i.e. on printed circuit board (PCB), on-chip and in Benzocyclobutene (BCB) above-wafer process, are presented. The designs target not only high performance, but also the practical considerations of low-cost, feasibility, better reliability, and good reproducibility. They cover the industrial, medical, and scientific (ISM) bands of 60 GHz, 122 GHz, and 245 GHz in the millimeter-wave range with outstanding performance in a low-cost fashion by applying innovative, appropriate integration methods and sophisticated design. By applying the localized backside etching (LBE) process the presented on-chip antennas achieve measured peak gains of 6–8.4 dBi for above 100 GHz applications with simulated efficiencies of 54–75%. These figures are comparable to that of on-board or in-package antennas. To the best of the author's knowledge, the achieved gain of 7.5–8.4 dBi in the band of 124–134 GHz for the 130 GHz on-chip double folded dipole antenna is the highest reported result to date for planar on-chip antennas on low-resistivity silicon technologies.

System demonstrators with integrated antennas are realized and measured. The 60 GHz demonstrator with on-PCB differential bunny-ear antenna and a novel bond-wire compensation scheme achieves a data rate of 3.6 Gbit/s over 15 meter distance, which was the best reported analog front-end without beamforming function in silicon technology regarding both the data rate and transmission distance at the time of its publication. A 245 GHz single-channel transmitter and a single-channel receiver with integrated on-chip antennas are also demonstrated. An effective isotropic radiated power (EIRP) of 7–8 dBm is achieved for the transmitter, which is the highest reported value at 245 GHz for a SiGe transmitter with a single antenna so far. Furthermore, the receiver has the highest reported integration level for any 245 GHz SiGe receiver. A 245 GHz 4-channel-transmitter array with integrated on-chip antenna array is also realized to achieve spatial power combining, which offers 11 dB higher EIRP than a single-channel transmitter.

From the presented results of the thesis it is feasible to realize high performance integrated planar antennas in the entire millimeter-wave range and beyond in a cost-effective fashion.

UNIVERSITÄT PADERBORN
Die Universität der Informationsgesellschaft

Zusammenfassung der Dissertation:

Integrierte Planare Antennen und

Technologien für Anwendungen im Millimeterwellen-Bereich

des Herrn Ruoyu Wang

Diese Arbeit untersucht den Entwurf und die Realisierung von integrierten planaren Antennen für Anwendungen im Millimeterwellen-Bereich. Der Stand der Technik wird ausführlich untersucht und ein Entwurfsablauf vorgeschlagen.

Mehrere Antennenentwürfe werden vorgestellt, die jeweils verschiedene Integrationsansätze und Technologien verwenden, z.B. Integration auf der Platine, auf dem Chip, und mit einem „Above-Wafer-Prozess" mit Benzocyclobuten (BCB). Die Entwürfe zielen nicht nur auf möglichst gute elektrische Leistungsdaten, sondern berücksichtigen weitere wichtige Gesichtspunkte, wie niedrige Kosten, Machbarkeit, verbesserte Zuverlässigkeit und Reproduzierbarkeit. Die Antennen decken die ISM-Frequenzbänder im Millimeterwellen-Bereich bei 60 GHz, 122 GHz und 245 GHz ab und erreichen dabei exzellente Leistungsdaten bei geringen Herstellungskosten, was auf innovative, angepasste Integrationsmethoden und spezielle Entwurfstechniken zurückzuführen ist. Durch lokale Rückseitenätzung („localized backside etching", LBE) erreichen die vorgestellten on-chip Antennen gemessene Verstärkungen von 6 bis 8.4 dBi für Frequenzen oberhalb von 100 GHz mit simulierten Effizienzen von 54 bis 75%. Diese Werte sind vergleichbar mit off-chip Antennen, die auf Platinen- oder mit einem System-In-Package-Ansatz realisiert werden. Nach Wissen des Autors ist der Antennengewinn von 7.5 bis 8.4 dBi in einem Frequenzband von 124 bis 134 GHz für eine on-chip Faltdipol-Antenne das beste bis dato erzielte Ergebnis für planare on-chip Antennen auf niederohmigem Siliziumsubstrat.

System-Demonstratoren mit integrierten Antennen wurden implementiert und gemessen. Der 60 GHz Demonstrator-Transceiver mit planarer Bunny-Ear-Antenne, integriert auf der Platine, und einer neuartigen Bonddraht-Kompensationsmethode erreichten eine Datenrate von 3.6 Gbit/s über 15 Meter Distanz. Dies war zum Zeitpunkt der Veröffentlichung das beste Ergebnis für Ein-Antennen-Transceiver in Siliziumtechnologie sowohl hinsichtlich Datenrate als auch Distanz. Ein 245 GHz einkanaliger Transmitter und einkanaliger Empfänger mit integrierten on-chip Antennen würde ebenfalls demonstriert. Eine effektive isotropische Abstrahlleistung (EIRP) von 7 bis 8 dBm wurde erreicht, welches den höchsten publizierten Wert für einen siliziumbasierten Sender mit Einzelantenne bis heute darstellt. Ebenso wurde ein 245 GHz 4-kanaliger Sender mit einem on-chip Antennen-Array demonstriert, um noch höhere Leistungen durch Leistungsüberlagerung in der Luft zu erreichen. Dabei wurde ein EIRP erreicht, das 11 dB höher als das EIRP der einkanaligen Lösung war.

Mit den Ergebnissen dieser Arbeit ist es möglich, planare integrierte Antennen mit sehr guten Leistungsdaten für den gesamten Millimeterwellen-Bereich und darüber hinaus bei geringen Herstellungskosten zu realisieren.

Integrated Planar Antenna Designs and Technologies for Millimeter-Wave Applications

Ruoyu Wang

Inhaltsverzeichnis

List of Acronyms

AUT	Antenna Under Test
BCB	Benzocyclobutene
BER	Bit Error Rate
BEOL	Back-End-of-Line
COB	Chip-on-Board
CPW	Coplanar Waveguide
CTE	Coefficient of Thermal Expansion
DRA	Dielectric Resonator Antenna
DRIE	Deep Reactive Ion Etching
EIRP	Effective Isotropic Radiated Power
EM	Electromagnetic
FER	Frame Error Rate
FEM	Finite Element Method
FIT	Finite Integration Technique
G-S-G	Ground-Signal-Ground
GCPW	Grounded Coplanar Waveguide
HD	High-Definition
ISM Band	Industrial, Scientific and Medical Band
I/O	Input/Output
IF	Intermediate Frequency
LBE	Localized Backside Etching
LOS	Line-of-Sight
LTCC	Low Temperature Co-fired Ceramic
LGA	Land-Grid-Array
LCP	Liquid Crystal Polymer
LNA	Low-Noise Amplifier
LO	Local Oscillator

mm-Wave	Millimeter-Wave
MCM-D	Multichip Module with Deposited Interconnects
OFDM	Orthogonal Frequency Division Multiplexing
PEC	Perfectly Electric Conducting
PMC	Perfectly Magnetic Conducting
PCB	Printed Circuit Board
PA	Power Amplifier
PTFE	Polytetrafluoroethylene
PLL	Phase-Locked Loop
PHY	Physical Layer
QFN	Quad Flat No-lead
QoS	Quality of Service
RFIC	Radiofrequency Integrated Circuit
RX	Receiver
SiGe	Silicon-Germanium
SOL	Short-Open-Load
SNR	Signal to Noise Ratio
SMT	Surface Mount Technology
SEM	Scanning Electron Microscope
TSVs	Through Silicon Vias
TEM	Transverse Electromagnetic
TM	Transverse Magnetic
TE	Transverse Electric
TX	Transmitter
VCO	Voltage Controlled Oscillator
WPAN	Wireless Personal Area Networks

1 Introduction

Wireless technology has changed our world significantly, and has become an indispensable part of our daily life. The number of handheld wireless devices and mobile internet users is growing very rapidly, and many people use their smart phones or tablet computers instead of newspaper, TV or PC for receiving news, entertainment, social networking, and so on at any time in any place. Wireless technology is not only used in communications, but also in other applications such as radar, any kind of sensing, and imaging. There is continuously increasing demand from the market for more broadband wireless systems, which enable higher data rate transmission for high-definition (HD) multimedia applications, and high resolution and accuracy for radar, sensing and imaging applications. Importantly, the mass products have to be implemented in a highly-integrated, low-power, and low-cost fashion. The requirements are beyond what the wireless systems in the market of today can offer, especially with respect to bandwidth. This creates great opportunity for the research in the millimeter-wave (mm-Wave) frequency bands (30–300 GHz) which can offer much higher bandwidth than traditional wireless systems operating in frequency bands below 10 GHz.

1.1   Millimeter-Wave Systems and Antenna Integration

The tremendous improvements of the high-speed silicon technologies, e.g. silicon-germanium (SiGe), have made continuous progress towards ever higher transistor cutoff frequencies, e.g. f_T/f_{max}=300/500 GHz in IHP's 0.13 µm BiCMOS (SG13G2) technology [1]. Nowadays all components for transceivers operating in the mm-Wave frequency range can be realized in silicon technologies with fairly good electrical performance [2] [3]. Taking the outstanding advantages of the silicon technologies in terms of low-cost and high-integration level mm-Wave systems are becoming attractive and affordable for consumer mass products. Promising applications are high data rate wireless personal area networks (WPANs) at 60 GHz, automotive radar at 77 GHz, imaging at 94 GHz, various evolving applications at the license-free industrial, scientific and medical (ISM) bands of 122 GHz and 245 GHz, etc. However, these systems require not only the radiofrequency integrated circuits (RFICs) but also a wide range of high-quality passive components operating in the mm-Wave range, especially the antennas and their interconnects for system integration. Apparently, conventional mm-Wave components such as horn antennas and waveguides cannot meet the basic requirements for mass consumer products due to their excessively high price and heavy weight in spite of their superior performance. The integrated planar antennas are well-known for their low profile, low weight, low-cost, and good compatibility with the active components or RFICs, thus representing the most suitable choice for such systems.

Integrated antennas are crucial components in mm-Wave systems. As frequency increases the link budget becomes more challenging not only due to the high free-space loss, but also due to other factors like limited output power of the transmitter and higher noise figure in the receiver. For commercial handset applications the power consumption should be at a reasonably low level to prolong the battery life. Therefore, antennas with a moderately high gain and high efficiency operating in sufficient bandwidth are generally required as well as a compact size, low-cost, and ease of use. Defining reasonable specifications and choosing the most appropriate antenna type should be done at the first phase of a design.

There are challenges from several aspects in mm-Wave integrated planar antenna designs. The substrate properties like the loss tangent and dielectric constant offered by the manufacturers are usually only measured up to lower frequencies, e.g. 10 GHz. The values may change considerably at the mm-Wave frequencies. Applying the inaccurate values in the design may result in a shift of resonance frequency, and hence performance degradation in the targeted frequency band. In addition, the problem of substrate waves will be more pronounced when the substrate becomes electrically thick, which can reduce the radiation efficiency and cause spurious radiation. The integration of antenna into a mm-Wave system also takes a vital role, because the interconnects between the antenna and the input/output (I/O) of the RFIC as well as the packaging materials and any other structures (e.g. a dielectric lid of a package) in the vicinity of the antenna could introduce parasitic effects (causing impedance mismatching and extra losses), and degrade the radiation performance. The parasitic effects will generally become more pronounced as the frequency increases. In practice the antenna integration requires very sophisticated designs and optimizations [4]–[7], which take all the extra effects into account to minimize design cycles. In addition, higher frequencies (smaller wavelengths) demand high-precision machining, accurate alignment, and high-resolution photolithography. All the challenges and high efforts involving in the integrated antenna design, and manufacturing of high-quality packaging and assembly will be translated to higher cost compared to their low frequency counterpart. The measurement of mm-Wave planar antenna is very challenging, too. Conventionally, the antenna under test (AUT) is connected to the measurement setup by a coaxial cable or a waveguide connector. However, the feature sizes of these types of connectors are too large for the planar mm-Wave antennas, especially for the on-chip antennas. Microwave probe based measurement setup with special calibration procedure has to be used for the on-chip antenna characterizations. Since the shielding of a microwave probe is worse than that of a conventional connector for antenna measurement, the spurious radiation from the probe will limit the accuracy of the measurement [8]–[10].

1.2   Outline of the Thesis

The target of this thesis is to realize mm-Wave integrated planar antennas by applying the most appropriate integration approaches and technologies, which are capable to cover the complete mm-Wave frequency range with outstanding performance in a low-cost fashion.

Chapter 2 will briefly introduce the most important figure-of-merits to describe the radiation performance of the designed antennas with emphasis on their effects in a wireless system. Some basic antenna models are theoretically studied, which offer insight into the operation principle of the designed antennas, and the direction for optimizations. The commonly used approaches to characterize the substrate properties are reviewed. The excitation and propagation of the substrate waves are studied. The microwave probe based antenna measurement setup is described. A discussion of various state-of-the-art antenna integration and packaging technologies is given in terms of the main concerns of feasibility, performance, reliability, cost, etc. In the end of this chapter a design procedure and methodology for the integrated planar mm-Wave antennas is proposed.

In chapter 3 integrated PCB (printed circuit board) antenna designs for 60 GHz applications are presented. The dielectric constant of low-cost RF substrates is characterized by transmission line method in wideband, and further verified by patch resonators around 60 GHz. The mm-Wave interconnect technologies of bond-wire and flip-chip are experimentally studied. A novel double-bonding structure is proposed to compensate the parasitic effects introduced by the bond-wire in a large bandwidth. The demonstrators with the designed antennas and the bond-wire compensation scheme are shown to achieve very good performance.

Several integrated on-chip antennas based on SiGe BiCMOS technologies are presented in chapter 4. The technology is overviewed. The localized backside etching (LBE) process, which is available in all IHP's technologies as well as other semiconductor technologies, is applied to improve the performance of the on-chip antennas. Different antenna structures are investigated to achieve high gain, mechanical robustness, better immunity to fabrication tolerances, and more compact size. The 245 GHz transceiver with integrated on-chip antenna is demonstrated.

Chapter 5 presents on-chip antenna designs by applying wafer-level integration technology. The polymer material of Benzocyclobutene (BCB) is deposited on the SiGe BiCMOS wafer as a post-wafer process. The antennas are realized in the thick copper layers in the BCB with ground shielding, which shields the antennas from the lossy silicon. In this way the radiation efficiency of the antennas is considerably higher than that of antennas realized on ordinary low-

resistivity silicon. The critical parameters for on-chip antenna designs with on-chip ground shielding are investigated. The interconnects among the metal layers are also experimentally verified, which have low parasitic effects, low loss, and very tight fabrication tolerance.

Chapter 6 will conclude the works in this thesis, and an outlook of the future research is also proposed.

1.3   Main Contributions

The main contributions of this thesis are the following:

- Design of high gain integrated PCB antennas on very low-cost RF substrate for the ISM band of 60 GHz applications. A differential bunny-ear antenna with end-fire radiation and a 4-element patch array antenna with broad-side radiation have been designed, manufactured, and measured [11]. They show excellent performance in IHP's transceiver demonstrators [12] [13]. The demonstrator with differential bunny-ear antenna has achieved a world record for 60 GHz front-ends in silicon technology without beamforming function regarding both the data rate and transmission distance at the time of its publication [14].

- Introduction of a novel double-bonding structure for compensating the parasitic effects introduced by bond-wire to improve the chip-to-antenna matching thus reducing the losses from the interconnects. This approach works well and reliable up to 80 GHz by using common wedge bonder and cheap normal PCB fabrication technology [15].

- Extensive study and investigation of on-chip antennas based on silicon BiCMOS process for above 100 GHz applications. Different antenna structures have been designed and characterized to achieve high gain, mechanical robustness, better immunity to fabrication tolerances, and more compact size. By applying LBE process, which is a standard process for the formation of through silicon vias (TSVs) in CMOS technology, I achieved very good performance of the on-chip antennas which compares favorably with the state-of-the-art designs [16]. To the best of my knowledge, the achieved gain of 7.5–8.4 dBi in the band of 124–134 GHz for the 130 GHz double-dipole on-chip antenna is the highest reported result for planar on-chip antennas in low-resistivity silicon technologies to date. I applied for an international patent for the double folded dipole on-chip antenna with surrounded air trenches, and it is pending [17]. The single-channel 245 GHz transmitter and single-channel receiver with on-chip antennas show outstanding performance, demonstrating the advantage of system-on-chip [18]–[20]. The single-channel transmitter has an effective isotropic radiated pow-

er (EIRP) of 7–8 dBm at 245 GHz, which is the highest reported result for a SiGe transmitter with single antenna at this frequency so far [18]. The receiver has the highest reported integration level for any SiGe receiver at 245 GHz [19]. The 245 GHz 4-channel-transmitter array with integrated on-chip antenna array offers 11 dB higher EIRP than a single-channel transmitter by spatial power combining [21].

- Design of antennas by using BCB above BiCMOS wafer process. The BiCMOS wafer was finalized without any change from the original process flow. The critical parameters for on-chip antenna designs with on-chip ground shielding are investigated. The antenna and the interconnects have been characterized, and proven reproducible in performance. The radiation efficiency is considerably higher than that of antennas realized on ordinary low-resistivity silicon [22]. This provides one promising choice for one-chip solutions for above 100 GHz applications.

References

[1] http://www.ihp-microelectronics.com/en/services/mpw-prototyping/sigec-bicmos-technologies.html

[2] J. C. Scheytt, Y. Sun, K. Schmalz, and R. Wang, "SiGe BiCMOS transceivers, antennas, and ultra-low-cost packaging for the ISM bands at 122 and 245 GHz," *Microwave Symposium Digest, 2012 IEEE MTT-S International*, pp. 1-3, Jun. 2012.

[3] J. C. Scheytt, Y. Sun, K. Schmalz, Y. Mao, R. Wang, W. Debski, and W. Winkler, "Towards mm-wave system-on-chip with integrated antennas for low-cost 122 and 245 GHz radar sensors," *Silicon Monolithic Integrated Circuits in RF Systems, 2013 IEEE 13th Topical Meetings on*, pp. 246-248, Jan. 2013.

[4] S. Beer, and T. Zwick, "122 GHz antenna-integration in a plastic package based on a flip chip interconnect," *Microwave Workshop Series on Millimeter Wave Integration Technologies, 2011 IEEE MTT-S International*, pp. 37-40, Sep. 2011.

[5] S. Beer, H. Gulan, M. Pauli, C. Rusch, G. Kunkel, and T. Zwick, "122-GHz chip-to-antenna wire bond interconnect with high repeatability," *Microwave Symposium Digest (MTT), 2012 IEEE MTT-S International*, pp. 1-3, June 2012.

[6] U. R. Pfeiffer *et al*., "A chip-scale packaging technology for 60-GHz wireless chipsets," *Microwave Theory and Techniques, IEEE Transactions on*, vol. 54, no. 8, pp. 3387-3397, Aug. 2006.

[7] P. Herrro, and J. Schoebel, "Planar antenna array at D-band fed by rectangular waveguide for future automotive radar systems," *Microwave Conference, 2008. 38th European*, pp. 1030-1033, Oct. 2008.

[8] S. Beer, and T. Zwick, "Probe based radiation pattern measurements for highly integrated millimeter-wave antennas," *Antennas and Propagation, 2010 Proceedings of the Fourth European Conference on*, pp. 1-5, Apr. 2010.

[9] D. Liu, B. Gaucher, U. Pfeiffer, and J. Grzyb, *Advanced Millimeter-wave Technologies: Antennas, Packaging and Circuits*, John Wiley & Sons Ltd. 2009.

[10] S. Pan, L. Gilreath, P. Heydari, and F. Capolino, "Investigation of a wide-band BiCMOS fully on-chip W-band bowtie slot antenna," *Antennas and Wireless Propagation Letters, IEEE*, vol. 12, pp. 706-709, May 2013.

[11] R. Wang, Y. Sun, and J. C. Scheytt, "An on-board differential bunny-ear antenna design for 60 GHz applications," *German Microwave Conference, 2010*, pp. 9-12, Mar. 2010.

[12] S. Glisic, K. Schmalz, F. Herzel, R. Wang, M. Elkhouly, Y. Sun, and J. C. Scheytt, "A fully integrated 60 GHz transmitter front-end in SiGe BiCMOS technology," *Silicon Monolithic Integrated Circuits in RF systems (SiRF), 2011 IEEE 11th Topical Meeting on*, pp. 149-152, Jan. 2011.

[13] Y. Sun, K. Schmalz, S. Glisic, R. Wang, and J. C. Scheytt, "An integrated differential 60 GHz sliding-IF receiver in SiGe BiCMOS," *Computer Research and Development (ICCRD), 2011 3rd International Conference on*, vol. 3, pp. 297-300, Mar. 2011.

[14] S. Glisic, J. C. Scheytt, Y. Sun, F. Herzel, R. Wang, K. Schmalz, M. Elkhouly, and C. S. Choi, "Fully integrated 60 GHz transceiver in SiGe BiCMOS, RF modules, and 3.6 Gbit/s OFDM data transmission," *International Journal of Microwave and Wireless Technologies*, vol. 3, special issue 02, pp. 139-145, Apr. 2011.

[15] R. Wang, Y. Sun, C. Wipf, and J. C. Scheytt, "An on-board differential patch array antenna and interconnects design for 60 GHz applications," *Microwave, Communications, Antennas, and Electronics Systems (COMCAS), 2011 IEEE International Conference on*, pp. 1-5, Nov. 2011.

[16] R. Wang, Y. Sun, M. Kaynak, S. Beer, and J. C. Scheytt, "A micromachined double-dipole antenna for 122-140 GHz applications based on a SiGe BiCMOS technology," *Microwave Symposium Digest (MTT), 2012 IEEE MTT-S International*, pp. 1-3, Jun. 2012.

[17] R. Wang, Y. Sun, M. Kaynak, and J. C. Scheytt, "Chip-Antenne, Elektronisches Bauelement und Herstellungsverfahren dafür," *International Patent, PCT/EP2013/077951, 2013*, pending.

[18] K. Schmalz, R. Wang, J. Borngräber, W. Debski, W. Winkler, and C. Meliani, "245 GHz SiGe transmitter with integrated antenna and external PLL," *Microwave Symposium Digest (IMS), 2013 IEEE MTT-S International*, pp. 1-3, Jun. 2013.

[19] K. Schmalz, J. Borngräber, R. Wang, W. Debski, W. Winkler, and C. Meliani, "Subharmonic 245 GHz SiGe receiver with antenna," *Microwave Integrated Circuit Conference (EuMIC), 2013 European*, pp. 121-124, Oct. 2013.

[20] K. Schmalz, R. Wang, Y. Mao, W. Debski, H. Gulan, H. Hübers, P. Neumaier, and J. Borngräber, "245 GHz SiGe sensor system for gas spectroscopy," *European Microwave Conference 2014*, pp. 644-647, Oct. 2014.

[21] K. Schmalz, J. Borngräber, W. Debski, M. Elkhouly, R. Wang, P. Neumaier, and H. Hübers, "245 GHz SiGe transmitter array for gas spectroscopy," *2014 IEEE Compound Semiconductor IC Symposium*, pp. 1-4, Oct. 2014.

[22] R. Wang, Y. Sun, M. Kaynak, J. Borngräber, B. Göttel, S. Beer, and J. C. Scheytt, "122 GHz patch antenna designs by using BCB above SiGe BiCMOS wafer process for system-on-chip applications," *Personal Indoor and Mobile Radio Communications (PIMRC), 2013 IEEE 24th International Symposium on*, pp. 1392-1396, Sep. 2013.

2 Basic Considerations on Planar mm-Wave Antenna Development

Defining reasonable specifications and choosing the most appropriate antenna type should be done at the first phase of a planar mm-Wave antenna design. Therefore, in this chapter the most important fundamental parameters to describe the radiation performance of an antenna will be briefly introduced, and then the characteristics of some planar antenna models are discussed. The substrates take crucial roles in the planar antenna designs. Some commonly used approaches to characterize the substrate properties will be reviewed. The excitation and propagation of the surface waves are theoretically studied and explained. The radiation performance of the antennas in this work was measured by a microwave probe based measurement system [1]. The measurement setup and its calibration method will be described. The choice of antenna integration and interconnect technologies will depend on the specific applications. A discussion of the state-of-the-art approaches is given in terms of the main concerns of feasibility, performance, reliability, cost, etc. Taking all the mentioned considerations into account and condensing the design experience gained from the thesis works into a methodology, a design flow and methodology for the integrated planar mm-Wave antennas is proposed in the last part of this chapter. The intention is to make the design meet the specifications with minimum design iterations and development cost.

2.1   Fundamental Parameters of Antennas

Some Fundamental parameters to describe the performance of an antenna are now discussed with emphasis on their effects in a wireless system. They must be thoroughly considered and balanced to meet the design specifications for a certain application.

2.1.1   Field Regions

The space surrounding an antenna is usually subdivided into three regions, from the inner to the outer: reactive near-field, radiating near-field, and far-field [2]. Although the field does not change abruptly between the neighboring regions, there are distinct differences among them. The reactive field predominates in the reactive near-field region. In the radiating near-field region the radiation fields predominate, and the angular field distribution is dependent upon the radial distance from the antenna. The far-field radiation patterns can be obtained by first measuring the antenna in this region, and then applying the near-field to far-field transformation calculation [3]. As the distance increases to the far-field, the near fields are negligible and the angular field distribution is essentially independent of the radial distance, which can be expressed as [4]

$$\vec{E}(r,\theta,\phi) = \left[\hat{\theta}F_\theta(\theta,\phi) + \hat{\phi}F_\phi(\theta,\phi)\right]\frac{e^{-jk_0 r}}{r} V/m \qquad (2.1)$$

where $\vec{E}(r,\theta,\phi)$ is the electric field vector, $\hat{\theta}$ and $\hat{\phi}$ are unit vectors in the spherical coordinate system as illustrated in Figure 2.1, r is the radial distance from the origin (antenna), and $k_0 = 2\pi/\lambda$ is the free-space propagation constant with wavelength $\lambda = c/f$. (2.1) indicates that the E-field propagates in the radial direction with a phase variation of $e^{-jk_0 r}$ and an amplitude decay factor of $1/r$. F_θ and F_ϕ are the pattern functions. They are dependent of the spatial coordinates (θ,ϕ), but independent of r. There is no E-field component in the radial direction. The commonly used criterion to define the far-field distance is

$$R \geq \frac{2D^2}{\lambda} \qquad (2.2)$$

where D is the maximum dimension of the antenna and λ is the wavelength. The antenna performance and measurement are discussed in the range of far-field in this thesis.
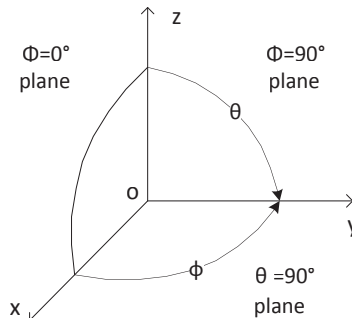
Figure 2.1: The spherical coordinate system.

2.1.2   Radiation Patterns and Antenna Gain

The radiation pattern is a graphical representation of the radiation properties of an antenna in the far-field as a function of spatial coordinates. It can be a plot of the radiation intensity, field strength, directivity, gain, etc. Instead of a 3-D pattern, the patterns in principle planes (E- and H-plane patterns) are usually plotted to demonstrate the radiation properties of antennas for simplicity. The E-plane is defined as the plane formed by the E-field vector and the direction of maximum radiation, and the H-plane is defined as the plane formed by the H-field vector and the direction of maximum radiation.

The directivity $D(\theta, \phi)$ is a figure-of-merit to describe the ability of an antenna to focus its power in a given direction. The gain $G(\theta, \phi)$ is closely related to the directivity by

$$G(\theta, \phi) = e_0 D(\theta, \phi) = e_c e_d e_r D(\theta, \phi) \tag{2.3}$$

where e_0 is the total antenna efficiency, e_c is the conduction efficiency accounting for the conductor losses, e_d is the dielectric efficiency accounting for the dielectric losses, and e_r is the reflection efficiency accounting for the antenna-transmission line impedance mismatching losses. So the gain is a measure that takes into account both the efficiency and the directional properties of an antenna. It is a vital but challenging task to achieve a high radiation efficiency in planar mm-Wave antenna designs. The various loss mechanisms will be discussed in detail later. When the direction is not specified, both the directivity and gain are taken in the direction of the maximum radiation as that in this thesis.

An antenna with a wider main beam can transmit or receiver power over a larger angular region, while an antenna with narrower main beam will only cover a smaller angular region. The most commonly used measure to describe the angular coverage of a main beam is the half power beamwidth or 3-dB beamwidth. Different applications have different preferences for the beamwidth. Most hand-held wireless devices like cell phones require an omnidirectional antenna, which has a constant radiation pattern in the azimuth plane. It enables the devices to transmit and receive equally in all directions. A narrow main beam is desired for the applications of the point-to-point radio links or radars to improve the link budget or avoid the clutters. The maximum directivity and 3-dB beamwidth are both measures of the directional properties of an antenna. For antennas with one narrow main beam and very negligible minor lobes, the maximum directivity and 3-dB beamwidth can be related by approximations [5] [6]

$$D_0 \cong \frac{41,253}{\Theta_1 \Theta_2} \tag{2.4}$$

or

$$D_0 \cong \frac{72,815}{\Theta_1^2 + \Theta_2^2} \tag{2.5}$$

where Θ_1 and Θ_2 are the 3-dB beamwidths in degrees in two orthogonal planes of the main beam, e.g. E- and H-plane. For planar arrays, [7] provides a better approximation

$$D_0 \cong \frac{32,400}{\Theta_1 \Theta_2} \tag{2.6}$$

(2.4)–(2.6) tell us the directivity and beamwidth are inversely proportional to each other, and offer us a convenient way to quickly estimate the directivity or

the antenna coverage range from knowing one of them. There is often compromise when making the design specifications. For instance in a point-to-point radio link, a high directivity can improve the link budget but the price is that it takes more effort to align the transmit and the receive antennas in a large distance due to the narrow beamwidth.

2.1.3   Antennas in Wireless Systems

Figure 2.2 shows a general radio link including the transmitter, receiver, wireless channel, and the antennas. The Friis transmission formula provides a fundamental way to relate the transmitted power P_t, the received power P_r, the wavelength λ, the transmit antenna gain (G_t), receive antenna gain (G_r), and the transmission distance R by

$$P_r = P_t G_t G_r \left(\frac{\lambda}{4\pi R}\right)^2 \tag{2.7}$$

The term of the free-space loss $(\lambda/4\pi R)^2$ can be written in the decibel scale

$$L_0(dB) = -20\log\left(\frac{\lambda}{4\pi R}\right) = -20\log\left(\frac{c}{4\pi R f}\right)$$

$$= 32.5 + 20\log(R) + 20\log(f) \tag{2.8}$$

where c is the speed of light, R is the transmission distance in meters, and f is the frequency in GHz. At the mm-Wave frequencies the free-space loss is much higher than that at lower frequencies, for instance, it is about 68 dB at 60 GHz in a transmission distance of 1 m while that is only 40 dB at 2.4 GHz. The transmission described by (2.7) should be understood as an ideal case, which assumes there are no losses from the interconnects between the antenna and the transceiver, and no extra channel losses other than the free-space loss. In practice we should take into account all the losses to calculate the link budget, and leave a reasonable link margin. Refer to Figure 2.2 we have

$$P_{r,in}(dBm) = P_{t,out} - L_t + G_t - L_0 - L_c + G_r - L_r \tag{2.9}$$

where L_t and L_r are the interconnect or packaging losses of the transmitter and receiver, L_c are the channel losses. As it will be discussed in the later sections, the interconnects require serious considerations to minimize their losses
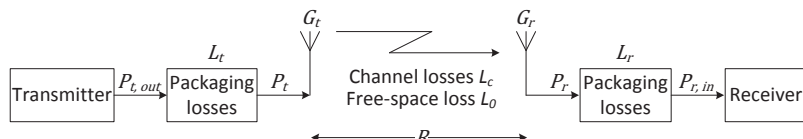

Figure 2.2: A general radio link.

in the mm-Wave range, especially in its higher frequency band. Sophisticated design and precise implementation are required to realize a low-loss interconnection between the off-chip antenna and the transceiver chip, which take a considerable part in the total cost. The channel losses L_c are dependent on many factors, such as the precipitation attenuation for the outdoor applications, the reflection and multipath fading, and the atmospheric attenuation. The atmospheric attenuation is frequency dependent. It is higher at the 60 GHz and 120 GHz bands due to the resonances of the molecular oxygen but lower at the bands of 35, 94, and 135 GHz [4]. The channel has to be characterized in order to calculate the link budget properly.

The system needs a minimum output signal to noise ratio ($SNR_{out,min}$) from the receiver to be able to demodulate the signal at a certain bit error rate (BER) by using a certain modulation scheme. At the ambient temperature of T_0=290 K, the required minimum input power or the sensitivity $P_{r,sens}$ of the receiver can be calculated in decibel scale as

$$P_{r,sens} = -174 dBm/Hz + 10\log(\Delta f) + NF_{tot} + SNR_{out,min} \quad (2.10)$$

where Δf is the receiver bandwidth in Hz, and NF_{tot} is the total noise figure of the receiver. In the mm-Wave range the bandwidth is usually large, because it is one of the reasons why we go to so high frequency. In addition, the total noise figure will inevitably increase with frequency due to the increased NF_{min} of the transistors [8]. Therefore, the $P_{r,sens}$ for a mm-Wave receiver will be higher than that at lower frequencies for the same required $SNR_{out,min}$. The link margin is defined as the difference between the received power calculated in the link budget and the receiver sensitivity

$$Link\ Margin\ (LM) = P_{r,in} - P_{r,sens} > 0 \quad (2.11)$$

In a system design we should specify a reasonable link margin, which is neither too low to guarantee a reliable wireless transmission nor so high that it results in excessive hardware complexity, power consumption, and cost.

From (2.7) to (2.11) we can see that with a higher effective isotropic radiated power (EIRP) $P_{t,out}G_t$ from the transmitter side, a higher antenna gain G_r from the receiver side, and minimum losses (L_t, L_r) from the interconnects either a larger transmission distance or a better link margin can be achieved. A better link margin implies that we have the possibility to employ some higher order modulation schemes to enable a higher transmission data rate, which requires higher $SNR_{out,min}$. At mm-Wave frequencies power generation is extremely difficult, and for hand-held devices the power consumption should be kept as low as possible to prolong the battery life. Therefore, the designs of antenna with high efficiency and gain as well as low-loss interconnects in a low-cost fashion are essential for mm-Wave systems. When it is necessary, an antenna

array consisting of multiple radiating elements in a certain geometrical configuration can be used to achieve a very high gain. A phased array can electrically steer its main beam with a high gain at a fast speed by controlling the feeding phases. When the line-of-sight (LOS) direct radio link is obstructed by some objects like moving people, a wireless system with beamforming function can maintain its radio link by steering the main beam to the best available transmit/receive direction [9]–[12]. However, the price is the high system complexity and cost, which was previously only affordable for military applications.

2.2   Planar Antennas

The planar antennas are compact in size, low-cost, and inherently compatible with the integrated circuits. They can take many kinds of shapes and variations to meet the design specifications. In addition, the input impedance can usually be tuned in a wide range to match to the circuits. All these advantages make them very attractive for the mm-Wave integrated antenna applications. Some planar antenna structures and configurations will be theoretically discussed in this section. The antennas developed in this thesis will be based on and derived from the original models of the basic antenna types. The theoretical analysis presented below is conducted under some simplified conditions, but it helps to understand the essence of the antennas' operation, and gives guidelines for the optimization. The actual performance of the planar antennas, which operate in a non-homogeneous environment and in more complex configurations, has to be predicted by full-wave electromagnetic (EM) simulations.

2.2.1   Planar Dipole Antenna

A. Folded Dipole Antenna

A planar folded dipole is a very attractive and practical structure due to its high bandwidth and large tuning range of the input impedance, while it has very similar radiation patterns to that of a thin wire dipole. The wider bandwidth comes from a larger effective conductor radius [13]. The input impedance of a folded dipole can be accurately predicted by decomposing the total current into a transmission line mode and an antenna mode provided the parallel conductors are close to each other ($space\ s \ll \lambda$), and it has been verified in [14]. The input impedance of an asymmetrical folded dipole antenna has been theoretically studied in [15] by applying the transmission line model. Figure 2.3 depicts the geometry of the antenna, and indicates the decomposition of the total current into the transmission line mode I_X and the antenna mode $I_A = I_{A1} + I_{A2} = I_{A1}(a + 1)$, where I_{A1} is the current on the driven element, and I_{A2} is the current on the parasitic element.
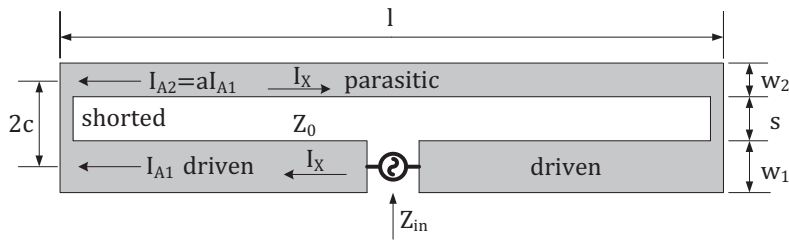
Figure 2.3: Schematic drawing of an asymmetrical folded dipole antenna.

The input impedance can be written as [15]

$$Z_{in} = \frac{2(1+a)^2 Z_A Z_X}{(1+a)^2 Z_A + 2Z_X} \qquad (2.12)$$

where Z_A is the impedance of the equivalent dipole, Z_X is the impedance of the transmission line mode, and $(1+a)^2$ is the impedance step-up ratio. Z_A can be calculated by using an equivalent dipole radius r_e with a length l. r_e is a finite value so that the bandwidth of the antenna is larger than that of a thin wire dipole which has a very small radius. Z_X is the impedance of a shorted transmission line of length $l/2$, which is given by [15]

$$Z_X = jZ_0 \tan\left(\frac{k_0 l}{2}\right) \qquad (2.13)$$

where k_0 is the propagation constant, and Z_0 is the characteristic impedance of the two conductor transmission line. For a half-wavelength folded dipole Z_X becomes infinite, so the expression for the input impedance can be reduced to

$$Z_{in} = (1+a)^2 Z_A \qquad (2.14)$$

It implies that the input impedance can be adjusted by tuning a, which can be approximated as [15]

$$a = \frac{\ln\left(4c + 2\left[(2c)^2 - (w_1/2)^2\right]^{1/2}\right) - \ln(w_1)}{\ln\left(4c + 2\left[(2c)^2 - (w_2/2)^2\right]^{1/2}\right) - \ln(w_2)} \qquad (2.15)$$

where w_1, w_2, and c are shown in Figure 2.3. The analysis is based on the assumptions that the environment is homogenous, and a substrate or a reflector does not exist. For practical designs of on-chip or on-PCB antenna that operates above a ground plane 3-D full-wave simulations are necessary to obtain precise results. But it is clear that by changing the dimensions a wide range of input impedance of the folded dipole antenna can be achieved to match to a circuit. Some on-chip antenna designs shown in chapter 4 are based on the model of folded dipoles above a reflector.

B. A Horizontal Dipole Antenna above a Ground Plane

The planar dipole antennas are very often operating above a ground plane of a package or a module as a reflector to obtain a broadside radiation and a higher gain. The influence of the ground plane on the radiation characteristics can be qualitatively studied by assuming a thin wire dipole above an infinite perfectly electric conducting (PEC) ground plane, since a thin wire dipole has well-known closed form far-field expressions and similar radiation patterns to the planar dipoles.

Figure 2.4 shows a coordinate system which coincides with Figure 2.1. A y-oriented horizontal dipole source S is located above an infinite PEC ground plane (xoy plane). An observation point P is in the far-field. The radiated fields will reach the point P through a direct path r_1 and a reflected path (reflected at point Q on the PEC). The reflection coefficient Γ at the PEC is equal to -1. According to the image theory the received field from the reflected path can be effectively taken into account by assuming that the field is radiated from an image source S' through a direct path r_2.

For a thin wire dipole the far-field radiation from S and S' observed at point P is written as

$$E_S(\theta, \phi, r_1) = E_\varphi(\theta, \phi) \frac{e^{-jk_0 r_1}}{r_1} \qquad (2.16a)$$

$$E_{S'}(\theta, \phi, r_2) = \Gamma E_\varphi(\theta, \phi) \frac{e^{-jk_0 r_2}}{r_2} \qquad (2.16b)$$
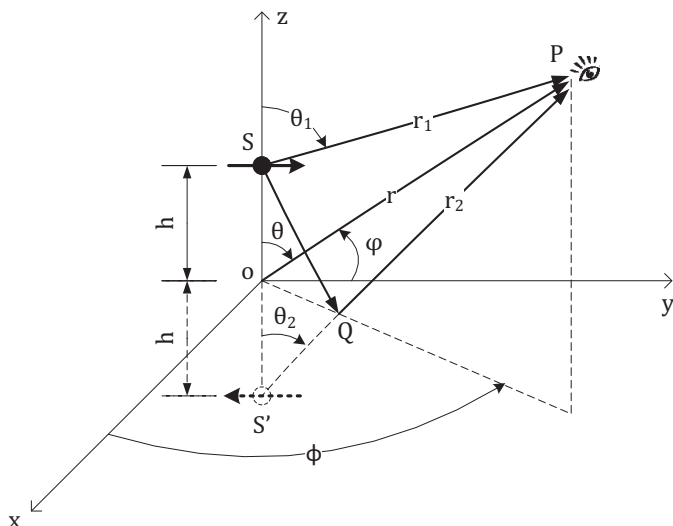

Figure 2.4: A horizontal electric dipole above an infinite PEC ground plane.

For the far-field observations, we have the approximation

for phase term $\begin{cases} r_1 \cong r - h\cos\theta \\ r_2 \cong r + h\cos\theta \end{cases}$; $\theta_1 \cong \theta_2 \cong \theta$ (2.17a)

for amplitude term $r_1 \cong r_2 \cong r$ (2.17b)

So the total far-field observed at P is

$$E_{tot}(\theta,\phi,r) = E_S + E_{S'} = E_\varphi(\theta,\phi)\frac{e^{-jk_0r}}{r}[2j\sin(k_0h\cos\theta)]   (2.18)$$

(2.18) is valid only above the ground plane ($z \geq 0; 0 \leq \theta \leq \pi/2 ; 0 \leq \phi \leq 2\pi$), because there is no field below the PEC. We can see that the total field is the product of the field of a single element placed at the origin and a factor (within the bracket) that is dependent of the height h. The far-field function of a finite length thin wire dipole can be written as [2]

$$E_\varphi^{finite}(\theta,\phi) = j\frac{\eta_0 I_0}{2\pi}\left[\frac{\cos\left(\frac{k_0l}{2}\sin\theta\sin\phi\right)-\cos\left(\frac{k_0l}{2}\right)}{\sqrt{1-\sin^2\theta\sin^2\phi}}\right]   (2.19)$$

where η_0 is the wave impedance in free-space, l is the length of the dipole, and I_0 is the peak value of the current. For a half-wavelength dipole above a PEC, the total field can be expressed as

$$E_\varphi^{half}(\theta,\varphi,h) = -\left(\frac{\eta_0 I_0}{\pi}\right)\left[\frac{\cos\left(\frac{\pi}{2}\sin\theta\sin\phi\right)}{\sqrt{1-\sin^2\theta\sin^2\phi}}\right][\sin(k_0h\cos\theta)]   (2.20)$$

The radiation intensity is

$$U(\theta,\phi,h) = \frac{1}{2\eta_0}\left|E_\varphi^{half}(\theta,\phi,h)\right|^2   (2.21)$$

The normalized radiation intensity patterns for different height h in E- (ϕ=90°) and H-plane (ϕ=0°) are plotted in Figure 2.5. The patterns are symmetrical so only a half of them for each height are plotted. It can be seen that the shape of the patterns change significantly as the height h varies. When h is larger than half-wavelength there will be sidelobes. Actually, the height is an important parameter in the design not only for the shape of the pattern but also for the input impedance. In practical designs there will be substrate(s) between the planar radiator and the ground plane. The reflection coefficient at the non-PEC ground plane with a finite conductivity will no longer be -1 but some similar values which are dependent on the incident angles and field polarizations. Some of the reflected waves will radiate out of the substrate with refraction at the dielectric-air interface, and some are trapped as surface waves that are dissipated as losses or diffracted at the truncated edges of the finite substrate as spurious radiations.
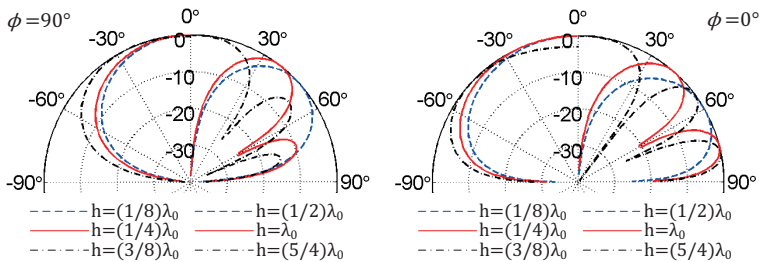
Figure 2.5: Normalized radiation intensity patterns in dB scale in E-plane (left) and H-plane (right) for different height h. (Only a half of the pattern is drawn for each h.)

2.2.2   Rectangular Patch Antenna

The rectangular patch antenna is probably the most widely used planar configuration because of ease of analysis and fabrication, and its attractive radiation characteristics. It can be excited by many feeding methods. The most frequently used types in the mm-Wave range are the microstrip line direct feeding, aperture coupling, and proximity coupling [16]–[19]. A wide range of impedance can be achieved by employing these feeding methods to match the antennas directly to the circuits. Due to the aforementioned advantages, the patch antennas are not only frequently used as a single element but also in antenna arrays. The major drawback of the patch antenna is its narrow bandwidth. Some techniques are developed to broaden the bandwidth, such as multimode operation [20]–[23], parasitic elements [24]–[26], and stacked patches [27] [28].

The patch antenna can be analyzed by either a transmission line model or a cavity model [29] [30], which are most accurate for thin substrates [31]. Figure 2.6 (a) and (b) demonstrate the transmission line model. As it is shown that the patch antenna is represented by two radiating slots separated by a low impedance transmission line of width W and length L. When L is equal to half wavelength in an effective homogeneous dielectric with an effective dielectric constant of ϵ_e, the phase of the E-field will undergo 180 degrees changing from one radiating slot to the other one. The radiation from the slots will add in phase in the positive z direction so that the patch antenna has a broadside radiation. There is fringing field at the edges of the patch because of its finite size, so the patch looks electrically longer and wider than its physical size. This effect must be taken into account in the designs, otherwise, the resonant frequency can be shifted. The extension ΔL due to the fringing effect on each end along the length can be calculated by [32]

$$\Delta L = 0.412 h \frac{(\epsilon_e + 0.3)(\frac{W}{h} + 0.264)}{(\epsilon_e - 0.258)(\frac{W}{h} + 0.8)} \qquad (2.22)$$
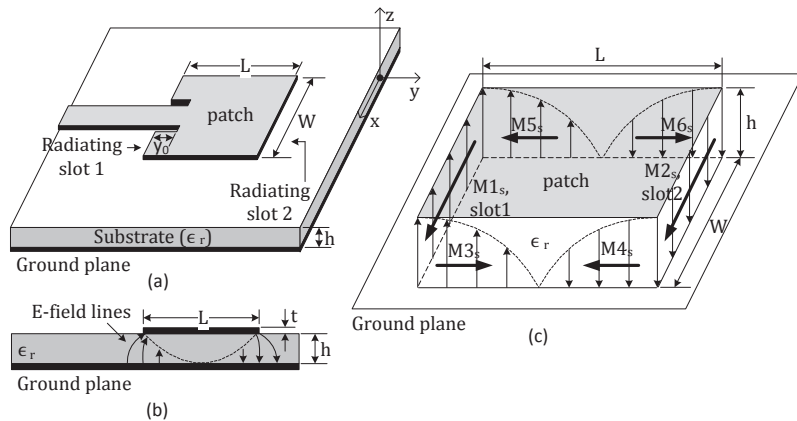
Figure 2.6: (a) Perspective view of the patch antenna (transmission line model); (b) Side view of the patch antenna (transmission line model); (c) Field configurations of the patch antenna (cavity model).

where

$$\epsilon_e = \frac{\epsilon_r + 1}{2} + \frac{\epsilon_r - 1}{2} [1 + 12 \frac{h}{W}]^{-1/2}, \quad \frac{W}{h} > 1 \tag{2.23}$$

So the effective length of the patch is

$$L_e = L + 2\Delta L \tag{2.24}$$

Then the resonant frequency (dominant mode) of a half-wavelength patch antenna is

$$f_0 = \frac{c_0}{2 L_e \sqrt{\epsilon_e}} \tag{2.25}$$

where c_0 is the velocity of light in free-space. For an efficient radiator, the width of the patch can be determined by [33]

$$W = \frac{c_0}{2 f_0} \sqrt{\frac{2}{\epsilon_r + 1}} \tag{2.26}$$

The input resistance has its maximum value at the open ends of the patch, where the voltage (E-field) is maximum and the current is minimum. The minimum value appears at the center of the patch where the voltage is ideally zero and the current is maximum. Therefore, the input resistance can be adjusted by tuning the inset feeding position y_0 [29] [30] to match to the transmission line and the circuits. For the other two popular feeding schemes, aperture coupling and proximity coupling, a similar method can be applied, i.e. tuning the feeding position.

The cavity model as shown in Figure 2.6 (c) is more complex than the transmission line model. However, it reveals the double-slot radiation mechanism of

a patch antenna in a clearer way. It models the patch antenna as a dielectric-loaded cavity with 2 PEC walls (patch and ground plane) and 4 perfectly magnetic conducting (PMC) walls (sidewalls). It assumes that the substrate is truncated and does not extend beyond the patch. The sidewalls represent 4 narrow (h is small) slots. The E-field distribution of the dominant mode [2] of the patch antenna is illustrated in Figure 2.6 (c). The boundary condition of the fields at a PMC wall is

$$-\hat{n} \times \vec{E} = \vec{M_s} \tag{2.27a}$$

$$\hat{n} \times \vec{H} = \vec{J_s} = 0 \tag{2.27b}$$

where $\hat{n}$ is the normal unit vector pointing out of each sidewall. From (2.27) we can see that there are only magnetic surface current density sources on the slots. The magnetic sources ($\vec{M1_s}$ and $\vec{M2_s}$) on the radiating slot 1 and 2 have equal magnitude and phase, and they form a two element slots array which gives a broadside radiation. The radiation from the sources on the other two slots cancels each other in the principle planes because of their equal magnitudes but opposite phases. The radiation from them in the non-principle planes is also smaller than that from radiating slot 1 and 2, so they are usually considered as non-radiating slots. The patch antenna based designs are presented in chapter 3 by using PCB technology for 60 GHz applications, and in chapter 5 by using polymer above-wafer process for 122 GHz applications.

2.2.3   Vivaldi Antenna

One of the most attractive features of the mm-Wave applications is its large available bandwidth, e.g. 57–66 GHz in the 60 GHz band in Europe. It requires wideband integrated antennas, which preferably have constant beamwidth, gain, and fairly good reflection coefficient over the entire bandwidth. The Vivaldi antenna as shown in Figure 2.7 (a) was originally reported in [34]. It is a member of aperiodic continuously scaled, gradually curved, non-resonant, and end-fire travelling wave antenna structures. It can be easily implemented on a thin film substrate by printed circuits technologies [34] [35]. The shape of the tapered slot is described by an exponential function [34]

$$y = \pm Ae^{px} \tag{2.28}$$

where y is the half separation of the slot lines, x is the length of the slot, A is a half of the minimum slot width, and p is the magnification factor which determines the beamwidth. Different parts of the antenna radiate efficiently at different frequencies, while the size of the radiating parts is constant in wavelength. Therefore, the Vivaldi antenna has theoretically unlimited bandwidth. In practice the high and low frequency limit will be determined by the minimum and maximum slot width of W_H and W_L, respectively, due to the finite

antenna size. The cut-off wavelength is defined as $\lambda_c = 2W_L$. The frequencies that have longer wavelength will not be radiated efficiently. The gain is proportional to the overall length L of the antenna which is in common with other travelling wave structures [36].

The bandwidth of the Vivaldi antenna can be limited by its feeding mechanism, i.e. the transition of planar transmission lines to the slot line. The transition needs to be sophisticatedly considered and designed together with the antenna for specific applications [37]–[39]. A derivative of the Vivaldi antenna, which is named as bunny-ear antenna, was originally introduced in [40], and further characterized in [41] and [42]. As shown in Figure 2.7 (b) the transition from a pair of balanced planar transmission lines to the radiating slot is exponentially tapered to achieve a wideband impedance matching. This structure is inherently compatible with a differential circuit, which has many advantages over its single-ended counterpart. A differential bunny-ear antenna design is presented in chapter 3 for 60 GHz applications.
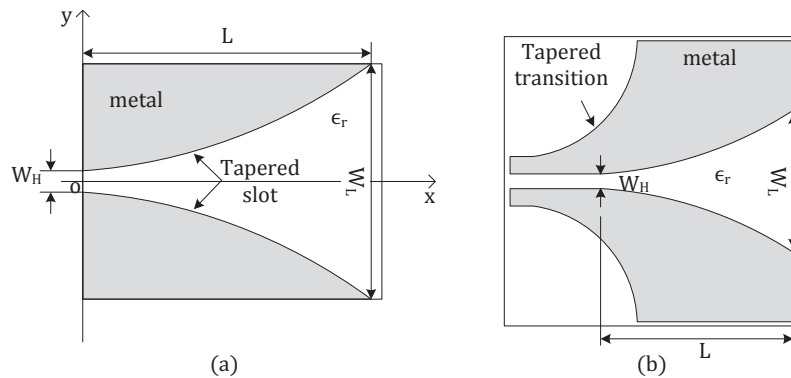
Figure 2.7: (a) The Vivaldi antenna; (b) The bunny-ear antenna.

2.2.4   Antenna Arrays

The planar antennas usually have low gain and efficiency. In many applications it is desired to have a high gain, a narrow and steerable beam of the antenna to mitigate the noise and clutter or improve the quality of service even in a non-line-of-sight radio link. A planar phased array antenna comprises of a certain number of antenna elements, which are normally identical, with individually controllable excitation magnitudes and phases in a suitable geometrical arrangement. The radiation from each element will add constructively or destructively in certain spatial directions that the steerable beams are achieved. The radiation pattern is the product of a single element factor and an array factor, assuming no mutual coupling. As the frequency comes to the mm-Wave range, the size of a planar phased array shrinks so that it becomes possible to be inte-

grated with the ICs in a module. On the other hand, the complex feeding network and antenna elements are fabricated on the same substrate, which can lead to considerably undesirable coupling due to the substrate modes and spurious radiation. Large mutual coupling levels among the antenna elements can degrade sidelobe levels, main beam shape, and possibly cause array blindness [43]. The spurious radiation from the feeding lines can interfere with the radiation patterns significantly. The development of a phased array antenna is a complicated task, which includes selection of substrate, determination of antenna elements and its feeding methods, design of a single element, and finally the design of complete antenna array. Special efforts should be made to design the feeding networks.

2.3   Substrates

The substrate takes a crucial role in the mm-Wave planar antenna designs. The permittivity of the substrate is directly related to the electrical dimensions of the structures in or on it, which decide the resonant frequencies. The permittivity of the dielectrics generally changes with frequency due to its physical nature, and in practice it is determined experimentally in the interested frequency bands for the accurate values, although there are theoretical equations, like Debye equation [44], to calculate it as a function of frequency for some ideal cases.

As the wavelength decreases in the mm-Wave range, the substrate becomes electrically thick so that the higher order modes of substrate waves are supported. They propagate in the substrate and dissipate as losses which lower the radiation efficiency of the antenna. In addition, they can be diffracted at the truncated edges of the substrate of finite size. The diffracted fields can interfere with the main radiation patterns and distort them. The following discussion on substrates is given in two aspects: the characterization of dielectric properties and the substrate modes.

2.3.1   Dielectric Characterization

The most important properties of a dielectric substrate in antenna designs are described by its complex permittivity as

$$\epsilon = \epsilon' - j\epsilon'' \tag{2.29}$$

The imaginary part ϵ'' accounts for the loss in the dielectric (heat) due to damping of the vibrating dipole moments, when an alternating electric field is applied [4]. In practice the complex permittivity is more often expressed by the relative permittivity ϵ_r (or dielectric constant), and the loss tangent $\tan\delta$ as

$$\epsilon = \epsilon'(1 - j\tan\delta) = \epsilon_0\epsilon_r(1 - j\tan\delta)$$

$$\tan\delta = \frac{\omega\epsilon'' + \sigma}{\omega\epsilon'} \qquad (2.30)$$

where ω is the angular frequency of the applied field, and σ is the conductivity of the dielectric which results in conductive loss. The manufacturers of the substrates usually give the properties only at relatively lower frequencies (≤ 10 GHz), which is not adequate for mm-Wave designs. A variety of dielectric characterization techniques have been proposed, and each of them has its own advantages and limitations.

The method of resonant cavities offers high Q measurement. Closed cavities can be used for liquid or mold materials, while open resonators have been proven capable to measure the complex permittivity of very low-loss, thin, and planar dielectrics in the mm-Wave range [45]–[48]. However, it is complex to implement them. The printed resonant circuits such as resonant rings [49] or open stubs, which are easier to implement, can also be used to have a good estimation of the permittivity. But it is difficult to measure the loss from the dielectric because of the non-negligible loss from the conductors.

Broadband characterization of dielectrics usually involves various transmission line approaches. They are generally insensitive to very low losses. A wave propagates along a general non-ideal transmission line will have a complex propagation constant, which includes the information of the phase velocity and the attenuation constant. Therefore, the relative permittivity and loss tangent can be extracted by analyzing the phase and magnitude of the measured reflection (S_{11}, S_{22}) and transmission coefficients (S_{21}, S_{12}), respectively. The free-space can be viewed as a special type of transmission line. In a free-space method setup [50] [51] a thin planar sample is placed between two antennas, normally horn antennas, and the S-parameters are measured to extract the dielectric properties. This approach is found very useful in the mm-Wave range, although the experimental setup and the free-space calibration is complex. Open-ended or filled transmission lines like coaxial lines or rectangular waveguides can also be used to characterize the dielectrics [45] [52]–[54]. But it still needs some efforts to fit the dielectrics to the transmission lines properly. The planar transmission line approach, either microstrip [55] or coplanar waveguide (CPW) [56], is probably the simplest way to evaluate the dielectric properties for the mm-Wave planar antenna applications. They can be fabricated on the same substrate as the planar antennas by using the same technology. The S-parameter is measured by microwave probes, and after applying certain de-embedding techniques the complex propagation constant can be extracted, thus obtaining the effective permittivity and attenuation constant. Finally, analytical formulas can be used to calculate the complex permittivity of the substrate. This method will be employed to characterize the PCB materials in chapter 3.

2.3.2   Substrate Waves

An antenna operating on a substrate can excite substrate waves, which lower the radiation efficiency and possibly distort the radiation patterns. The substrate modes in two scenarios in this thesis, a grounded dielectric (surface waves) and a parallel plate dielectric waveguide (guided waves), are studied in this section.

A. Surface Waves on a Grounded Dielectric

A typical configuration of a planar antenna is that a radiator is formed on top of a grounded dielectric substrate. We can understand qualitatively how the antennas radiate and excite surface waves from a ray point of view. In Figure 2.8 a point source (antenna) is located on a dielectric (ϵ_r) at $(d, 0, 0)$. It radiates waves directly into free-space above the dielectric, which are designated as radiated waves. At the same time the source also excites waves (can be many modes at discontinuities of an antenna) into the dielectric, and they are reflected by the ground plane to the dielectric-air interface. In this case the Snell's law for either parallel or perpendicular polarization can be written as

$$\sin\theta_t = \sqrt{\frac{\epsilon_1}{\epsilon_2}}\sin\theta_i = \sqrt{\frac{\epsilon_r\epsilon_0}{\epsilon_0}}\sin\theta_i = \sqrt{\epsilon_r}\sin\theta_i, \ \ \epsilon_r > 1 \qquad (2.31)$$

where θ_i is the incidence angle, and θ_t is the refraction angle. It can be seen from (2.31) that if θ_i increases, the refraction angle θ_t will increase at a faster rate. Therefore, when θ_i reaches the so called critical angle θ_c, θ_t will be 90°. When the incidence angle is smaller than the critical angle (see $\theta_i = \theta_1 < \theta_c$ in Figure 2.8), the waves are partially reflected by the dielectric-air interface and progressively leaking into the air (leaky waves), thus eventually contributing to radiation. If the incidence angle θ_i is equal to or beyond the critical angle θ_c (see $\theta_2 > \theta_c$ in Figure 2.8), the incident waves will be totally reflected. Then the waves are trapped inside the dielectric and propagating along β as surface waves, which decay exponentially away from the dielectric surface ($x \geq d$) along h. The surface waves spread out in a cylindrical fashion around the source point, and the amplitude of the fields decay with distance $1/\sqrt{r}$ that more slowly than space waves $(1/r)$ [16] [57]. The surface waves are generally considered as losses since they are trapped in the dielectric of infinite size, and do not contribute to radiation. However, for the dielectric with finite size the surface waves can be reflected and diffracted at the truncated edges, thus causing spurious radiation that probably distorts the main radiation patterns. In addition, the travelling of the surface waves will introduce coupling between the antennas or circuits which are fabricated on the same substrate. This effect can severely degrade the performance of an antenna array and even lead to malfunction (array blindness).
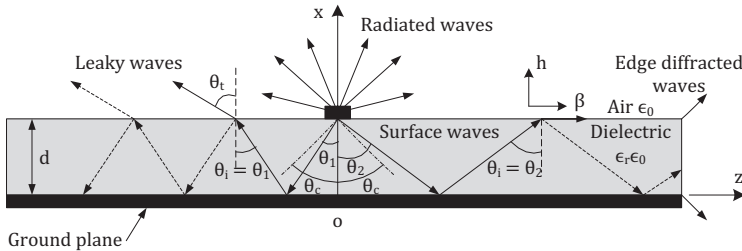
Figure 2.8: Presentation of a grounded dielectric and various waves.

The surface waves require certain conditions to propagate in a dielectric after being excited. A grounded dielectric cannot support transverse electromagnetic (TEM) waves because it is a non-homogeneous media. Transverse magnetic (TM) and transverse electric (TE) surface waves will be studied. The general solutions for the TEM, TM, and TE waves are given in the appendix A.

TM Modes

Consider the grounded dielectric as shown in Figure 2.8. The dielectric has a dielectric constant of ϵ_r and a thickness of d. We assume the dielectric has infinite extent in the y and z direction, and the surface waves propagate along β (+z) with an $e^{-j\beta z}$ propagation factor and no variation in the y direction ($\partial/\partial y = 0$).

The longitudinal electric field $E_z(x, y, z) = e_z(x, y)e^{-j\beta z}$ must satisfy the Helmholtz equation in both the dielectric and air regions:

$$\left(\frac{\partial^2}{\partial x} + \frac{\partial^2}{\partial y} + \frac{\partial^2}{\partial z} + \epsilon_r k_0^2\right) e_z(x, y)e^{-j\beta z} = 0, \quad \text{for } 0 \leq x \leq d \qquad (2.32a)$$

$$\left(\frac{\partial^2}{\partial x} + \frac{\partial^2}{\partial y} + \frac{\partial^2}{\partial z} + k_0^2\right) e_z(x, y)e^{-j\beta z} = 0, \qquad \text{for } d \leq x < \infty \qquad (2.32b)$$

where $k_0 = \omega\sqrt{\epsilon_0 \mu_0}$ is the wave number in free-space. Taking into account $\partial/\partial y = 0$, (2.32) can be reduced to

$$\left(\frac{\partial^2}{\partial x} + \epsilon_r k_0^2 - \beta^2\right) e_z(x, y) = 0, \quad \text{for } 0 \leq x \leq d \qquad (2.33a)$$

$$\left(\frac{\partial^2}{\partial x} + k_0^2 - \beta^2\right) e_z(x, y) = 0, \qquad \text{for } d \leq x < \infty \qquad (2.33b)$$

The cutoff wavenumbers for the two regions are defined as

$$k_c^2 = \epsilon_r k_0^2 - \beta^2, \quad \text{for } 0 \leq x \leq d \qquad (2.34a)$$

$$h^2 = \beta^2 - k_0^2, \qquad \text{for } d \leq x < \infty \qquad (2.34b)$$

where the sign on h^2 is chosen in anticipation of an exponentially decaying along x-axis above the dielectric-air interface [4]. The propagation constant β of a certain surface wave must be the same in both air and dielectric regions to

achieve phase matching of the tangential fields at the dielectric interface for all values of z. The general solutions to (2.33) are

$$e_z(x, y) = A \sin k_c x + B \cos k_c x, \quad \text{for } 0 \leq x \leq d \qquad (2.35a)$$

$$e_z(x, y) = C e^{hx} + D e^{-hx}, \qquad \text{for } d \leq x < \infty \qquad (2.35b)$$

The boundary conditions are

$$E_z(x, y, z) = 0, \qquad \text{at } x = 0 \qquad (2.36a)$$

$$E_z(x, y, z) < \infty, \qquad \text{as } x \to \infty \qquad (2.36b)$$

$$E_z(x, y, z) \text{ continous}, \quad \text{at } x = d \qquad (2.36c)$$

$$H_y(x, y, z) \text{ continous}, \quad \text{at } x = d \qquad (2.36d)$$

From appendix A we have $H_z = E_y = H_x = 0$. The boundary conditions (2.36a) and (2.36b) imply that $B = 0$ and $C = 0$ in (2.35). Then from the continuous condition of (2.36c) we have

$$A \sin k_c d = D e^{-hd} \qquad (2.37)$$

As indicated in (2.36d) the magnetic field must be also continuous at the interface, from (2.35) and (A.6) in appendix A we have

$$\frac{\epsilon_r A}{k_c} \cos k_c d = \frac{D}{h} e^{-hd} \qquad (2.38)$$

Combine (2.37) and (2.38) to eliminate A and D, then

$$k_c \tan k_c d = \epsilon_r h \qquad (2.39)$$

Eliminating β from (2.34) we can get another equation

$$k_c^2 + h^2 = (\epsilon_r - 1) k_0^2 \qquad (2.40)$$

Given d and k_0, then k_c and h can be solved numerically from (2.39) and (2.40). However, a graphical solution can show the results more visually. Multiplying both sides of (2.39) and (2.40) by d and d^2, respectively, we have

$$(k_c d) \tan(k_c d) = \epsilon_r (hd) \qquad (2.41a)$$

$$(k_c d)^2 + (hd)^2 = (\epsilon_r - 1)(k_0 d)^2 \qquad (2.41b)$$

(2.41a) and (2.41b) can be plotted on the $k_c d$–hd plane as shown in Figure 2.9 for 2 dielectric constants ϵ_r=3 and ϵ_r=11.9, which are the values of some often used PCB materials (e.g. Rogers 3003) for on-board antenna designs and silicon for on-chip antenna designs. Each intersection of the curves, which are constituted by (2.41a) and (2.41b), implies a common solution to both of them. Only the first quadrant is plotted, because h should be positive real due to the waves decaying along the x-axis, and a negative k_c merely changes the sign of
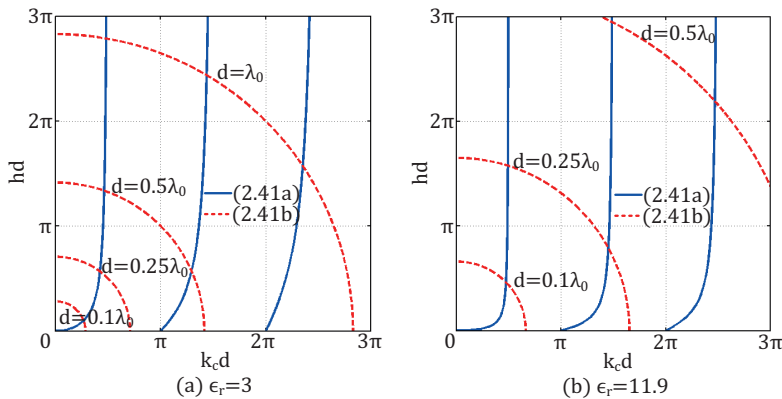
Figure 2.9: Graphic solutions to (2.41) for TM modes with (a) $\epsilon_r=3$ and (b) $\epsilon_r=11.9$.

constant A in (2.35a). (2.41b) is an equation of a circle with a radius of $\sqrt{\epsilon_r-1}k_0 d$. As $\sqrt{\epsilon_r-1}k_0 d$ increases, either ϵ_r or d or both, the circle may have more intersections with the tangent function curves described by (2.41a), implying that more TM modes can propagate.

It can be observed that for an ordinary dielectric, which has a finite thickness and a dielectric constant greater than 1, there is always at least one propagating TM mode, designated as TM_0 mode, which has a zero cutoff frequency. TM_0 mode can have some field lines aligned with the field lines of the quasi-TEM mode of microstrip lines, which are often used to construct feeding structures of planar antennas on the dielectrics. The fields of the TM_0 mode are zero at zero frequency, so the coupling to the quasi-TEM mode is negligible until a threshold frequency is reached. Studies have shown that the threshold frequency can be defined as [58]

$$f_T = \frac{c_0}{2\pi d}\sqrt{\frac{2}{\epsilon_r-1}}\tan^{-1}(\epsilon_r) \tag{2.42}$$

For $\epsilon_r > 10$, (2.42) reduces to [58]

$$f_T(\text{GHz}) = \frac{10.6}{d\sqrt{\epsilon_r}} \quad (\text{d in cm}) \tag{2.43}$$

The higher order modes TM_n will start propagating when the radius of the circle reaches $n\pi$ (Figure 2.9). Therefore, the cutoff frequency of the TM_n modes can be derived as

$$\sqrt{\epsilon_r-1}\frac{2\pi}{\lambda_c}d = n\pi \tag{2.44a}$$

$$f_c = \frac{nc_0}{2d\sqrt{\epsilon_r-1}}, \quad n = 0, 1, 2, \dots \tag{2.44b}$$

As soon as k_c and h have been determined, the complete expressions for the fields can be obtained from (2.34), (2.35), (2.37), and (A.6) in appendix A as

$$
E_z(x,y,z) = \begin{cases} A\sin k_c x e^{-j\beta z} & \text{for } 0 \leq x \leq d \\ A\sin k_c d e^{-h(x-d)} e^{-j\beta z} & \text{for } d \leq x < \infty \end{cases} \tag{2.45a}
$$

$$
E_x(x,y,z) = \begin{cases} \dfrac{-j\beta}{k_c} A\cos k_c x e^{-j\beta z} & \text{for } 0 \leq x \leq d \\ \dfrac{-j\beta}{h} A\sin k_c d e^{-h(x-d)} e^{-j\beta z} & \text{for } d \leq x < \infty \end{cases} \tag{2.45b}
$$

$$
H_y(x,y,z) = \begin{cases} \dfrac{-j\omega\epsilon_0\epsilon_r}{k_c} A\cos k_c x e^{-j\beta z} & \text{for } 0 \leq x \leq d \\ \dfrac{-j\omega\epsilon_0}{h} A\sin k_c d e^{-h(x-d)} e^{-j\beta z} & \text{for } d \leq x < \infty \end{cases} \tag{2.45c}
$$

TE Modes

The TE modes can be solved in a similar procedure as that for TM modes. The longitudinal magnetic field must satisfy the wave equations

$$
\left(\frac{\partial^2}{\partial x} + k_c^2\right) h_z(x,y) = 0, \qquad \text{for } 0 \leq x \leq d \tag{2.46a}
$$

$$
\left(\frac{\partial^2}{\partial x} - h^2\right) h_z(x,y) = 0, \qquad \text{for } d \leq x < \infty \tag{2.46b}
$$

After applying the certain boundary conditions to the general solutions of the fields in two regions, two equations can be achieved as

$$
-(k_c d)\cot(k_c d) = (hd) \tag{2.47a}
$$

$$
(k_c d)^2 + (hd)^2 = (\epsilon_r - 1)(k_0 d)^2 \tag{2.47b}
$$

where k_c and h can be solved by either numerical or graphical approach. The cutoff frequency of TE_n modes can be found as

$$
f_c = \frac{(2n-1)c_0}{4d\sqrt{\epsilon_r - 1}}, \quad n = 1, 2, 3, \dots \tag{2.48}
$$

For most of antenna designs, the higher order surface wave modes should be avoided to maintain high radiation efficiency within the bandwidth of interest. The selection of substrates, i.e. the dielectric constant ϵ_r and the thickness d, is important to minimize the number of propagating surface wave modes. Figure 2.10 shows a plot of the cutoff frequencies (below them certain surface wave modes will become evanescent modes) of some foremost surface wave modes as a function of the substrate thickness d for two common dielectric constants ϵ_r=3 and ϵ_r=11.9, which give references for a large variety of low and high permittivity substrates for planar mm-Wave antenna designs. The threshold frequency f_T defined in (2.42) and (2.43), below which there is little coupling between the TM_0 mode with zero cutoff frequency and the Quasi-TEM mode of microstrip lines, is also plotted. The propagation constant β of the higher order surface wave mode is small when its cutoff frequency is just
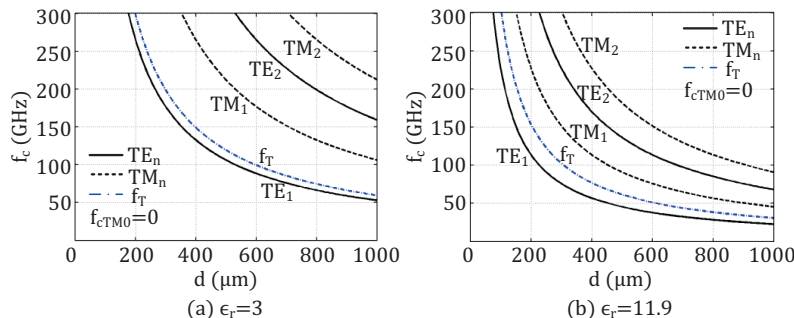
Figure 2.10: Plotting of cutoff frequencies f_c of TM_n and TE_n surface wave modes as well as the threshold frequency f_T as a function of dielectric thickness. (a) $\epsilon_r=3$; (b) $\epsilon_r=11.9$.

reached ($\beta = k_0$ at the cutoff frequency for certain mode). As frequency increases β will be more close to or even exceed the guided wave propagation constant of the antenna, then the modes coupling and loss become more significant.

B. Parallel Plate Guided Waves

It is quite normal that there is a metal layer also on top of the dielectrics, especially for the on-chip designs because there is requirement on the minimum global metal density for each metal layer in the back-end-of-line (BEOL) process, and the chip is usually seated on a ground plane of a package. In this case a parallel plate waveguide is formed at least locally. The geometry of such a waveguide is shown in Figure 2.11. We assume the width of the waveguide in y direction is very large compared with the thickness d so that fringing fields and any y variations can be ignored, and the guided waves propagate in the +z direction with an $e^{-j\beta z}$ propagation factor. Since the media is homogeneous, it can support TEM mode besides TM and TE modes. The analysis of the modes is analogous to that for a grounded dielectric, so the detailed analysis will not be repeated here. The cutoff frequency for the TEM mode is zero, and the cutoff frequency for TM_n and TE_n modes is identical as

$$f_c = \frac{n}{2d\sqrt{\mu\epsilon_r\epsilon_0}}, \quad n = 1, 2, 3 \dots \tag{2.49}$$
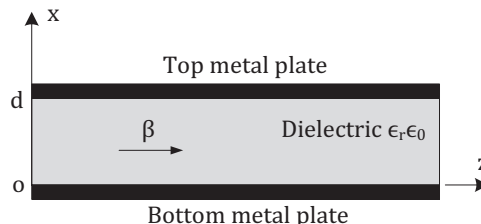

Figure 2.11: Geometry of a parallel plate waveguide.
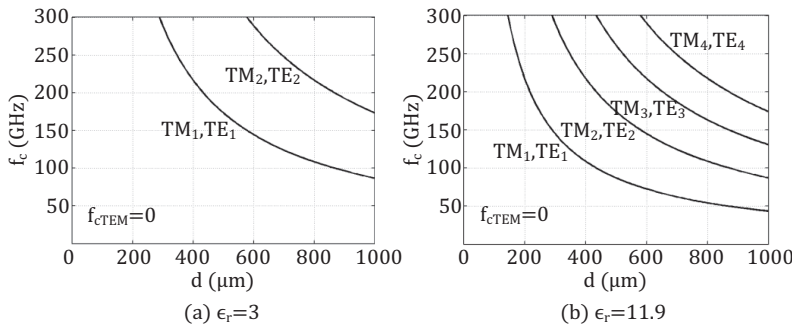
Figure 2.12: Plotting of cutoff frequencies f_c of TM_n and TE_n modes in a parallel plate waveguide as a function of d. (a) $\epsilon_r=3$; (b) $\epsilon_r=11.9$.

There is no TE_0 mode, and the TM_0 is actually identical to the TEM mode. The cutoff frequency f_c of the TM_n and TE_n modes is plotted as a function of the dielectric thickness d in Figure 2.12 for $\epsilon_r=3$ and $\epsilon_r=11.9$, respectively. It can be observed that the cutoff frequencies for the higher order modes are higher than those of the surface waves in a grounded dielectric slab with the same dielectric constant and thickness (Figure 2.10).

2.4   Antenna Measurement

At mm-Wave frequencies the planar antenna measurements are very challenging. Conventionally, the antenna under test is connected to the measurement setup by a coaxial cable or a waveguide connector. However, the feature sizes of these types of connectors are too large for the printed planar mm-Wave antennas, especially for the on-chip antennas. A probe based antenna measurement takes the advantages of measuring exactly at the reference plane of interest, and avoiding the effort of mounting connectors, which is a very difficult task or even not possible. On the other hand, there are also challenges. A special calibration procedure has to be conducted to the measurement setup, which is vital to achieve an accurate measurement. As many other measurements using a microwave probe, the measurement is sensitive to vibration so that the AUT cannot be rotated, and has to be well fixed on a sample holder. Since the shielding of a microwave probe is worse than that of a conventional connector for antenna measurement, the spurious radiation and reflection from the probe will limit the dynamic range.

The radiation performance of the antennas in this work was measured at the Karlsruhe Institute of Technology (KIT) by a microwave probe based measurement setup as shown in Figure 2.13, which is described in detail in [1] and [59]. The mechanical assembly of the system as illustrated in Figure 2.13 (a) contains two arms and two rotary stages, which are consistent with the azimuth and elevation angles, to rotate the receive horn antenna around the AUT to

measure nearly the 3-D radiation patterns or three sectional planes in a far-field distance of 60 cm. However, the existence of the table will limit the measurement range to about 270° in horizontal plane and 255° in one vertical plane. The receive horn antenna can be rotated 90° to enable the measurement of two polarizations. The AUT, specifically the part containing the probing pads is well fixed on a sample holder that is made of dielectric foam ($\epsilon_r < 1.1$, $\tan\delta < 0.001$), resembling air in terms of electric properties. In this way the radiating part of the AUT can be positioned in the air, and thus achieving measurement in a quasi-in-air condition, as shown in Figure 2.13(b). For the measurement in different frequency bands the frequency modules (RF sources and harmonic mixers) as well the RF probes are interchanged.

The principle of the calibration procedure is explained in detail in Chapter 17 of [60]. To sum up, it requires three steps. First, the transmit path of the system is calibrated to the reference plane at the input port 1 of the reference horn antenna and the probe as shown in Figure 2.14. In the second step a reference horn antenna with well-known gain G_{ref} is attached to the system to calibrate the free-space loss and the system losses as shown in Figure 2.14 (a). From the measured $S_{21,ref}$ we can get

$$G_{system} = \frac{|S_{21,ref}|^2}{G_{ref}} \tag{2.50}$$

with G_{system} representing all system losses (including free-space loss) and the gain of the receive horn antenna. The third step is the calibration of the probe as shown in Figure 2.14 (b), which moves the reference plane to the probe tips to measure the complex input impedance of the device. The short-open-load (SOL) method is employed to make the 1-port (only port1) calibration by using
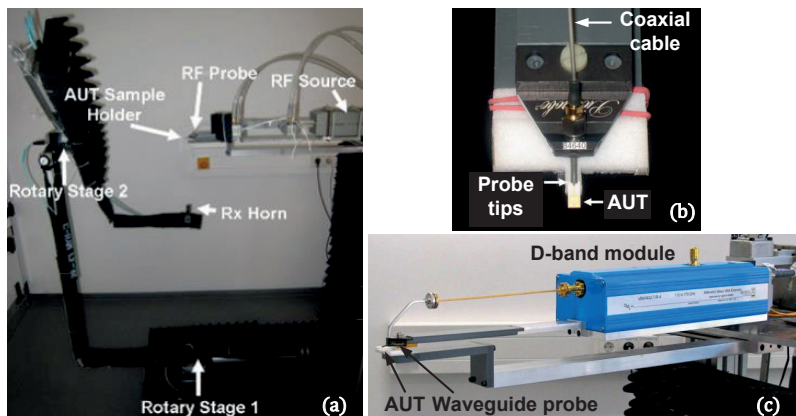
Figure 2.13: Probed based measurement setup [1][59]: (a) mechanical assembly, (b) coaxial cable probe and AUT contact, (c) D-band (110–170 GHz) transmit/receive module, waveguide probe, and the AUT.
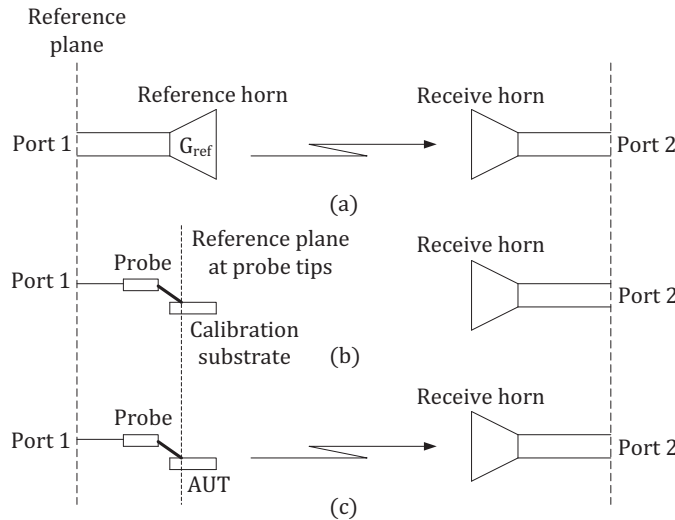
Figure 2.14: Calibration procedure for a probe based mm-Wave antenna measurement setup: (a) gain calibration, (b) probe calibration, (c) AUT measurement.
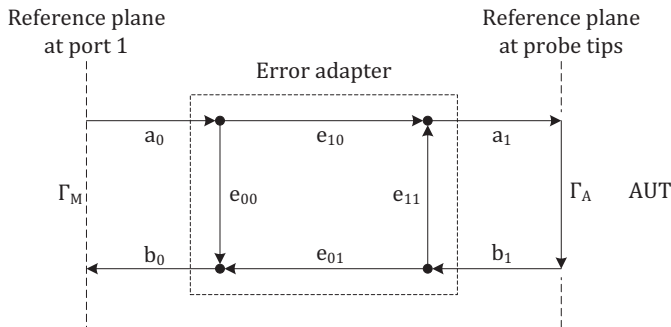
Figure 2.15: 1-port SOL calibration error model.

a standard calibration substrate. The 1-port SOL error model is shown in Figure 2.15. The relationship between the measured reflection coefficient Γ_M with error and the actual reflection coefficient Γ_A at the device itself at the reference plane can be written as [60]

$$\Gamma_M = \frac{b_0}{a_0} = e_{00} + \frac{e_{10}e_{01}\Gamma_A}{1 - e_{11}\Gamma_A} \qquad (2.51a)$$

$$\Gamma_A = \frac{\Gamma_M - e_{00}}{e_{11}(\Gamma_M - e_{00}) + e_{10}e_{01}} \qquad (2.51b)$$

$\Gamma_{M,short}$, $\Gamma_{M,open}$, and $\Gamma_{M,load}$ can be obtained by measuring the short, open, and load calibration standards on the calibration substrate, while $\Gamma_{A,short}$, $\Gamma_{A,open}$,

and $\Gamma_{A,load}$ are the known calibration standard values. They yield three equations with three unknown error factors (e_{00}, e_{11}, and $e_{10}e_{01}$) so that the unknown error factors can be determined by calculation. Knowing the error factors, Γ_A can be calculated from Γ_M in the antenna measurements. Assuming the error adapter is perfectly reciprocal ($e_{10} = e_{01}$), the gain of the probe can be expressed as

$$G_{probe} = e_{10}e_{01} \qquad (2.52)$$

Finally the antenna measurement can be implemented as shown in Figure 2.14 (c), and the proper gain G_{AUT} of the AUT can be calculated from the directly measured result $S_{21,M}$ as

$$G_{AUT} = \frac{|S_{21,M}|^2}{G_{system} \cdot G_{probe}} \qquad (2.53)$$

2.5   Preliminary Considerations on mm-Wave Antenna Design and Integration

The integration of antenna into an mm-Wave system takes a vital role, and is very challenging. Many methods and technologies for mm-Wave packaging and antenna integration have been developed, which are discussed below.

2.5.1   Chip-on-Board with Integrated PCB Antenna

Figure 2.16 (a) and (b) illustrate the concept of a RFIC, which is directly attached on a PCB, incorporating with an integrated PCB antenna by using mm-Wave interconnect technologies, bond-wire and flip-chip, respectively. As shown in Figure 2.16 (a) the chip is glued on the ground plane of the PCB, which also acts as a large heat sink for the chip. The RF I/O of the chip is interconnected to the antenna by wire-bonding. The wire-bonding is a mature, thermal expansion insensitive, and high yield process that supports a well-established low-cost infrastructure with high reliability. Unfortunately, the electrically long loop of the bond-wires will introduce considerable parasitic effects (about 1 nH/mm of inductance as a rule of thumb) so that they exhibit low-pass frequency characteristics in the mm-Wave range. The bond-wire with short length is difficult to produce, and the repeatability is a serious issue. Consequently, special compensation designs and process control for bond-wires have to be applied in order to achieve acceptable performance within the bandwidth of interest [26] [61] which increase the assembly complexity, and the cost. As frequencies increase to above 100 GHz or even above 200 GHz the compensation for bond-wires becomes much more difficult (requires very precise fabrication technology and process control), if it is not impossible.
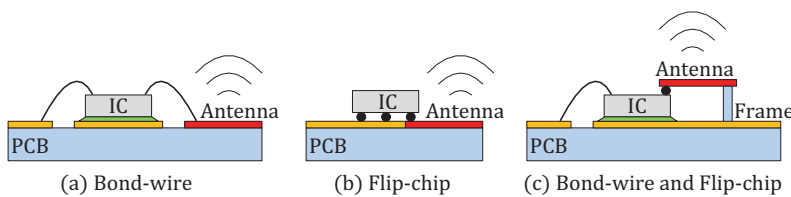
Figure 2.16: Chip-on-board with integrated PCB antenna by using: (a) bond-wire solution, (b) flip-chip solution, (c) bond-wire and flip-chip solution.

Figure 2.16 (b) shows a flip-chip solution with bump interconnects, which offers a very short transition between the chip and the PCB antenna. Therefore, the parasitic effects associated with a bump itself are significantly smaller than that of a bond-wire, showing a wide application potential at mm-Wave frequencies above 100 GHz and even higher up to 170 GHz with a compensation scheme [62] [63]. Moreover, the bumps can be placed on the entire die area that it enables a much higher I/O count compared with that of the bond-wire solution, which can only use the periphery of the chip. The density of the bumps will be constrained by the normal PCB manufacturing technology whose minimum line width and spacing are limited to about 100 μm. The flipped-over chip mounting onto an underlying PCB gives other types of parasitic problems. They can result in considerable deterioration in performance of the overall packaged mm-Wave system if special cares are not taken in the designs. Obviously, the electrical parameters of various circuit elements on the chip surface, e.g. inductors, couplers or any structures made of transmission lines, will be influenced by the proximity effects to the PCB, especially when a metallization is present on the PCB below the chip [64], thus causing chip detuning. The different coefficient of thermal expansion (CTE) of the chip and the PCB material can cause a strain on the flip-chip joints that arises reliability issues, so an underfill process (e.g. a thermal compression technology) is often required to absorb the stress. The price is that the underfill materials will probably introduce additional detuning effects as well as more losses. Another problem has to be considered is that unlike the case of a chip directly seating on a large heat sink (metal ground plane) on a PCB, the upside-down configuration of the chip has limited heat dissipation capability that could result in severe performance degradation of the RF circuits.

A combination of the bond-wire and flip-chip technologies can take the advantages of both technologies as shown in Figure 2.16 (c). The low frequency I/O and DC supplies of the chip, which are not sensitive to the parasitics, can be interconnected to the PCB by wire-bonding. The antenna and the RF I/O of the chip, which are operating at the highest frequencies of the system, are interconnected by flip-chip bumps. The effects of the supporter of the antenna must be taken into account in the design. In [65] a covar metal frame (rectangle

ring type) is used to mechanically support the antenna, and the metal frame to-gether with the metallic base of the board form a metal cavity which provides a well-controlled EM environment, making the antenna less sensitive to the sur-rounding package and PCB-level metal as well as dielectric structures. Another advantage of this hybrid approach is that an optimal substrate preferably with low dielectric constant and thicker thickness, which are usually contradictory to the requirements of other on-board RF passive circuits, can be used for the antenna since they are not implemented on the same substrate. Apparently, the packaging and assembly process of the hybrid approach is more complex than that of a bond-wire or flip-chip solution, resulting in a higher cost.

The chip-on-board (COB) with integrated PCB antenna is a very cost-effective solution since there are a wide range of low-cost and high-quality RF substrates available in the market, and the PCB technologies are quite well-established. The parasitic effects introduced by the chip-antenna interconnect technologies of wire-bonding or flip-chip can be compensated up to certain frequencies on the board side in a cost-effective fashion. However, the resolution (e.g. mini-mum line width and spacing are about 100 μm) and accuracy of normal PCB technologies limit its applications within the lower band of mm-Wave frequen-cies. In addition, this method requires mm-Wave expertise in the PCB design and additional molding process (e.g. glob top [65]) to protect the chip and the interconnects from mechanical damage and contamination. Nevertheless, it can be expected that the COB with integrated PCB antenna solution gives better performance than other packaging methods because of fewer signal transfer stages (the I/O of the chip is interconnected to the PCB directly), flexibility in on-board antenna design, and larger possible heat sink. All these characteristics make this approach very commonly used for mm-Wave system demonstrators to evaluate the system performance. The designs for 60 GHz applications based on this method will be demonstrated in chapter 3.

2.5.2   Antenna Integrated In-Package and Antenna Integrated On-Chip

For mass products it is highly desirable to have an mm-Wave system with inte-grated antenna in a package. In the mm-Wave range the size of the antenna de-creases into millimeter range, so it is feasible to integrate it into a small pack-age or even on-chip. In this case the package confines all high frequency interconnects inside itself so that only the low frequencies and DC supplies are transferred between the package and the next level platform, which requires significantly less efforts and little high frequency expertise. Therefore, the sur-face mount technology (SMT) can be used to mount the packages in the same way as other SMT components directly onto the surface of a low-cost PCB mother board, enabling mass products.

There are several packaging and antenna integration technologies available for mm-Wave applications, such as low temperature co-fired ceramic (LTCC) [66] [67] packages, silicon based packages [68] [69], land-grid-array (LGA) packages [70], plastic quad flat no-lead (QFN) packages [71], etc. Among them the plastic QFN package is the simplest and probably the cheapest. The following discussion on antenna integration in-package is based on a QFN package as an example, but many conclusions can also be applied on other package platforms (e.g. parasitic effects of wire-bonding and flip-chip technologies).

Figure 2.17 shows an example of very low-cost plastic air cavity QFN package (10 mm × 10 mm × 0.635 mm) with a typical pin pitch of 0.5 mm from the market [72], which is compatible with SMT process. There are more standard and customized sizes available to accommodate chips and antennas with different sizes. The larger center metal pad can act as a good heat sink for the chip to transfer the heat from the package to the outside PCB, and it can also serve as a reflector for the in-package antenna to enhance the broadside radiation. This package can be encapsulated by filling of molding compound or closed by a flat lid or a dome. The molding compound is usually very lossy at mm-Wave frequencies, and can introduce uncertainties to the antenna's behavior [65]. A lid can be made of various dielectric materials (e.g. plastic, glass, ceramic alumina, etc.) with standard or customized sizes and thicknesses. It has been demonstrated in [71] that a lid with a thickness of half-wavelength ($d = 0.5\lambda_g$) has little influence on the radiation performance of the in-package antenna, thus being a recommended solution. The reason is that the reflections of the radiated wave at the air-lid (dielectric) interface can be analyzed by a transmission line method [73]. That is when the radiated wave incident at the air-lid interface normally or the incident angle is small the flat lid sheet acts as a half-wavelength transmission line with wave impedance Z_{lid}, which transforms the free-space wave impedance Z_0 outside the package onto itself inside the package, thus theoretically no reflections.
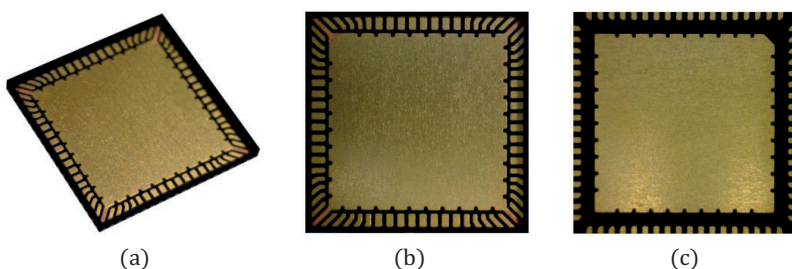

Figure 2.17: A plastic air cavity quad flat no-lead (QFN) package (10 mm × 10 mm × 0.635 mm) with a pin pitch of 0.5 mm [72]: (a) perspective view, (b) top view, (c) bottom view.
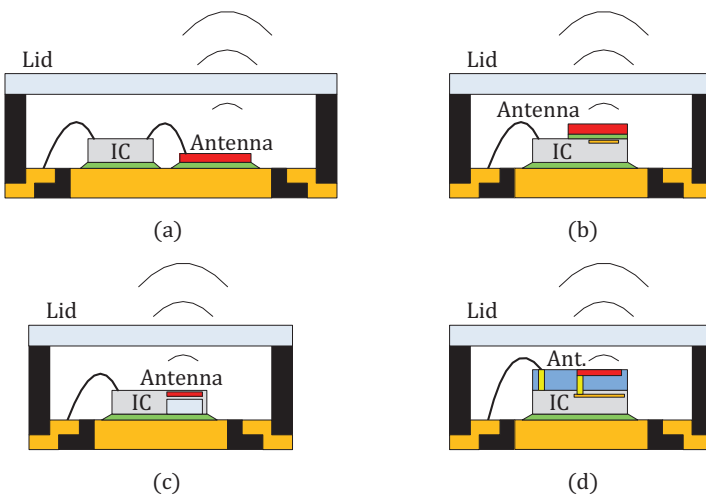
Figure 2.18: Antenna integration concepts based on a QFN package: (a) antenna on dielectric, (b) antenna on superstrate or dielectric resonator antenna, (c) antenna on-chip with localized backside etching process, (d) antenna fabricated in an above-wafer process.

Figure 2.18 shows some examples of possible antenna integration concepts based on a QFN package. In Figure 2.18 (a) an antenna is fabricated on a thin dielectric, and glued on the center pad of the package with epoxy adhesive. The antenna and the chip are interconnected by wire-bonding, but in fact any chip-on-board and PCB antenna integration methods shown in Figure 2.16 can be applied in this package. Since a suitable high-quality dielectric and advanced fabrication technology can be used for the antenna, and it is flexible to configure the antenna like making a metallized air cavity on the center pad of the QFN package below the antenna [71], the antenna on dielectric method can give very good radiation performance (e.g. an antenna radiation efficiency of 75% including the bond-wire loss was achieved for 122 GHz applications in [71]). The low frequency I/Os and DC supplies of the chip are interconnected to the inner pins of the package by wire-bonding, and transferred to the outer pins. For a flip-chip approach the chip can be attached to the dielectric of the antenna (or an interposer layer), and the low frequency I/Os as well as the DC supplies are spread out by transmission lines on the dielectric, and then wire-bonded to the pins of the package. Obviously, all the RF packaging problems related to bond-wire or flip-chip technologies also exist here.

To avoid using the complex RF interconnect processes, the antenna has to be implemented on-chip as shown in Figure 2.18 (b)–(d). In these cases only the low frequency signals and DC supplies are required to be transferred between the chip and package by simple bond-wires, thus greatly reducing the difficulty

in packaging. The challenges come from the design of on-chip antennas. The BEOL process of silicon technologies usually offer several metal layers buried in an insulator (silicon dioxide or its variations) on a chip, which can be used to design antennas. However, it is well-known that on low-resistivity silicon antennas have very low radiation efficiency (<15%) due to the high losses and substrate wave effects of the silicon substrate used in CMOS or BiCMOS technologies. In addition, the insulator layer is too thin (~15 µm) to make a ground shielded (from lossy silicon) antenna with acceptable radiation efficiency (~10%) [74]. Extensive study and research have been conducted to improve the performance of the on-chip antennas. The details will be discussed in chapter 4 and chapter 5, while some concepts are described here.

Figure 2.18 (b) shows the concept of superstrate antennas or dielectric resonator antennas (DRA) glued on top of the chip, which are excited by on-chip transmission lines or on-chip antennas through electromagnetic coupling. The radiation efficiency of the antennas was improved to 40–60% as reported in [75]–[77]. This method requires relatively precise alignment and gluing process to place the superstrate or dielectric antenna on the right position of the chip, which adds cost to the antenna-chip assembly. The antenna is vertically positioned on the chip, so it does not occupy the chip or package area, enabling a more compact chip size.

In Figure 2.18 (c) an antenna is fabricated by the BEOL process within the chip, and it can be directly integrated with the active circuits by on-chip interconnects like microstrip transmission lines or CPW lines. The on-chip interconnects have much higher fabrication precision, bandwidth and reliability with little parasitic effects than any off-chip RF interconnects so that they can work at the higher band of mm-Wave and even up to submillimeter-wave region. The radiation efficiency of the on-chip antenna is improved by selectively removing the lossy silicon in critical areas by applying an LBE process. The LBE process is part of standard through silicon vias (TSVs) technology, and is available in a variety of commercial semiconductor technologies as well as all of IHP's SiGe BiCMOS technologies. This process is based on deep reactive ion etching (DRIE) technology, which enables very high aspect ratio, thus allowing the etched areas with arbitrary shapes in the close vicinity of the active devices. The packaging and assembly procedure for this concept is extremely simple, but a considerably larger chip area, which is expensive for low volume production, is needed since no active devices can be placed under the antenna or in the etched areas. Therefore, the on-chip antenna with LBE process is more suitable for higher frequency applications, specifically above 100 GHz which leads to a smaller form factor for the antennas. There is compromise between the antenna performance and mechanical stability. It is desired to have a larger silicon etched area to enhance the radiation efficiency and bandwidth,

but the mechanical stability will be reduced in this way since the very thin membrane (silicon dioxide) is fragile without the support of silicon. In chapter 4 several on-chip antenna designs with LBE process as well as fully integrated mm-Wave transceivers are presented, targeting higher performance, better mechanical stability, and more compact size.

Figure 2.18 (d) demonstrates another approach to integrate an antenna onto an IC with improved radiation efficiency by applying wafer-level integration technology. Several polymer layers as well as metal layers are deposited on the silicon wafer as a post-wafer process. BCB is a widely used polymer for mm-Wave applications in the thin-film multilayer multichip module with deposited interconnects (MCM-D) technology due to its low losses, lower mechanical stress, and better planarization [78]–[80]. The metal layers in the BCB and in the BEOL process of the silicon technology can be interconnected by vias with extremely high precision, small feature size, low parasitic effects, and low-loss. The antennas are realized in the thick copper layers in the BCB with ground shielding, which shields the antennas from the lossy silicon. In this way the radiation efficiency of the antennas is considerably higher than that of antennas realized on ordinary low-resistivity silicon. As the antenna can be placed on top of the chip, it does not increase much of the chip size. However, currently the total thickness of the deposited BCB is usually within several tens of micrometers, which limits the antenna bandwidth and further improvement of efficiency. Antenna designs based on this method for 122 GHz applications are presented in chapter 5.

2.6   Design Flow and Methodology

A successful design of integrated mm-Wave antenna is a systematic work. A design flow and methodology is proposed by condensing the design experience from this thesis work into a methodology as shown Figure 2.19. The principle of the design methodology is that from simpler structures to more complex structures, and from cheaper (computer simulation based) task to more expensive task (e.g. interconnects characterization, dielectric characterization, prototype manufacture, etc.). In this way we expect to save the development time and cost by minimizing complete re-design cycles and prototype hardware fabrications.

First, design specifications have to be defined, which can be divided into two categories: the applications of the design and the technical requirements of the design. The design applications will determine, to large extent, which packaging and antenna integration method is preferred to use. For instance the chip-on-board with integrated PCB antenna as illustrated in Figure 2.16 is a suitable

```
                    ┌─────────────────────────────────┐
                    │    Define design specifications  │
                    └─────────────────────────────────┘
                                   ↓
                    ┌─────────────────────────────────────────────┐
           ┌───────►│ Decide packaging and antenna integration method │
           │        └─────────────────────────────────────────────┘
 ┌──────────────┐                  ↓
 │Consider other│   ┌─────────────────────────────────────────────┐
 │  approaches  │   │ Preliminarily design by 3-D EM simulation   │
 └──────────────┘   └─────────────────────────────────────────────┘
           ▲                       ↓
           │    No    ◇ Can design specifications be fullfilled? ◇
           └──────────
                              Yes ↓
                    ┌─────────────────────────────────────────────┐
                    │ Packaging and substrate materials characterization │
                    └─────────────────────────────────────────────┘
                                   ↓
                    ┌─────────────────────────────────────────────┐
           ┌───────►│ Thoroughly design by 3-D EM simulation      │◄──┐
           │        └─────────────────────────────────────────────┘   │
           │    No    ◇ Can design specifications be fullfilled? ◇    │
           └──────────                                                 │
                              Yes ↓                          ┌──────────────┐
                    ┌─────────────────────────────────────┐  │ Identify the │
                    │ Prototype manufacture and measurement│  │   problems   │
                    └─────────────────────────────────────┘  └──────────────┘
                                   ↓                                   ▲
                          ◇ Results satisfactory? ◇ ──── No ──────────┘
                              Yes ↓
                    ┌─────────────────────────────────┐
                    │        Design finished          │
                    └─────────────────────────────────┘
```

Figure 2.19: Integrated mm-Wave antenna design flow.

approach for 60 GHz system demonstrator applications in the preliminary development phase due to its high performance, ease of realization, and low-cost for in-house system evaluation. In contrast, if the design targets mass products a compact and low-cost mm-Wave system in-package as shown in Figure 2.18 is more desired. When the application is above 200 GHz an antenna on-chip solution is the most attractive. The technical requirements are defined from a system point of view. It usually includes the radiation direction, operation bandwidth, antenna gain, beamwidth, etc., which have been introduced in section 2.1.

As soon as the design specifications have been fixed, the packaging and antenna integration method has to be determined with comprehensively considering the discussions in section 2.5. And then, preliminary design can be started. The substrate waves were theoretically studied in section 2.3.2, offering references for selecting the appropriate substrates for the planar antenna designs. Analytical closed form solutions are only valid for simple antenna structures operating in simplified environment as discussed in section 2.2, although they do offer insight into the principle of the antenna operation and the direction for optimization. In practice the planar antenna and its operating environment are much more complex so that numerical approaches are indispensable. Three dimensional full-wave electromagnetic (3-D EM) simulators of ANSYS HFSS frequency domain solver based on the finite element method (FEM) [81], and

CST microwave studio transient solver based on the finite integration technique (FIT) [82] are employed in the designs. Both simulators can give accurate prediction of S-parameter and near/far-field results, which have been proven in many designs world widely. The preliminary design is the conceptual verification and performance evaluation of the selected packaging and antenna integration method. In this procedure some structures or factors with less influence over the performance can be simplified or even excluded in the simulated model to shorten the simulation time, thus enabling more simulations to study more possible structures.

After implementing extensive simulations based on the selected method we can have a general idea of whether the design specifications can be fulfilled or not. If not, we have to re-consider other packaging and antenna integration methods. (For example, if we found it too difficult to compensate the bond-wire with acceptable performance in the operation band, we have to consider the flip-chip or antenna on-chip solutions.) If yes, we proceed with the design into a more thorough way. The materials for packaging and dielectrics for antenna are characterized in the frequency band of interest by applying a suitable method (reviewed in section 2.3.1) when there are no reliable dielectric property data from the manufacturers or literature. The packaging interconnects are also characterized in terms of their electrical performance, possible fabrication tolerance, reliability, repeatability, etc. Knowing all necessary information thorough design can be conducted. In the simulations all structures including the antennas, dielectrics, interconnects, and anything could have influence over the performance are 3-dimensionally modeled as their physical dimensions with the correct material properties. After optimizing the design, if the results can fulfill the design specifications we can proceed to manufacture prototypes. Otherwise, re-consider the packaging and integration method. The measurement plan should be included in the design procedure to guarantee a testable prototype, and the influence of the measurement structures (e.g. probing pads) can be de-embedded out from the final results. The antenna measurement setup and its calibration procedure were introduced in section 2.4. After the measurements we should consider if the results are satisfactory because they can deviate from the design due to manufacture tolerance or any other un-considered factors which make the prototype different from the model in simulations. If the results are not acceptable we have to identify the problems first, and then adjust the simulation accordingly which calls for a re-design cycle.

2.7   Conclusions

This chapter introduced the most important antenna parameters with the emphasis on their effects in mm-Wave systems. They must be thoroughly considered and balanced to meet the design specifications for a certain application.

Some planar antenna models were theoretically studied, which offered insight into the operation principle of the presented antennas in this thesis as well as the directions for the antenna optimization. The substrate takes an essential role in planar antenna designs. A variety of dielectric characterization techniques were reviewed, and the excitation and propagation of substrate waves were investigated. The probe based antenna measurement setup and its special calibration procedure were depicted. The state-of-the-art antenna integration and packaging methods were extensively reviewed and discussed regarding their advantages and limitations. By considering all the aforementioned factors and condensing the design experience in this thesis work into a methodology a design flow and methodology was proposed in the end of the this chapter.

References

[1]   S. Beer, and T. Zwick, "Probe based radiation pattern measurements for highly integrated millimeter-wave antennas," *Antennas and Propagation*, *2010 Proceedings of the Fourth European Conference on*, pp. 1-5, Apr. 2010.

[2]   C. A. Blanis, *Antenna Theory: Analysis and Design*, 3rd edition, John Wiley & Sons, New York, 2005.

[3]   Shamim, L. Roy, N. Fong, and N. G. Tarr, "24 GHz on-chip antennas and balun on bulk Si for air transmission," *Antennas and Propagation*, *IEEE Transactions on*, vol. 56 , no. 2, pp. 303-311, Feb. 2008.

[4]   D. Pozar, *Microwave Engineering*, 4th edition, John Wiley & Sons, New York, 2011.

[5]   J. D. Kraus, *Antennas*, McGraw-Hill, New York, 1988.

[6]   C. –T. Tai, and C. S. Pereira, "An approximate formula for calculating the directivity of an antenna," *Antennas and Propagation*, *IEEE Transactions on*, vol. AP-24, no. 2, pp. 235-236, Mar. 1976.

[7]   R. S. Elliott, "Beamwidth with directivity of large scanning arrays," *The Microwave Journal*, pp. 74-82, Jan. 1964.

[8]   S. Voinigescu, *High-frequency integrated circuits*, Cambridge University Press, Cambridge, 2013.

[9]   P. Herrero, and J. Schoebel, "Planar antennas and beamforming devices for a multi gigabit 60 GHz demonstrator with quality of service," *Antennas and Propagation*, *2010 Proceedings of the Fourth European Conference on*, pp. 1-5, Apr. 2010.

[10] A. Valdes-Garcia *et al.*, "A SiGe BiCMOS 16-element phased-array transmitter for 60GHz communications," *ISSCC*, *2010 IEEE International-al*, pp. 218-219, Feb. 2010.

[11] S. Emami *et al.*, "A 60GHz CMOS phased-array transceiver pair for multi-Gb/s wireless communications," *ISSCC, 2011 IEEE International*, pp. 164-166, Feb. 2011.

[12] S. Yoshida *et al.*, "A 60-GHz band planar dipole array antenna using 3-D SiP structure in small wireless terminals for beamforming applications," *Antennas and Propagation*, *IEEE Transactions on*, vol. 61, no. 7, pp. 3502-3510, July 2013.

[13] G. H. Brown, and O. M. Woodward, Jr., "Experimentally determined impedance characteristics of cylindrical antennas," *Proceedings of the IRE*, vol. 33, no. 4, pp. 257-262, Apr. 1945.

[14] G. A. Thiele, E. P. Ekelman Jr., and L. W. Henderson, "On the accuracy of the transmission line model for folded dipoles," *Antennas and Propagation*, *IEEE Transactions on*, vol. 28, no. 5, pp. 700-703, Sep. 1980.

[15] R. W. Lampe, "Design formulas for an asymmetrical coplanar strip folded dipole," *Antennas and Propagation*, *IEEE Transactions on*, vol. 33, no. 9, pp. 1028-1031, Sep. 1985.

[16] J. F. Zücher, and F. E. Gardiol, *Broadband patch antennas*, Artech House, MA, 1995.

[17] R. Wang, Y. Sun, M. Kaynak, J. Borngräber, B. Göttel, S. Beer, and J. C. Scheytt, "122 GHz patch antenna designs by using BCB above SiGe BiCMOS wafer process for system-on-chip applications," *2013 IEEE International Symposium on Personal, Indoor and Mobile Radio Communications*, London, pp. 1392-1396, Sep. 2013.

[18] A. S. Emhemmed, I. McGregor, and K. Elgaid, "200GHz broadband proximity coupled patch antenna," *Ultra-Wideband 2009*, *IEEE International Conference on*, pp. 404-407, Vancouver, Sep. 2009.

[19] M. Himdi, O. Lafond, S. Laignier, and J. P. Daniel, "Extension of cavity method to analyse aperture coupled microstrip patch antenna with thick ground plane," *Electronics Letters*, vol. 34, no. 16, pp. 1534-1536, Aug. 1998.

[20] K. –L. Wong, and W. – H. Hsu, "A broad-band rectangular patch antenna with a pair of wide slits," *Antennas and Propagation*, *IEEE Transactions on*, vol. 49, no. 9, pp. 1345-1347, Sep. 2001.

[21] J. Huang, P. Yang, W. C. Chew, and T. Ye, "A compact broadband patch antenna for UHF RFID tags," *2009 Asia Pacific Microwave Conference*, pp. 1044-1047, Singapore, Dec. 2009.

[22] G. Rafi, and L. Shafai, "Broadband microstrip patch antenna with V-slot," *Microwaves, Antennas and Propagation*, *IEE Proceedings*, vol. 151, no. 5, pp. 435-440, Oct. 2004.

[23] J. –Y. Sze, and K. –L. Wong, "Broadband rectangular microstrip antenna with pair of toothbrush-shaped slots," *Electronics Letters*, vol. 34, no. 23, pp. 2186-2187, Nov. 1998.

[24] C. K. Aanandan, and K. G. Nair, "Compact broadband microstrip antenna," *Electronics Letters*, vol. 22, no. 20, pp. 1064-1065, Sep. 1986.

[25] G. Kumar, and K. C. Gupta, "Directly coupled multiple resonator wideband microstrip antennas," *Antennas and Propagation*, *IEEE Transactions on*, vol. 33, no. 6, pp. 588-593, Jun. 1985.

[26] R. Wang, Y. Sun, C. Wipf, and J. C. Scheytt, " An on-board differential patch antenna and interconnects design for 60 GHz applications," *2011 IEEE International Conference on Microwaves, Communications, Antennas and Electronics System*, pp. 1-5, Tel Aviv, Nov. 2011.

[27] A. Lamminen, and J. Saily, "Wideband stacked patch antenna array on LTCC for W-band," *Antennas and Propagation*, *Proceedings of the 5th European Conference on*, pp. 2962-2966, Rome, Apr. 2011.

[28] K. Li, C. H. Cheng, K. F. Tong, and T. Matsui, "Broadband stacked coplanar patch antennas," *2001 31st European Microwave Conference*, pp. 1-4, London, Sep. 2001.

[29] A. G. Derneryd, "A theoretical investigation of the rectangular microstrip antenna element," *Antennas and Propagation*, *IEEE Transactions on*, vol. 26, no. 4, pp. 532-535, Jul. 1978.

[30] K. R. Carver, and J. Mink, "Microstrip antenna technology," *Antennas and Propagation*, *IEEE Transactions on*, vol. 29, no. 1, pp. 2-24, Jan. 1981.

[31] D. H. Schaubert, D. M. Pozar, and A. Adrian, "Effect of microstrip antenna substrate thickness and permittivity: comparison of theories and experiment," *Antennas and Propagation*, *IEEE Transactions on*, vol. 37, no. 6, pp. 677-682, Jun. 1989.

[32] E. O. Hammerstad, "Equations for microstrip circuit design," *5th European Microwave Conference*, pp. 268-272, Sep. 1975.

[33] I. J. Bahl, and P. Bhartia, *Microstrip Antennas*, Artech House, MA, 1980.

[34] P. J. Gibson, "The Vivaldi aerial," *9th European Microwave Conference*, pp. 101-105, Sep. 1979.

[35] K. S. Yngvesson, D. H. Schaubert, T. L. Korzeniowski, E. L. Kollberg, T. Thungren, and J. F. Johansson, "Endfire tapered slot antennas on dielectric substrates," *Antennas and Propagation*, *IEEE Transactions on*, vol. 33, no. 12, pp. 1392-1400, Dec. 1985.

[36] F. J. Zucker, "Surface- and leaky-wave antennas," *Antenna Engineering Handbook*, H. Jasik, Ed. McGraw-Hill, New York, 1961.

[37] J. D. S. Langley, P. S. Hall, and P. Newham, "Balanced antipodal Vivaldi antenna for wide bandwidth phased arrays," *Microwaves, Antennas and Propagation*, *IEE Proceedings*, vol. 143, no. 2, pp. 97-102, Apr. 1996.

[38] Joon Shin, and D. H. Schaubert, "A parameter study of stripline-fed Vivaldi notch-antenna arrays," *Antennas and Propagation*, *IEEE Transactions on*, vol. 47, no. 5, pp. 879-886, May 1999.

[39] E. Gazit, "Improved design of the Vivaldi antenna," *Microwaves, Antennas and Propagation*, *IEE Proceedings*, vol. 135, no. 2, pp. 89-92, Apr. 1988.

[40] J. J. Lee, and S. Livingston, "Wide band bunny-ear radiating element," *Antennas and Propagation Society International Symposium*, *1993. AP-S. Digest*, vol. 3, pp. 1604-1607, 28 Jun.-02 Jul. 1993.

[41] M. C. Greenberg, and K. L. Virga, "Characterization of bunny-ear antennas for wireless basestation applications," *Radio and Wireless Conference*, 1998, pp. 87-90, Aug. 1998.

[42] M. C. Greenberg, and K. L. Virga, "Characterization and design methodology for the dual exponential tapered slot antenna," *Antennas and Propagation Society International Symposium*, *1999 IEEE*, vol. 1, pp. 88-91, Jul. 1999.

[43] D. Pozar, "Considerations for millimeter wave printed antennas," *Antennas and Propagation*, *IEEE Transactions on*, vol. 31, no. 5, pp. 740-747, Sep. 1983.

[44] P. Debye, *Polar Molecules*, Chemical Catalog Co., New York, 1929.

[45] T. Zwick, A. Chandrasekhar, C. W. Baks, U. R. Pfeiffer, S. Brebels, and B. P. Gaucher, "Determination of the complex permittivity of packaging materials at millimeter-wave frequencies," *Microwave Theory and Techniques*, *IEEE Transactions on*, vol. 54, no. 3, pp. 1001-1010, Mar. 2006.

[46] M. N. Afsar, "Dielectric measurements of millimeter-wave materials," *Microwave Theory and Techniques*, *IEEE Transactions on*, vol. 32, no. 12, pp. 1598-1609, Dec. 1984.

[47] N. J. Damaskos, and B. J. Kelsall, "Cavity techniques for substrate properties at microwave/millimeter-wave bands," *Microwave Journal*, pp. 112-124, Dec. 2003.

[48] R. G. Jones, "Precise dielectric measurements at 35 GHz using an open microwave resonator," *Electrical Engineerings*, *Proceedings of the Institution of*, vol. 123, no. 4, Apr. 1976.

[49] I. Wolff, and N. Knoppik, "Microstrip ring resonator and dispersion measurement on microstrip lines," *Electronics Letters*, vol. 7, no. 26, pp. 779-781, Dec. 1971.

[50] D. K. Ghodgaonkar, V. V. Varadan, and V. K. Varadan, "A free-space method for measurement of dielectric constants and loss tangents at microwave frequencies," *Instrumentation and Measurement*, *IEEE Transactions on*, vol. 38, no. 3, pp. 789-793, Jun. 1989.

[51] D. K. Ghodgaonkar, V. V. Varadan, and V. K. Varadan, "Free-space measurement of complex permittivity and complex permeability of magnetic materials at microwave frequencies," *Instrumentation and measurement*, *IEEE Transactions on*, vol. 39, no. 2, Apr. 1990.

[52] Y. Y. Lim, M. D, Rotaru, A. Alphones, and A. P. Popov, "Simple and improved dielectric parameter extraction of thin organic packaging materials using open-ended coaxial line technique," *Microwaves, Antennas and Propagation*, *IEE Proceedings*, vol. 152, no. 4, pp. 214-220, Aug. 2005.

[53] W. B. Weir, "Automatic measurement of complex dielectric constant and permeability at microwave frequencies," *Proceedings of the IEEE*, vol. 62, no. 1, pp. 33-36, Jan. 1974.

[54] M. D. Janezic, and J. A. Jargon, "Complex permittivity determination from propagation constant measurements," *Microwave and Guided Wave Letters*, *IEEE*, vol. 9, no. 2, pp. 76-78, Feb. 1999.

[55] A. M. Mangan, S. P. Voinigescu, M. –T. Yang, and M. Tazlauanu, "De-embedding transmission line measurements for accurate modeling of IC designs," *Electron Devices*, *IEEE Transactions on*, vol. 53, no. 2, pp. 235-241, Feb. 2006.

[56] M. D. janezic, and D. F. Williams, "Permittivity characterization from transmission-line measurement," *Microwave Symposium Digest 1997*, *IEEE MTT-S International*, vol. 3, pp. 1343-1346, Jun. 1997.

[57] D. B. Rutledge, and M. S. Muha, "Imaging antenna arrays," *Antennas and Propagation*, *IEEE Transactions on*, vol. 30, no. 4, pp. 535-540, Jul. 1982.

[58] I. J. Bahl, and D. K. Trivedi, "A designer's guide to microstrip line," *Microwaves*, pp. 174-182, May 1977.

[59] S. Beer, H. Gulan, C. Rusch, G. Adamiuk, and T. Zwick, "A double-dipole antenna with parasitic elements for 122 GHz system-in-package radar sensors," *Antennas and Propagation*, *Proceedings of the 5th European Conference on*, pp. 1903-1906, Apr. 2011.

[60] D. Liu, B. Gaucher, U. Pfeiffer, and J. Grzyb, *Advanced Millimeter-wave Technologies: Antennas, Packaging and Circuits*, John Wiley & Sons Ltd., 2009.

[61] S. Beer, H. Gulan, M. Pauli, C. Rusch, G. Kunkel, and T. Zwick, "122-GHz chip-antenna wire bond interconnect with high repeatability," *Microwave Symposium Digest*, *2012 IEEE MTT-S International*, pp. 1-3, Jun. 2012.

[62] A. Jentzsch, and W. Heinrich, "Theory and measurements of flip-chip interconnects for frequencies up to 100 GHz," *Microwave Theory and Techniques*, *IEEE Transactions on*, vol. 49, no. 5, pp. 871-878, May 2001.

[63] S. Beer, and T. Zwick, "122 GHz antenna-integration in a plastic package based on a flip chip interconnect," *Microwave Workshop Series on Millimeter Wave Integration Technologies*, *2011 IEEE MTT-S International*, pp. 37-40, Sep. 2011.

[64] W. Heinrich, A. Jentzsch, and G. Baumann, "Millimeter-wave characteristics of flip-chip interconnects for multichip modules," *Microwave Theory and Techniques*, *IEEE Transactions on*, vol. 46, no. 12, Dec. 1998.

[65] U. Pfeiffer, J. Grzyb, D. Liu, B. Gaucher, T. Beukema, B. A. Floyd, and S. K. Reynolds, "A chip-scale packaging technology for 60-GHz wireless chipsets," *Microwave Theory and Techniques*, *IEEE Transactions on*, vol. 54, no. 8, pp. 3387-3397, Aug. 2006.

[66] Y. P. Zhang, "60-GHz antenna-in-package technology," *Electrical Design of Advanced Packaging & Systems Symposium*, *2009 IEEE*, pp. 1-4, Dec. 2009.

[67] D. G. Kam, D. Liu, A. Natarajan, S. Reynolds, and B. A. Floyd, "Low-cost antenna-in-package solutions for 60-GHz phased-array systems," *Electrical Performance of Electronic Packaging and Systems (EPEPS)*, *2010 IEEE 19th Conference on*, pp. 93-96, Oct. 2010.

[68] C. Jin, V. N. Sekhar, X. Bao, B. Chen, B. Zheng, and R. Li, "Antenna-in-package design based on wafer-level packaging with through silicon via technology," *Components, Packaging and Manufacturing Technology*, *IEEE Transactions on*, vol. 3, no. 9, pp. 1498-1505, Jun. 2013.

[69] N. Hivik *et al.*, "High-efficiency 60 GHz antenna fabrication using low-cost silicon micromachining techniques," *Antennas and Propagation Society International Symposium*, *2007 IEEE*, pp. 5043-5046, Jun. 2007.

[70] U. Pfeiffer, J. Grzyb, D. Liu, B. Gaucher, T. Beukema, B. Floyd, and S. Reynolds, "A 60 GHz radio chipset fully-integrated in a low-cost packaging technology," *Electronic Components and Technology Conference*, *2006. Proceedings. 56th*, pp. 1343-1346, May-Jun. 2006.

[71] S. Beer, H. Gulan, C. Rusch, and T. Zwick, "Coplanar 122-GHz antenna array with air cavity reflector for integration in plastic packages," *Antennas and Wireless Propagation Letters*, *IEEE*, vol. 11, pp. 160-163, 2012.

[72] http://www.mirrorsemi.com/M-QFN72W.5.html

[73] D. R. Jackson, and N. G. Alexopoulos, "Gain enhancement methods for printed circuit antennas," *Antennas and Propagation*, *IEEE Transactions on*, vol. 33, no. 9, pp. 976-987, Sep. 1985.

[74] A. Babakhani, X. Guan, A. Komijani, A. Natarajan, and A. Hajimiri, "A 77-GHz phased-array transceiver with on-chip antennas in silicon: receiver and antennas," *Solid-State Circuits*, *IEEE Journal of*, vol. 41, no. 12, pp. 2795-2806, Dec. 2006.

[75] J. Hasch, U. Wostradowski, S. Gaier, and T. Hansen, "77 GHz radar transceiver with dual integrated antenna elements," *German Microwave Conference*, *2010*, pp. 280-283, Mar. 2010.

[76] Y. –C. Ou, and G. M. Rebeiz, "On-chip slot-ring and high-gain horn antennas for millimeter-wave wafer-scale silicon systems," *Microwave The-*

ory and Techniques, *IEEE Transactions on*, vol. 59, no. 8, pp. 1963-1972, Jun. 2011.

[77] D. Hou, Y. –Z. Xiong, W. –L. Goh, S. Hu, W. Hong, and M. Madihian, "130-GHz on-chip meander slot antennas with stacked dielectric resonators in standard CMOS technology," *Antennas and Propagation*, *IEEE Transactions on*, vol. 60, no. 9, pp. 4102-4109, Sep. 2012.

[78] S. B. Yeap, Z. Chen, L. Rui, D. S. W. Ho, and L. T. Guan, "135-GHz co-planar patch array on BCB/silicon with polymer-filled cavity," *Antenna Technology (iWAT)*, *2011 International Workshop on*, pp. 344-347, Mar. 2011.

[79] S. Seok, N. Rolland, and P. –A. Rolland, "A 60 GHz quarter-wave patch antenna based on BCB polymer," *Antennas and Propagation Society International Symposium, 2008*, pp. 1-4, Jul. 2008.

[80] S. Hu, Y. –Z. Xiong, L. Wang, R. Li, and T. G. Lim, "A millimeter-wave wideband high-gain antenna and its 3D system-in-package solution in a TSV-compatible technology," *Electronic Components and Technology Conference, 2011 IEEE 61st*, pp. 869-872, May-Jun. 2011.

[81] http://www.ansys.com/Products/Simulation+Technology/Electromagnetics/Signal+Integrity/ANSYS+HFSS

[82] https://www.cst.com/Products/CSTMWS

3 Integrated PCB Antenna Designs for 60 GHz Applications

3.1 Introduction

At 60 GHz an ISM frequency bandwidth of several gigahertz up to even 9 GHz (i.e. 57–66 GHz in Europe) is unlicensed to use all over the world. The unprecedented available bandwidth creates exciting opportunities for circuit, antenna, and system researchers to realize wireless communication systems with data rates in the order of several gigabits per second, allowing high-definition media transfers. In addition, 60 GHz occurs at a peak in atmospheric attenuation [1] due to the resonance of the molecular oxygen, which makes it best suitable for short range and dense deployment of highest spectral frequency reuse applications. In fact, in recent years with the progress and availability of silicon technologies in the millimeter-wave frequency range, the 60 GHz band has already received intense research, targeting highly-integrated silicon transceivers and high-performance system-in-package. The promise of gigabits per second wireless data transfer and low-cost hardware due to large-scale integration of digital logic with the radiofrequency transceiver on a single die attracts very strong interest of the industry, too. This leads to many standardization activities of 60 GHz including IEEE 802.15.3c, WirelessHD, IEEE 802.11ad, the WiGig standard, and ECMA 387 [2].

The performance and cost of a 60 GHz system is not only determined by the transceiver chips, but also strongly dependent on its packaging and assembly process, specifically the integration of the antenna and the transceiver circuits that has been introduced in Chapter 2. A large number of solutions have been published and proposed. The choice should be made according to design specifications and the application scenarios. There is compromise among the performance, reliability, system integration complexity, and cost. Integrating an antenna on-chip with circuits is the most straight forward way to enable a simple package, since the high-frequency interconnects between the chip and the package are no more needed. However, the on-silicon antennas suffer from very low radiation efficiency which is in the range of 10–15% [3]–[5]. By applying localized backside etching process to remove the lossy silicon under or around the on-chip radiator, the radiation efficiency can be significantly improved. But the form factor of the antenna is increased because of the reduced effective permittivity or additional etched areas, where the active components cannot be placed. The half-wavelength of 60 GHz in free-space is 2.5 mm, which is still too large to implement antennas on-chip with moderate gain and reasonable cost.

Antenna on-board and antenna in-package can achieve much higher efficiency than antenna on-silicon. Commonly used materials and associated technologies for antenna designs are RF PCB [6] [7], LTCC [8]–[10], glass or fused silica [11] [12], and liquid crystal polymer (LCP) [13] [14]. Currently, LTCC is probably the most frequently used technology for antenna in-package applications because it offers low-loss dielectrics and a high degree of integration due to cavities and embedded passives. For all the aforementioned off-chip antenna integration technologies the RF interconnects between the antenna and the chip have to be seriously taken into account in the designs. They should provide good impedance matching and low insertion loss. The mainstream mm-Wave interconnect techniques are wire-bonding and flip-chip. From electrical point of view the bond-wire interconnect is challenging due to its small cross-section and long loop that can introduce loss and destroy impedance matching at 60 GHz. Nonetheless, the wire-bonding process is well-established in consumer electronics, and it is mechanically robust, thermal expansion insensitive, and very cheap, thus remaining a very attractive solution. Interestingly, a bond-wire can be bonded from the RF in/output of the chip to the package or mother board to serve as a low-gain wire antenna for very short-range applications rather than a high frequency interconnect since its length is comparable to the wavelength at 60 GHz [15] [16]. Several bond-wire antennas with power amplifiers (PA) can even form an array in a small form factor to achieve a spatial power combining [17]. In [18] the searchers from Toshiba published a 60 GHz CMOS transceiver chipset with a bond-wire antenna (0 dBi gain) in-package (BGA) that achieved 2.62 Gb/s PHY data rate and 2.07 Gb/s MAC throughput in 3 cm distance. But obviously, the gain of bond-wire antennas is not enough for longer range applications, i.e. several to ten meters. The flip-chip interconnect technique by using bumps, which are much shorter but thicker than bond-wires, has better connection performance than that of wire-bonding. However, it is possible to cause chip detuning.

In the following sections the PCB antenna designs for 60 GHz applications are presented and discussed. They are the cheapest solutions but offering very good performance. The very low-cost RF PCB substrates are characterized, and the packaging issues of RF interconnect are studied. The methodology can also be applied to other materials like the frequently used LTCC. The antennas have been integrated with the transceiver chips to demonstrate the high data rate wireless transmission, and the results prove the good performance of the antenna and its interconnects.

3.2   RF PCB Substrates Characterization and Selection

The selection of substrate is crucial for the success of PCB antenna designs. The substrates should have relatively uniform electrical properties over fre-

quency and temperature, good mechanical stability, feasibility of being processed by standard PCB technology, and tight thickness tolerance besides a low loss tangent and preferably a lower dielectric constant. Lastly, they have to be available in the market with a low-cost. We have to pay attention in choosing the thickness of the substrate to compromise between enlarging antenna bandwidth and suppressing higher order surface waves. The thickness of the conductor on the substrate also takes a role [19]. It should be at least several times larger than the skin depth to avoid excessive loss. The skin depth in copper at 60 GHz is about 0.27 μm, so a copper foil thickness of several micrometers is sufficient. There is an upper limit, too. Increasing the conductor thickness makes the structure patterning process more inaccurate yielding poor structure profiles or larger minimum line spacing, which may degrade the performance.

Dielectric properties of the substrates are usually offered by the manufacturers only up to 10 GHz, which is far away from the mm-Wave range. Three commercially available and low-cost polytetrafluoroethylene (PTFE) composites based substrates have been characterized in this work, which are RO3003 and RT/duroid 5880 from Rogers Corporation [20], and CLTE-AT from Arlon MED [21]. A dielectric thickness of 127 μm with 17 μm copper foil (1/2 ounce) on both sides is chosen for all substrates. Their properties given by the data sheet from the manufacturers are summarized in Table 3.1.

The substrates are characterized by a simple planar transmission line method in wideband, and then the calculated dielectric constants are further verified by comparing the simulated and measured S11 of a patch resonator in a narrow band near 60 GHz. Unfortunately, the calculated loss tangent by the transmission line method is not accurate due to the conductor loss, imperfections in measurement, radiation loss from the structure, etc.

Table 3.1 Material Properties from Data Sheet [20] [21]

	Dielectric constant	Loss tangent	Test condition	Dielectric thickness	others
RO3003	3.00±0.04	0.0013	10GHz 23°C	127 μm	Ceramic-filled
RT/duroid 5880	2.20 2.20±0.02	0.0004 0.0009	1MHz 23°C 10GHz 23°C	127 μm	Fiberglass reinforced
CLTE-AT	3.0 3.0	0.0013 0.0013	1MHz 10GHz	127 μm	Fiberglass reinforced

3.2.1   Theory of Planar Transmission Line Approach for Substrate Characterization

The propagation constant γ of a microstrip transmission line, which includes the information of phase velocity and attenuation constant, can be extracted from the S-parameter measurements of two transmission lines with identical geometry but different lengths [22] as shown in Figure 3.1 (a). The microstrip transmission lines are measured by microwave probes with a tip configuration of ground-signal-ground (G-S-G). The influence of the measurement launching structures (probing pads and the pad-line discontinuity) can be de-embedded out by the following algorithm [22]. Line1 and line2 with a length of L_1 and L_2 ($L_1 < L_2$), respectively, are perfectly symmetric about the symmetric plane. The measured 2-port S-parameter matrices of the two lines can be mathematically converted into the transmission matrices, which are

$$M_1 = A \cdot T_1 \cdot B \tag{3.1a}$$

$$M_2 = A \cdot T_2 \cdot B \tag{3.1b}$$

where A and B are the transmission matrices of the measurement launching structures for port1 and port2, respectively, while T_1 and T_2 are the transmission matrices of the intrinsic lines with length L_1 and L_2.

We multiply the transmission matrix of line2 by the inversed transmission matrix of line1 as shown in Figure 3.1 (b)

$$M_{21}^h = M_2 \cdot [M_1]^{-1} = AT_2[T_1]^{-1}A^{-1} = AT_{21}A^{-1} \tag{3.2}$$

where M_{21}^h is the transmission matrix of the resulted hybrid structure, and $T_{21} = T_2[T_1]^{-1}$ is the transmission matrix of the line segment with length
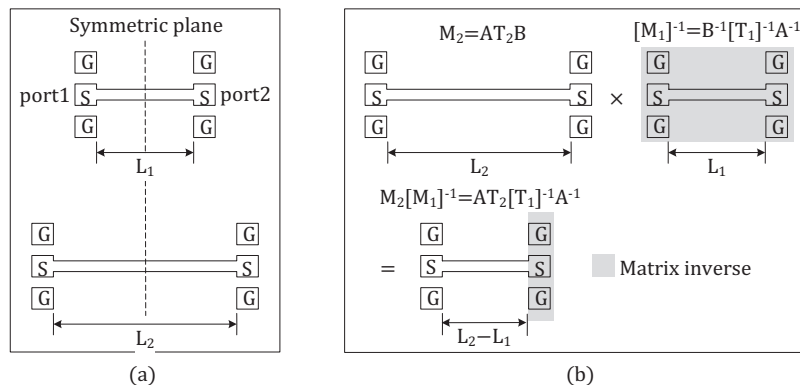
Figure 3.1: (a) Microstrip transmission lines with probing pads; (b) Multiplying the transmission matrix of line2 by the inversed transmission matrix of line1.

$L_2 - L_1$. Assuming the launching structure at port1 can be modeled solely by a lump admittance Y_A, we have

$$A = \begin{bmatrix} 1 & 0 \\ Y_A & 1 \end{bmatrix} \tag{3.3}$$

$$M_{21}^h = \begin{bmatrix} 1 & 0 \\ Y_A & 1 \end{bmatrix} \cdot T_{21} \cdot \begin{bmatrix} 1 & 0 \\ -Y_A & 1 \end{bmatrix} \tag{3.4}$$

The hybrid structure can be viewed as a parallel combination of lumped admittances Y_A at port1, $-Y_A$ at port2, and Y_{21} of the intrinsic line, so the Y matrix can be written as

$$Y_{21}^h = \begin{bmatrix} Y_A & 0 \\ 0 & -Y_A \end{bmatrix} + Y_{21} \tag{3.5}$$

where Y_{21}^h is the Y matrix representation of M_{21}^h, and Y_{21} is the Y matrix representation of T_{21}. The intrinsic line segment is perfectly symmetric, so swapping port1 and port2 will not change its matrices of S, Z, or Y, that is

$$Y_{21} = \begin{bmatrix} a_{11} & a_{12} \\ a_{21} & a_{22} \end{bmatrix} = \text{Swap}(Y_{21}) = \begin{bmatrix} a_{22} & a_{21} \\ a_{12} & a_{11} \end{bmatrix} \tag{3.6}$$

So we have

$$Y_{21}^h + \text{Swap}\left(Y_{21}^h\right) = Y_{21} + \begin{bmatrix} Y_A & 0 \\ 0 & -Y_A \end{bmatrix} + Y_{21} + \begin{bmatrix} -Y_A & 0 \\ 0 & Y_A \end{bmatrix} \tag{3.7a}$$

$$Y_{21} = \frac{Y_{21}^h + \text{Swap}(Y_{21}^h)}{2} \tag{3.7b}$$

The transmission matrix T_{21} of the lossy transmission line with length $L_2 - L_1$ can be explicitly expressed as [22]

$$T_{21} = \begin{bmatrix} \cosh\gamma(L_2 - L_1) & Z_c\sinh\gamma(L_2 - L_1) \\ Z_c^{-1}\sinh\gamma(L_2 - L_1) & \cosh\gamma(L_2 - L_1) \end{bmatrix} \tag{3.8}$$

where Z_c is the characteristic impedance of the line. Converting Y_{21} in (3.7b) to its transmission matrix T_{21}, and comparing it with (3.8), the complex propagation constant can be obtained

$$Y_{21} \rightarrow T_{21} = \begin{bmatrix} A & B \\ C & D \end{bmatrix} \tag{3.9a}$$

$$\gamma = \frac{\cosh^{-1}A}{L_2 - L_1} = \alpha + j\beta \tag{3.9b}$$

where α is the attenuation factor, and β is the phase factor. There are closed form formulas to describe a microstrip transmission line [23] [24]. Considering a low-loss microstrip line as a quasi-TEM line with a metal line width of W and a dielectric thickness d, we have

$$\alpha = \alpha_d + \alpha_o \tag{3.10a}$$

$$\beta = k_0\sqrt{\epsilon_e} \tag{3.10b}$$

with

wavenumber in free-space $\quad k_0 = \omega\sqrt{\epsilon_0\mu_0}$ (3.10c)

effective dielectric constant $\quad \epsilon_e = \frac{\epsilon_r+1}{2} + \frac{\epsilon_r-1}{2}[1 + 12\frac{d}{W}]^{-1/2}, \frac{W}{d} > 1$ (3.10d)

attenuation factor due to dielectric loss $\quad a_d = \frac{k_0\epsilon_r(\epsilon_e-1)\tan\delta}{2\sqrt{\epsilon_e}(\epsilon_r-1)}$ Np/m (3.10e)

losses other than the dielectric loss $\quad \alpha_o$ (3.10f)

From (3.9) and (3.10), we can calculate the effective dielectric constant ϵ_e, dielectric constant ϵ_r, and the dielectric loss tangent $\tan\delta$ as

$$\epsilon_e = \frac{\text{Imag}^2(\gamma)}{k_0^2} \tag{3.11a}$$

$$\epsilon_r = \frac{2\epsilon_e - (1 - [1+12d/W]^{-1/2})}{1 + [1+12d/W]^{-1/2}} \tag{3.11b}$$

$$\tan\delta = \frac{2\sqrt{\epsilon_e}(\epsilon_r-1)}{\epsilon_r k_0(\epsilon_e-1)}\alpha_d \tag{3.11c}$$

(3.11b) and (3.11c) are derived from the formulas of (3.10) based on quasi-static approximations, assuming a quasi-TEM line. The dielectrics under test are as thin as 127 μm with dielectric constants of about 2.2 and 3, so the lowest surface wave mode of TM_0 with zero cutoff frequency will not significantly coupled to the quasi-TEM mode of the microstrip line in the 60 GHz band, and there are no propagating higher order surface wave modes (see Figure 2.10). The dispersion effects of the microstrip lines are assumed to be not pronounced, and the calculation for dielectric constant is expected to be still valid in the 60 GHz band with acceptable accuracy. The calculated values will be verified by comparing the simulation (using calculated dielectric constant) and measurement of a narrow band resonant patch antenna. The calculated loss tangent will not be accurate, which is a drawback of this planar transmission line approach due to the fact that it is not possible to properly separate the dielectric loss from other losses, such as metallic ohmic and roughness losses, radiation loss, imperfect fabricated structure loss, etc.

3.2.2   Prototype Measurement and Verification

All structures are measured by microwave probes in G-S-G configuration with 250 μm pitch. Figure 3.2 shows the photos of the fabricated two microstrip lines (line width of W=0.3 mm) on RO3003 with lengths L_1=4.8 mm and L_2=5.5 mm, and their CPW to microstrip line via-less transitions. The same structures are also fabricated on other dielectrics under test. They are fabricated in-house by laser milling process, which can give good accuracy in metal

(a)   (b)
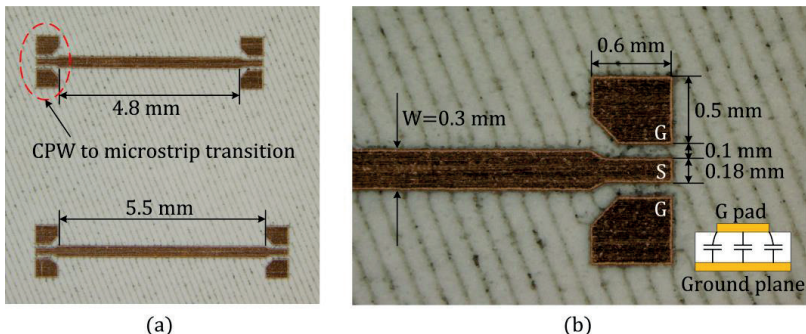
Figure 3.2: (a) Microstrip transmission lines on RO3003 with different lengths, and (b) coplanar waveguide (CPW) to microstrip via-less transition.
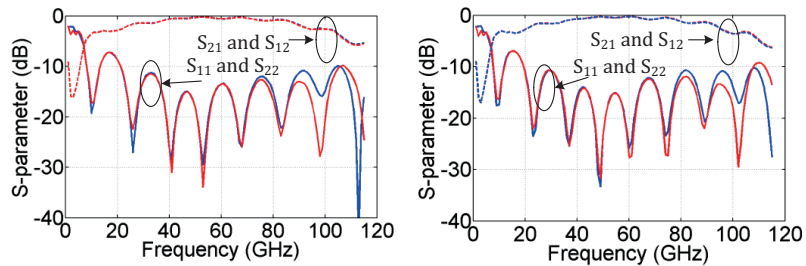

Figure 3.3: Measured S-parameter for microstrip lines on RO3003 with length L_1=4.8 mm (left), and L_2=5.5 mm (right).

structure patterning so that very symmetric structures can be achieved as shown in the photos.

The ground (G) pads have to be connected to the ground plane of the microstrip lines on the other surface of the dielectric. Conventionally, this is achieved by galvanic connections of through dielectric vias. The vias will introduce considerable parasitic effects, and it is difficult to make them with good accuracy by normal PCB process, e.g. their positions on the pads at each end of the microstrip line may be slightly different, thus violating the assumption of perfectly symmetric structure. Therefore, the ground pads are connected to the ground plane by capacitive coupling without using vias as shown in Figure 3.2 (b). Figure 3.3 shows the measured S-parameter of the two lines on RO3003 (referenced to 50 Ω, frequency span 1–115 GHz). S_{11} and S_{22} are identical to each other up to about 85 GHz, which implies a symmetric structure and a sufficient accuracy of probe contacting. At higher frequencies the influence of the small asymmetry of the probe contacting at each end of the line or tolerance of the structure fabrication becomes pronounced that the measured results start showing asymmetric. Below 40 GHz the insertion loss is high, because the capacitive coupling is not sufficient at these frequencies. We are in-

terested in the band of 40–80 GHz, where the lines and the transitions exhibit good performance.
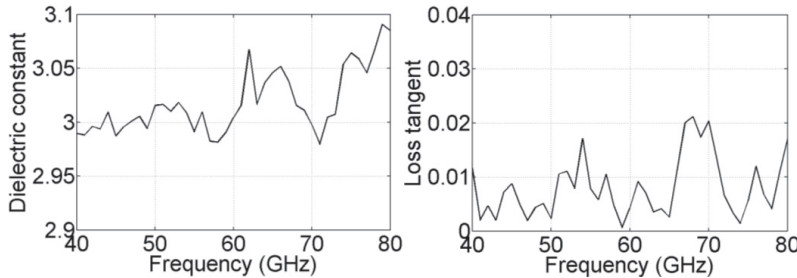

Figure 3.4: Calculated dielectric constant and loss tangent of RO3003.
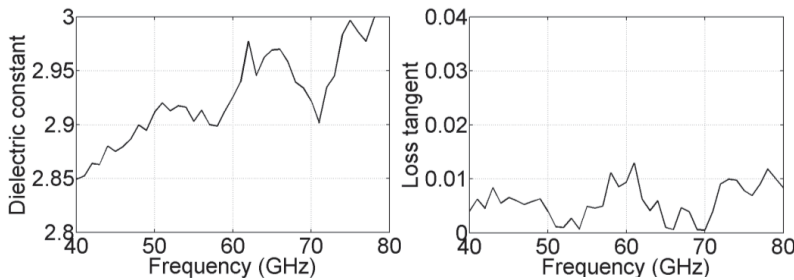
Figure 3.5: Calculated dielectric constant and loss tangent of CLTE-AT.
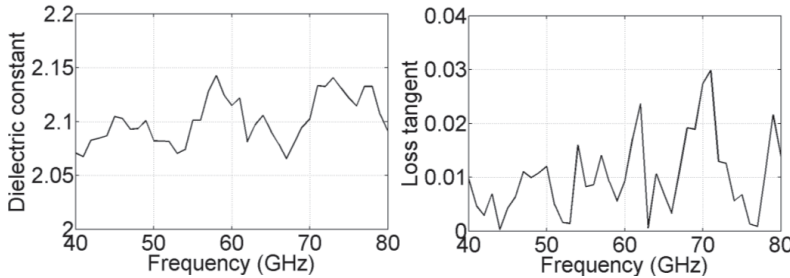
Figure 3.6: Calculated dielectric constant and loss tangent of RT/duroid 5880.

Table 3.2 Comparison of the ϵ_r from Calculation and Data Sheets

	Calculated (mean) ϵ_r	ϵ_r from data sheet	tanδ from data sheet
RO3003	3.02±0.05@50–70 GHz	3.0±0.04@10 GHz	0.0013@ 10 GHz
CLTE-AT	2.93±0.05@50–70 GHz	3.0@10 GHz	0.0013@ 10 GHz
RT/duroid 5880	2.10±0.04@50–70 GHz	2.2±0.02@10 GHz	0.0009@ 10 GHz

Figure 3.4, Figure 3.5, and Figure 3.6 show the calculated dielectric constant and loss tangent of RO3003, CLTE-AT, and RT/duroid 5880, respectively. The calculated loss tangent is considerably higher than its actual value, because it is assumed in the calculation that all losses are from the dielectrics. In fact, for most microstrip substrates conductor loss is more significant than dielectric loss except for some semiconductor substrates [23]. The calculated dielectric constants have fluctuations within about ±0.05 in the 60 GHz band, and the mean values (averaged in the band of 50–70 GHz) are compared with the values from the data sheet in Table 3.2. The calculated value of RO3003 is 3.02 at 60 GHz which is almost identical to that in the data sheet. The calculated values at 60 GHz of CLTE-AT and RT/duroid 5880 are slightly smaller than the given ones in the data sheets, which were measured at 10 GHz by the manufacturers of the dielectrics.

Patch resonators are fabricated together with the transmission lines on the same dielectrics using the same measurement launching structure, as shown in Figure 3.7, to verify the calculated dielectric constants. The S_{11} of the patch resonator is simulated by using the dielectric constant from the calculation, and then it is compared with the measured S_{11} to verify the calculation around the resonant frequency. To illustrate the necessity of the dielectric characterization the dielectric constant value from the data sheet is also input to the simulation, and the simulated S_{11} is compared with the measured one, too. The loss tangent values used in the simulations are from the data sheet. Figure 3.8 shows the comparison results. It can be seen that the simulations by using the calculated dielectric constants for RO3003 and RT/duroid 5880 have excellent agreement with the measurements. There is small discrepancy for CLTE-AT at 60 GHz, but after applying a tiny modification to Er in simulation (from 2.93 to 2.92) the agreement is excellent, too. In contrast when the dielectric constants from the data sheets are used in the simulations, the resonant frequency is shifted from the measurement except RO3003 whose value is almost identical to the calculated one. RO3003 will be used for the 60 GHz antenna designs in the following sections due to its stable dielectric properties and low-cost.


(a)   (b)
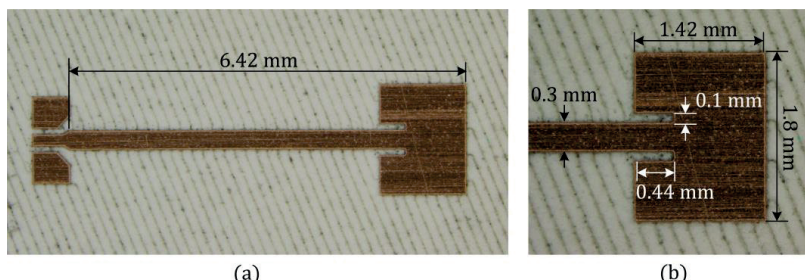
Figure 3.7: (a) Patch resonator with CPW to microstrip transition; (b) Enlarged view of the patch.
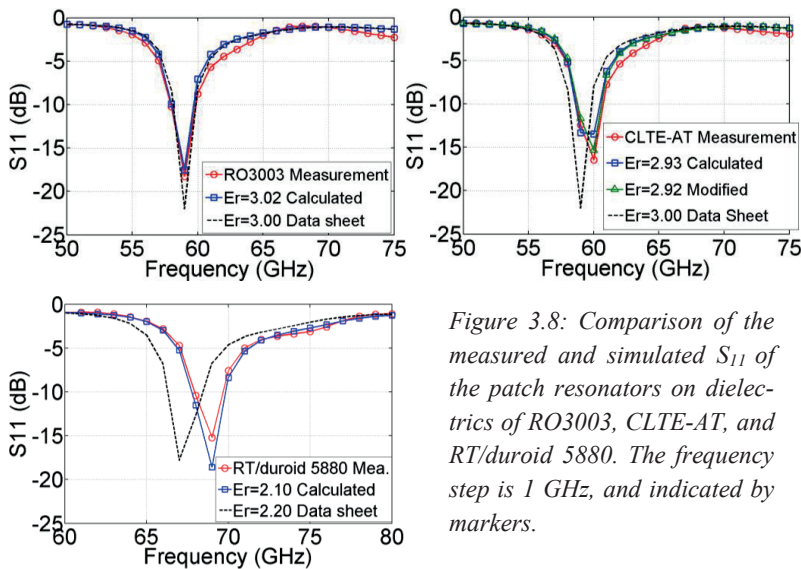
Figure 3.8: Comparison of the measured and simulated S_{11} of the patch resonators on dielectrics of RO3003, CLTE-AT, and RT/duroid 5880. The frequency step is 1 GHz, and indicated by markers.

3.3   Millimeter-Wave Interconnects

Wire-bonding and flip-chip are the state-of-the-art mm-Wave interconnect technologies, which are indispensable for the integrated PCB antenna and many other antenna in-package designs. In this section they are tested in the lab in the frequency band of 1–115 GHz, and a novel bond-wire compensation structure is proposed to improve the impedance matching and reduce the loss.

3.3.1   Wire-Bonding and Bond-Wire Compensation

The bond-wire under test is made by a wedge bonder manually in the lab. The wire is made of aluminum with a diameter of 25.4 µm (1 mil) as shown in Figure 3.9a. In order to investigate how significant parasitic effects and loss a bond-wire with different length can introduce, some test structures b–e in Figure 3.9 have been fabricated on the RF substrate of RO3003, and measured. Structure b is a 4 mm-long through microstrip line with the same via-less measurement launching structure as discussed in last section, which has good impedance matching to 50 Ω in 60 GHz band. Breaking structure b in the middle, and leaving a gap with different dimensions of 0.4, 0.7, and 0.9 mm yields structures c, d, and e. The two parts of the microstrip lines are then interconnected by bond-wires with different lengths of approximately 0.5, 0.8, and 1 mm, respectively. Figure 3.10 shows the measured S_{11} and S_{21} of the structures b–e. S22 and S12 are not plotted for better visualization, and they will not give additional information due to the symmetric structures. It can be observed that
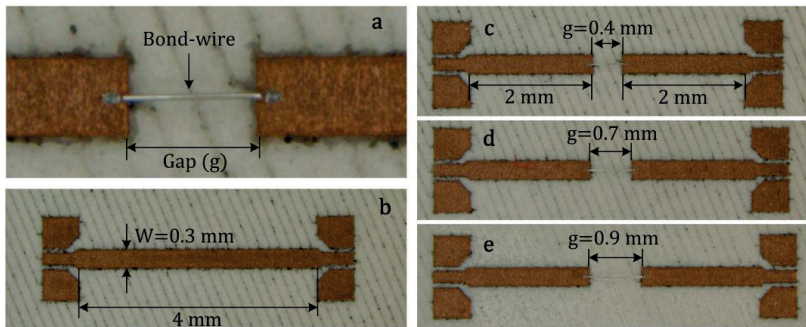
Figure 3.9: Bond-wire test structures.
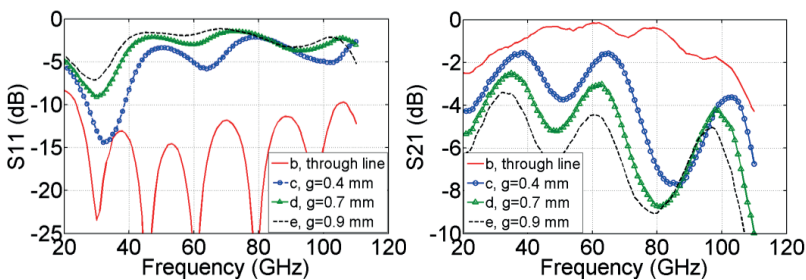
Figure 3.10: Measured S-parameters of bond-wire test structures b–e.

the through line has good impedance matching and low insertion loss in the band of 40-80 GHz, while those of the structures with bond-wires are bad. It can also be clearly seen that longer bond-wire gives worse matching (higher inductance), and higher insertion loss. 1mm-long bond-wire introduces about 1 nH inductance is known as a rule of thumb. A bond-wire with very short length is difficult to make, and the repeatability is a serious issue. A wire length of 0.5 mm is assumed in the compensation design, which has been experimentally proven achievable with good repeatability by manual implementation in the lab.

The targeted bond-wire compensation method should offer good performance over enough bandwidth, good repeatability, ease of fabrication, and low-cost. In [25] a five-stage low-pass filter type bond-wire interconnect has been proposed, which achieved a return loss of greater than -12 dB and an insertion loss from 0 to 0.3 dB from dc to 80 GHz using two 432-µm-long 1-mil-diameter ball bonds. However, it requires compensation structures on both sides of the bond-wires which indicates the necessity of larger chip area, and the co-design of the chip and PCB antenna or in-package antenna. In [26] a series capacitor is used to tune out the inductance of the bond-wire, thus compensating the bond-wire at the resonant frequency. Although only an additional series capacitor realized by a small printed transmission line is required on the package side by

this scheme, it calls for multilayer board/package design to realize the series capacitor that complicates the PCB antenna fabrication.

Figure 3.11 shows the concept and a prototype of the proposed novel double-bond-wire compensation scheme. The compensation structure is symmetric, which comprises of two identical series bond-wires and a shunt capacitor in the middle. The bond-wires are assumed to be about 0.5 mm long and treated as inductors with value of L_{bw}. The length of the bond-wires is bounded by the gaps (0.4 mm) so that we can expect less tolerance in length of the bond-wires even by manual implementation. Its repeatability will be verified by the measurements shown later. The shunt capacitor is made by a small piece of microstrip transmission line in size of $w_1 \times w_2$, and the size can determine the capacitance value. The Smith-chart in Figure 3.11 (c) demonstrates the principle of this compensation method. One series bond-wire with inductance L_{bw} will move the impedance point from the matched center to point A for frequency f_0 along the constant resistance circle. Then, the shunt capacitor with an appropriate capacitance value C transforms the admittance from point A to B along the constant conductance circle. Last, the other series bond-wire with the same inductance value of L_{bw} can make the impedance point back to matched point. We can also achieve matching at another frequency f' for the same bond-wires, but with a different capacitance C', which can be obtained by tuning the size of the capacitor (w_1 and w_2). From the plot it is easy to see that when f'<f_0 it requires C'>C, hence a larger capacitor size and vice versa.

The same measurement launching structures as that shown in Figure 3.9 are used in the bond-wire compensation prototypes characterization. From Figure 3.10 we can see that the launching structures have good matching to 50 Ω, so they represent the 50 Ω ports in the measurement. Figure 3.12 shows the measured S-parameters of the structures without (Figure 3.9c) and with bond-wire compensation (Figure 3.11b) for the same bond-wire length of about 0.5 mm.
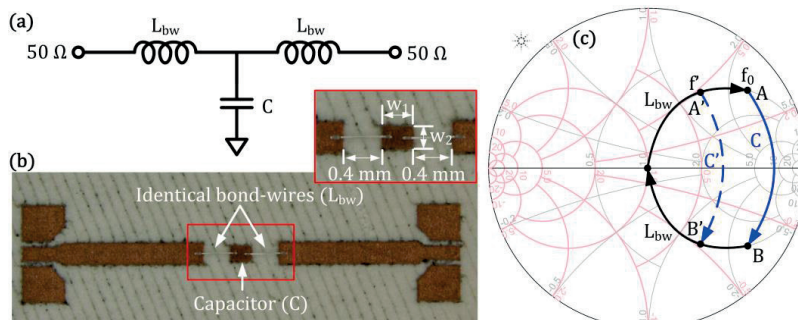

Figure 3.11: Presentation of double-bond-wire compensation scheme: (a) Equivalent circuit model of the compensation structure; (b) Fabricated prototype of the compensation structure; (c) Theory presented by Smith-chart.
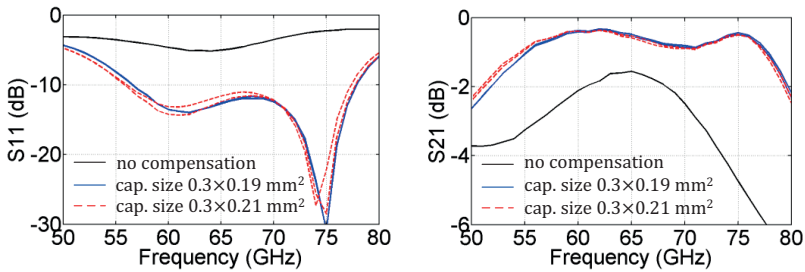
Figure 3.12: Measured S-parameters of the structures with and without bond-wire compensation.
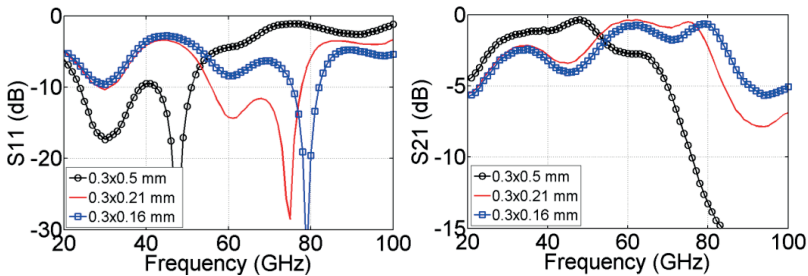
Figure 3.13: Measured S-parameters of the compensated structures with different capacitor sizes (capacitances).

The compensation structures with two slightly different capacitor sizes, 0.3×0.19 mm^2 and 0.3×0.21 mm^2, were measured, and the measured results are plotted for two samples for each size. The measured results are consistent, which indicates this method can give good repeatability and can tolerate, to some extent, imperfections of the PCB metal structure patterning. The reflection coefficient of the structures with compensation is lower than -10 dB from 57 to 77 GHz, and the insertion loss is lower than -1 dB from 55 to 77 GHz which are significantly better than that without compensation. Importantly, the large bandwidth can also help to tolerate possible variations in the fabrication and applications. Subtracting the loss from the launching structures (Figure 3.10), the L-C-L structure itself only gives a loss of about 0.2–0.3 dB at 62 GHz.

As discussed before by tuning the size (capacitance) of the capacitors the pass-band can be selected. Figure 3.13 shows the measured S-parameters of the compensated structures with different capacitor sizes but constant bond-wire length of 0.5 mm. The pass-bands are 48, 60, and 80 GHz, which correspond to capacitor sizes of 0.3×0.5 mm^2, 0.3×0.21 mm^2, and 0.3×0.16 mm^2, respectively. It can be found that larger capacitor shifts the pass-band to lower frequency and vice versa, which is also clearly seen from the Smith-chart in Fig-

ure 3.11c. This verifies that the compensation structure can be scaled to use in many frequency bands. This method was published in [27].

3.3.2   Flip-Chip and Stud Bumps

The interconnect bumps of flip-chip technology are much shorter but thicker than the bond-wires, so they have less parasitic effects. The general advantages and constrains of this technique has been discussed in section 2.5.1. The loss of the stud bumps is characterized experimentally in a wide band of 1–115 GHz in this section. The fabricated prototype is shown in Figure 3.14. The chip is represented by a small board, whose top view and bottom view are shown in Figure 3.14a and Figure 3.14d, respectively. A floating grounded coplanar waveguide (GCPW) transmission line with a length of 5.4 mm is fabricated on a thin film dielectric of CLTE-AT with a thickness of 127 μm, which has been characterized in section 3.2. The thin film is laminated on FR4 epoxy with a thickness of 0.51 mm to make the "chip" mechanically robust. The parameters of the GCPW line are illustrated in Figure 3.14b with the enlarged view of the gold stud bumps. The minimum slot width between the signal line and ground lines is limited to 0.1 mm by the PCB technology so that the characteristic impedance of the line is a little higher than 50 Ω. The stud bumps are made by gold ball wire bonding. The bonder first places a gold bump on the metal, and then breaks the wire above the bump, thus leaving a small wire tail. The maximum diameter of the bumps is about 70–80 μm and the height is around 60 μm excluding the wire tail. During the flip-chip process the stud bumps will undergo heating and pressing that the height decreases to about 30–40 μm. On the mother board structure c contains two 5 mm-long GCPW lines that have the same parameters as the line on the "chip", and a gap of 5 mm is left between them for flip-chip. The line on the "chip" is 5.4 mm-long, so it is overlapped with the on-board lines of about 0.2 mm at each end. The flip-chip is done in a thermo-compression process by FINEPLACER® bonding system from finetech [28]. The bonding system enables transparent view to align the chip with the mother board under microscope as shown in Figure 3.14e. A thermally conductive but electrically nonconductive epoxy EPO-TEK® 930-4 from EPOXY TECHNOLOGY [29] is used as underfill material. The underfill has a dielectric constant of 3.73 and a loss tangent of 0.004 at 1 kHz (23°C) from the data sheet. The test samples are made with and without underfill covering the bumps to estimate the influence of the underfill over the interconnects. The area of the on-chip GCPW line is not underfilled.

Microwave probes with 250 μm pitch are used for the measurements. Figure 3.15 shows the measured S-parameters of the GCPW-Chip-GCPW flip-chip structure with and without underfill covering the stud bumps, and the 15 mm-long GCPW through line (Figure 3.14f). The S_{11} of the through line is better
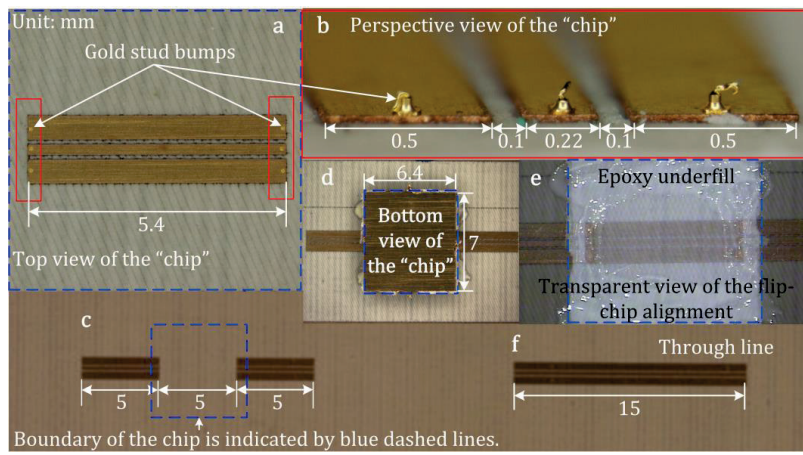
*Figure 3.14: Fabricated prototype for stud bumps characterization. (Unit: mm)*
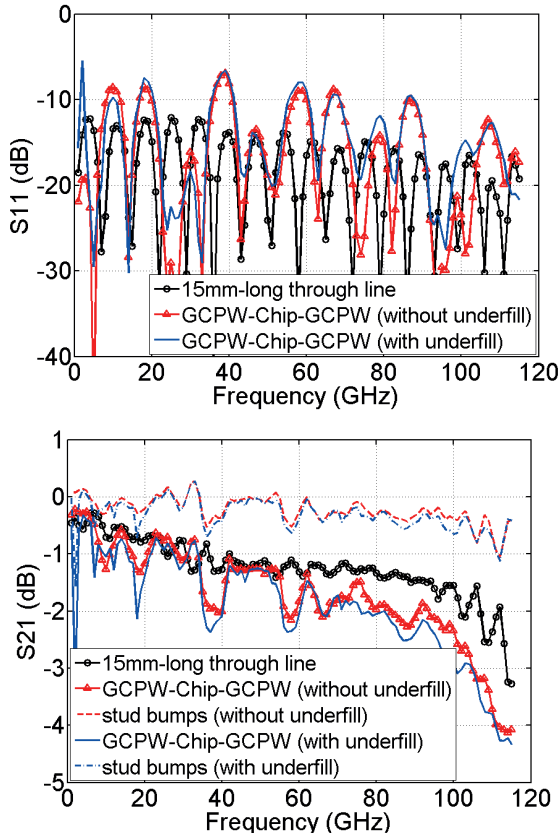
Figure 3.15: Measured S-parameters of the test structures, and the estimated loss from the stud bumps.

than -12 dB over the measured bandwidth. The S_{11} of the flip-chip structure with and without underfill around bumps is similar to each other, and both better than -7 dB without employing any compensation structures. The loss of one set of coplanar stud bumps is estimated by subtracting the insertion loss of the through line from the insertion loss of the flip-chip structure, and then dividing that by 2. The stud bumps have "positive" insertion loss S_{21} at some frequencies. This is because the flip-chip structure has better S_{11} at those frequencies than the through line, and then the S_{21} is higher than the latter, resulting in positive values after subtraction. By comparing the S_{21} of stud bumps with and without underfill we can see that the underfill introduce a little additional loss to the bumps. The stud bumps give a maximum insertion loss of 0.7 dB with underfill and 0.5 dB without underfill up to 100 GHz. The loss is higher around some frequencies like 18 GHz, 38 GHz, 58 GHz, and so on due to the worse S_{11} of the flip-chip structures. We can expect that the insertion loss can be lower if some impedance compensation structure is applied in certain bands.

3.4   60 GHz Antenna Designs and Demonstrators

The free-space loss at 60 GHz is as high as 68 dB per meter, which indicates a tight link budget for the communication systems. It requires a moderate gain of single antenna solution for short range (<10 m) indoor applications or even a phased array to enlarge the distance and improve the quality of service (QoS). Differential circuits have many attractive advantages such as compression of even-order harmonic distortion, interference rejection, higher dynamic range, better immunity to possible imperfections of chip-board ground connection, etc. All antenna designs in this section have differential feedings that enable direct connection to the circuits without using a balun, thus reducing the loss and noise. The RF input/output impedance on the pads of the integrated circuit (IC) are designed to be 50 Ω, so a full port odd-mode (differential) impedance of the antenna has to be optimized to 100 Ω. The bond-wire interconnects are considered as part of the antenna designs, and the compensation structure is optimized for each design. The system demonstrators are also shown.

3.4.1   Differential Bunny-Ear Antenna

The principle of a bunny-ear antenna has been discussed in 2.2.3. The antenna design is shown in Figure 3.16. It is fabricated on a characterized thin film dielectric of RO3003 (ϵ_r=3.02, tanδ=0.0013) with a thickness of 127 μm. The radiation slot line and microstrip-to-antenna transition line are both described by exponential functions as (in mm)

Radiation slot line: $x = \pm(e^{0.00513 \cdot y^{1.67}} - 0.94), \quad y \in [0, 30]$ (3.12)
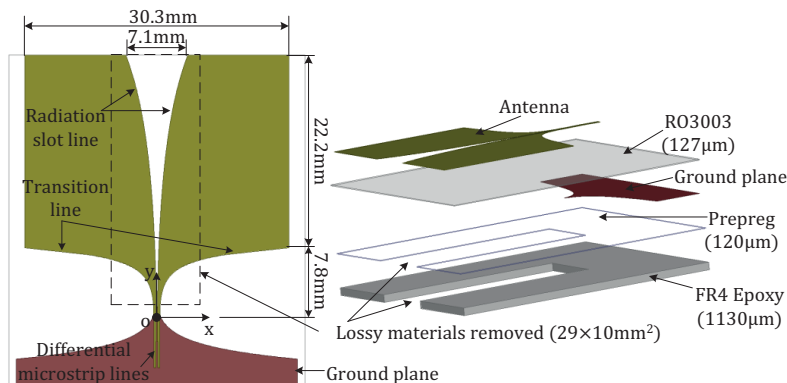
Figure 3.16: Differential bunny-ear antenna design.

Transition line: $\quad x = \pm\left(e^{0.0221 \cdot y^{2.35}} - 0.64\right), \quad y \in [0, 7.8]$ $\qquad$ (3.13)

The functions are optimized by 3-D EM simulations, which lead to a maximum slot opening of 7.1 mm (1.42 wavelength in free-space at 60 GHz), antenna width of 30.3 mm, and antenna length of 30 mm. The antenna is fed by differential microstrip lines, and matched to 100 Ω port impedance. The ground plane of the microstrip lines is also tapered to achieve a smoother microstrip-to-antenna transition.

The thin thickness and low dielectric constant of RO3003 guarantee no higher-order mode surface waves. However, it is too soft to be used alone that an FR4 Epoxy (ϵ_r=4.4, tanδ=0.02) carrier with a thickness of 1.13 mm was laminated under it by using two layers of 60 µm-thick prepreg 1080 (ϵ_r=4.2, tanδ=0.01 at 5 GHz) to make the antenna and other circuits mechanically robust. To maintain the high efficiency the lossy and thick FR4 under the antenna has to be removed, otherwise, the simulated radiation efficiency is only 25%. It is known that the field is most intense along the radiation slot. Therefore, only a small piece of FR4 (29×10 mm^2) around the radiation slot is removed without sacrificing much of the mechanical stability. Figure 3.17 shows the simulated S_{11}, gain, and radiation efficiency for the antenna on RO3003 only, and the antenna with cut FR4. The S_{11} is similar for the two cases, which is below -10 dB in a wide band of 50–70 GHz. The gain is also similar and flat over frequency, which is around 12–13.5 dBi in the 60 GHz band. However, the radiation efficiency for the antenna with cut FR4 is degraded to about 83%, which is 11% lower than that without FR4. Figure 3.18 shows the simulated radiation patterns in E- and H-plane for the antenna with cut FR4. The radiation patterns are almost identical to each other with a 3-dB beamwidth of 28° in both principle planes for the frequencies of 57, 62, and 66 GHz, which are the lowest, center, and highest frequencies in the 60 GHz band.
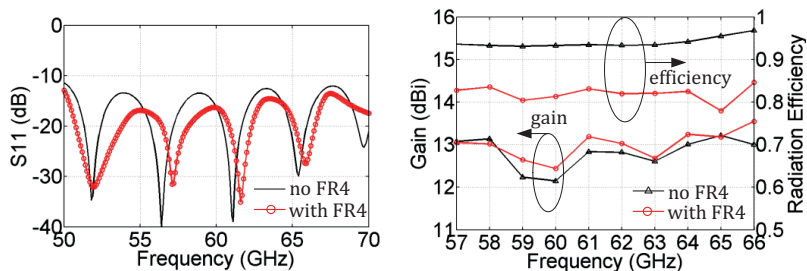
Figure 3.17: Simulated S11, gain, and radiation efficiency for the antenna on RO3003 only, and the antenna with cut FR4.
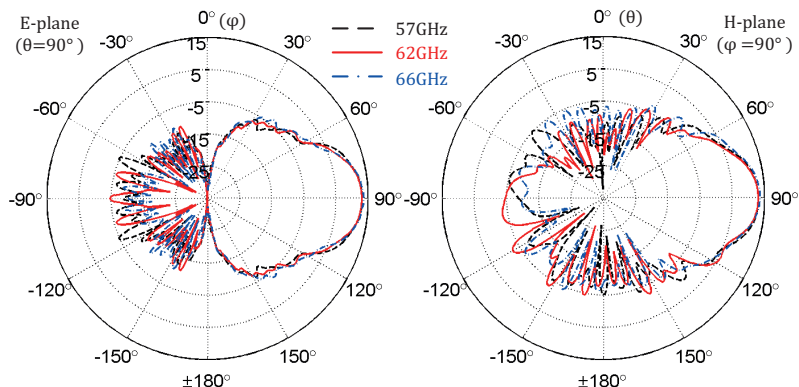

Figure 3.18: Simulated radiation patterns (in dBi) of the antenna with cut FR4 for frequencies of 57, 62, and 66 GHz.

A prototype has been fabricated as shown in Figure 3.19 to evaluate the performance of the antenna, and verify the simulation. The bond-wire compensation structure is considered as part of the antenna, which have a differential reference input impedance of 100 Ω, and all structures are included in the simulation. The antenna is fabricated by standard PCB technology of wet etching. The profile of the planar structures slightly deviates from that in the simulation due to the nature of the wet etching process, obtaining rounded instead of squared corners and line edges (see Figure 3.19c). The antenna is measured by a microwave probe based measurement setup (single-ended), which has been described in section 2.4. A balun and a CPW to microstrip transition have to be employed in the measurement as shown in Figure 3.19c. The balun comprises of 2 sections of half-wavelength transmission lines which provide 180° phase shift between the output ports P2 and P3 [30]. More sections of the balun can give even wider bandwidth but higher loss. Figure 3.20 shows the simulated performance of the 2-section balun (without the CPW to microstrip transition). Both the phase balance and the magnitude balance of the output ports (S_{21} and S_{31}) as well as the input reflection coefficient (S_{11}) are very good over the interested frequency band of 57–66 GHz.
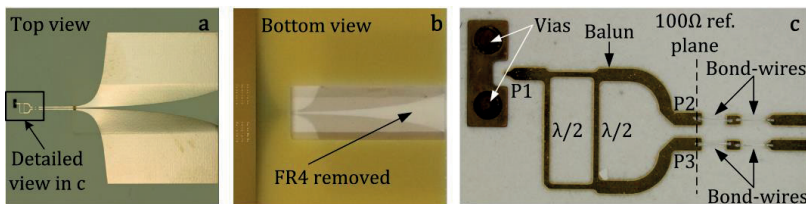
Figure 3.19: Fabricated prototype of the bunny-ear antenna.
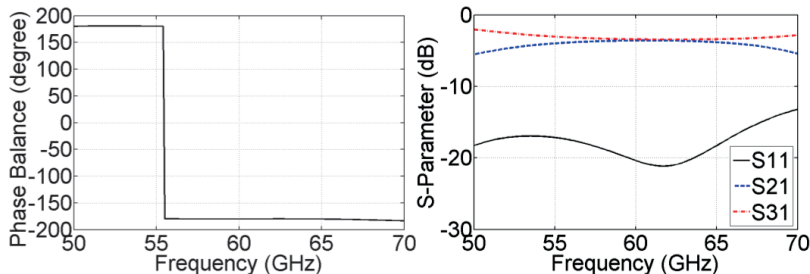
Figure 3.20: Simulated results of the Balun (without CPW to microstrip transition).

Figure 3.21 shows the simulated S11 of the antenna with and without measurement structures, i.e. the balun and the CPW to microstrip transition. The simulated S11 for the antenna without measurement structures, which is the case in practical applications, is better than -10 dB including the bond-wire and its compensation over the entire 60 GHz band. However, the S11 is significantly deteriorated above 60 GHz by the introduction of the balun, and especially the CPW to microstrip transition with vias for the measurement. The measured S11 of two samples have been plotted in the same figure, and they are consistent. This again verifies the good repeatability of the bond-wire compensation scheme. The simulation and measurement generally have good agreement. The small deviations can be from many factors, such as fabrication tolerances, non-characterized (at 60 GHz) dielectrics of FR4 and prepreg, variations of the bond-wires from the simulation, etc. The measured gain is in the range of 10–12.5 dBi from 54 GHz to 66 GHz. It can be observed that the gain is declining after 60 GHz, to large extent, due to the worse S11 caused by the measurement structures. In addition, the loss from the measurement structures is not calibrated out, so a 1–2 dB higher gain is expected in practical applications.

Figure 3.22 shows the simulated and measured normalized radiation patterns in the two principle planes at 62 GHz. There are more sidelobes in the upper hemisphere in H-plane due to the spurious radiation from the balun. The simulation and measurement have excellent agreement, which indicates that the simulated patterns for the antenna in practical applications shown in Figure 3.18 can be trusted.
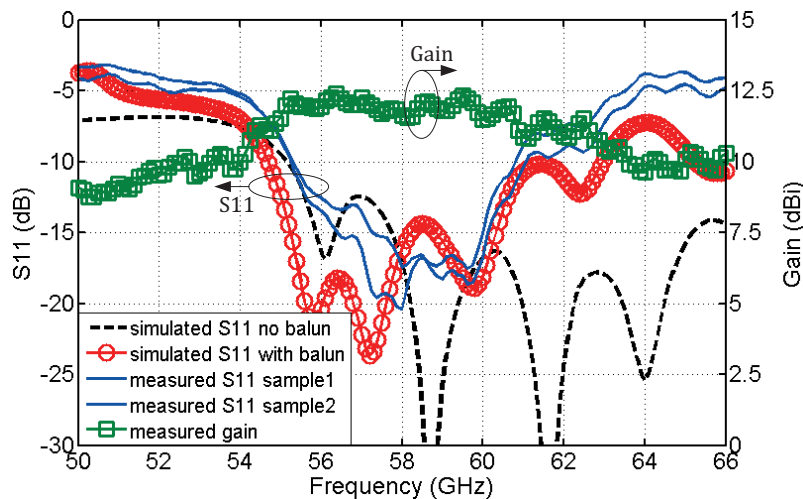
Figure 3.21: Simulated and measured results of the antenna prototype.
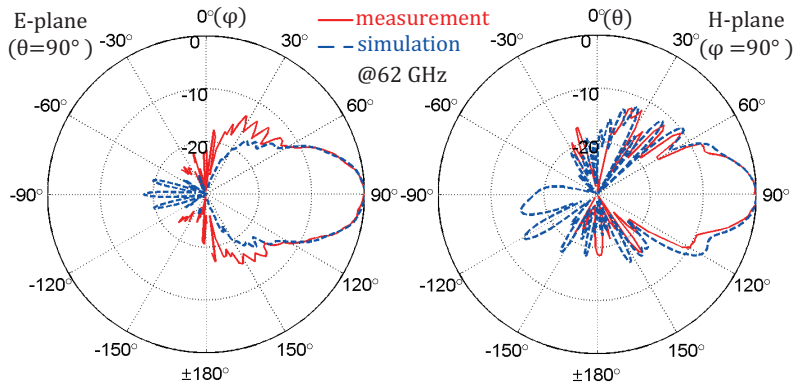

Figure 3.22: Simulated and measured normalized radiation patterns (in dB) at 62 GHz.

3.4.2   60 GHz Demonstrator with Bunny-Ear Antenna

The demonstrator board is shown in Figure 3.23. The chip is fixed in a metalized cavity by glue so that the surface of the chip is at the same level as the surface of the board. A metal ring is extended out from the cavity, and it is connected to the ground plane of the circuit board (bottom metal layer of RO3003) as well as the top metal plane of the RF4 carrier by the metal wall. The ground pads on the chip are wire-bonded to the metal ring, which is the shortest way between the on-chip and on-board ground plane to minimize the parasitics. There are many on-chip ground pads, which are wire-bonded to the ground ring to further improve the connection between the on-chip and on-board
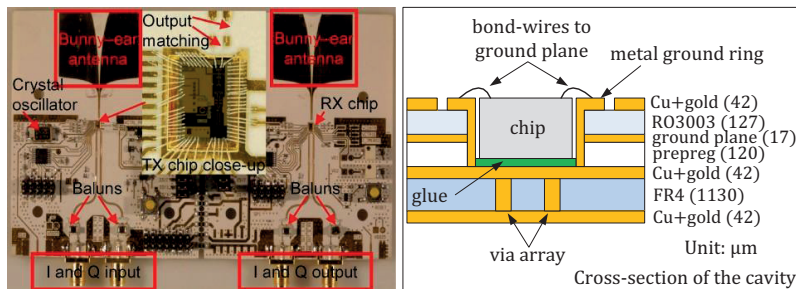
Figure 3.23: 60 GHz transceiver demonstrator.

Constellation diagram for 16QAM

Demonstrator measurement
setup in indoor environment
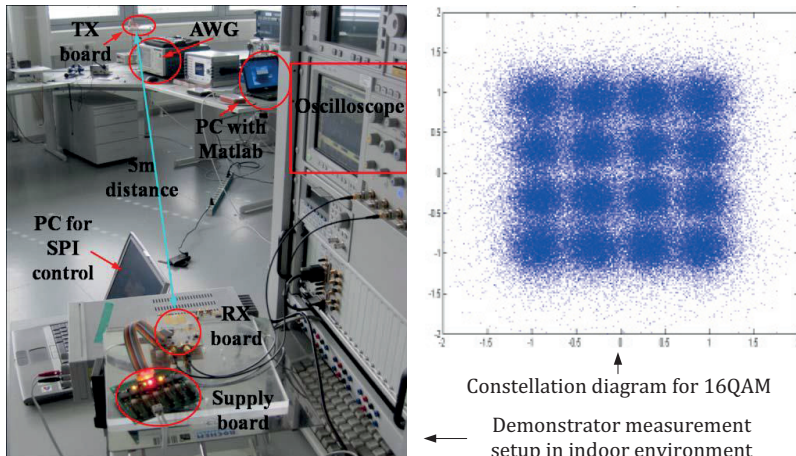
Figure 3.24: Demonstrator indoor measurement setup, and the measured constellation diagram for 16QAM, ¾ coding, OFDM signal with 3.6 Gbit/s data rate over 15 m distance.

ground. In addition, the differential circuit is inherently immune to imperfections of ground connection. The two metal layers of the FR4 carrier are connected by via arrays for better heat dissipation.

The transmitter front-end chip consists of a 12 GHz I/Q mixer, an intermediate frequency (IF) amplifier, a phase-locked loop (PLL), a 60 GHz mixer, an image-rejection filter and a PA. The measured 1-dB compression point at the output is 12.6 dBm and the saturated power is 16.2 dBm [31]. The receiver front-end chip consists of a low-noise amplifier (LNA), a 60 GHz mixer, a PLL and an IF demodulator. The measured noise figure of the LNA is 6.5 dB at 60 GHz, and the overall conversion gain of the receiver is 81 dB with tuning range larger than 30 dB [32]. The demonstrator was measured in an indoor environment as shown in Figure 3.24 for data transmission with an orthogonal frequency division multiplexing (OFDM) signal. The OFDM physical layer (PHY) parameters are similar to the IEEE 802. 15. 3c standard. I and Q input signals have

850 MHz bandwidth each. The transmitter (TX) and receiver (RX) were measured in a loop: Matlab–Tektronix arbitrary waveform generator (AWG)–TX–RX–Agilent oscilloscope–Matlab. Matlab gives OFDM frames information to the AWG, which generates the frames and feeds them to the TX. The received signal is fed from the RX to the oscilloscope, and the sampled signal is analyzed by Matlab. Data transmission of 3.6 Gbit/s (4.8 Gbit/s raw – i.e. without coding) was demonstrated over 15 meters with zero frame error rate (FER). The FER was measured for 2000 frames. The OFDM signal used 16QAM modulation scheme with ¾ coding. The measured constellation diagram is also shown in Figure 3.24. The presented demonstrator was the best reported analog front-end in silicon technology without beamforming regarding both the data rate and transmission distance at the time of its publication [33]. The high gain of the differential bunny-ear antenna, and the low-loss antenna-to-chip interconnects design have large contribution to the link budget, obtaining superior performance of the demonstrator.

3.4.3   Differential Patch Array Antenna

The bunny-ear antenna features an end-fire radiation direction and a relatively large size. For some applications a broad-side radiation direction or a smaller antenna size with an acceptable lower gain may be preferred. A 4-element patch array antenna as shown in Figure 3.25 has been developed as another choice for the demonstrator. It is highly desirable that only the antenna part of the demonstrator board is replaced by the new antenna design, and other circuit design can be largely maintained by using the same substrate, i.e. RO3003 with a thickness of 127 μm. However, it is too thin for patch antennas to obtain acceptable bandwidth for 60 GHz applications. In order to achieve a thicker substrate the copper on bottom side of RO3003 is removed under the antenna. In this way the 120 μm prepreg 1080 acts as an additional substrate for the antenna, and the top metal of the FR4 serves as the ground plane for the antenna. Actually, the ground plane of other on-board circuits (on bottom side of RO3003), the ground plane of this antenna (top metal of FR4), and the on-chip ground are well connected by the metalized cavity and many bond-wires as shown in Figure 3.23. The patch array antenna consists of 4 patches and 4 pairs of parasitic dipoles to increase the directivity, broaden the bandwidth [34], and suppress the surface wave. A thick substrate is risky for the patch antenna due to the possible surface wave effects, which can reduce the radiation efficiency and distort the radiation patterns. The total thickness of the hybrid substrate is 247 μm, and the cutoff frequency for TE_1 mode is about 170 GHz from equation (2.48) (using the higher dielectric constant 4.2 of prepreg 1080 with a substrate thickness of 247 μm). Therefore, there are no higher-order propagating surface wave modes for 60 GHz applications except for TM_0 with zero cutoff
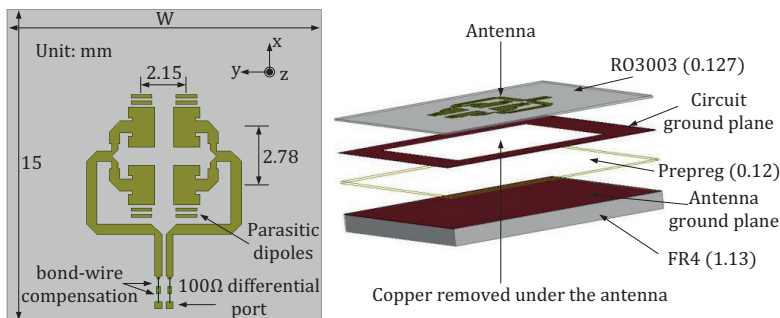
Figure 3.25: Differential patch array antenna. unit: mm.
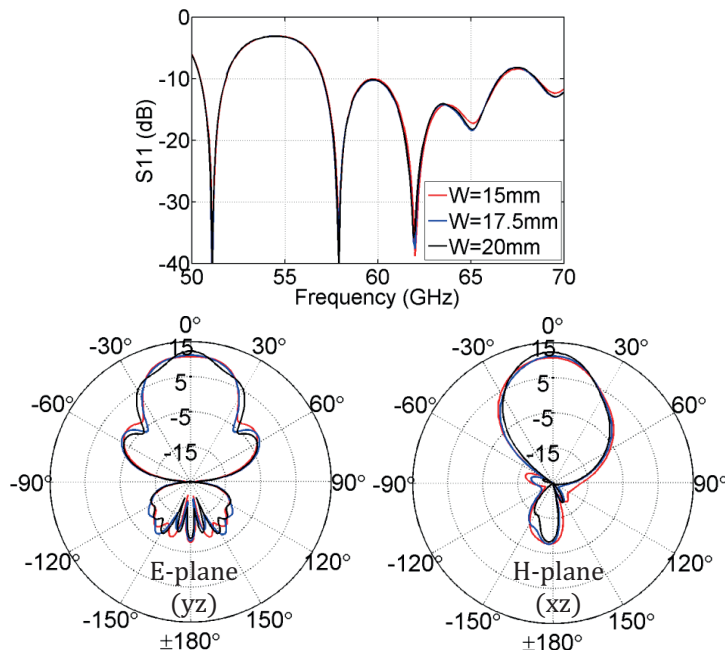
Figure 3.26: Simulated S_{11} and radiation patterns (in dBi) at 62 GHz of the antenna with different substrate width (W).

frequency. In addition, the radiation efficiency of broadside antennas can be greatly improved by an antenna array with cophasal excitation of the array elements placed half-wavelength apart [35] [36]. This can be partially explained in terms of the phasings of the surface wave fields. Surface waves, launched end-fire from each element, are significantly out of phase and tend to cancel. When the surface wave effect is pronounced, the antenna performance will strongly depend on the finite substrate size due to the reflection and diffraction of surface waves at the truncated substrate edges. Figure 3.26 shows the simulated S11 (including bond-wire compensation structure) and radiation patterns

in the principle planes at 62 GHz of the antenna with different substrate width (W). It can be observed that the S11 is consistent and better than -10 dB in the frequency band of 57–66.5 GHz. There is slight difference in radiation patterns due to the diffraction of the radiated fields at the edges of the finite ground plane with different sizes. The gain is more than 10.5 dBi at 62 GHz with an efficiency of 86%. The conclusion is that the surface wave effect does not have much influence over the antenna performance, although a relatively large bandwidth for the patch array antenna of about 15% is achieved.

The fabricated antenna prototype and the demonstrator module with the antenna are shown in Figure 3.27. Again, the differential antenna has to be measured by using a balun and a CPW to microstrip transition. The transition is via-less and grounded by electromagnetic coupling, which is similar to that introduced in 3.2.2. The balun is of the same type of the one used in the bunny-ear antenna prototype measurement, but it contains 4 stages to guarantee the bandwidth. In order to calibrate out the losses caused by the balun and the transition, a back-to-back calibration structure has been fabricated and measured, too. The measured results of the back-to-back calibration structure are plotted in Figure 3.28. The S_{11} is well below -14 dB from 57 GHz to 70 GHz, which implies that the return loss contribute little to the insertion loss S_{21}. The actual antenna gain is estimated by subtracting a half of the insertion loss of the back-to-back calibration structure from the directly measured antenna gain.
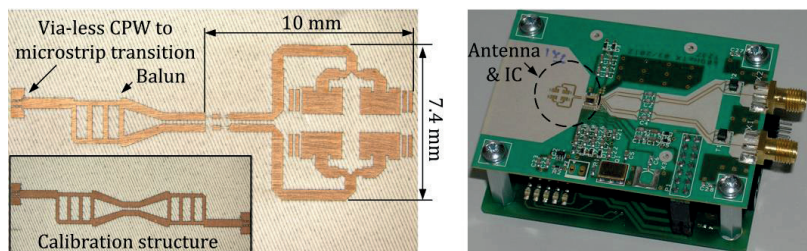

Figure 3.27: (Left) Antenna prototype and back-to-back calibration structure; (Right) Demonstrator module with antenna.
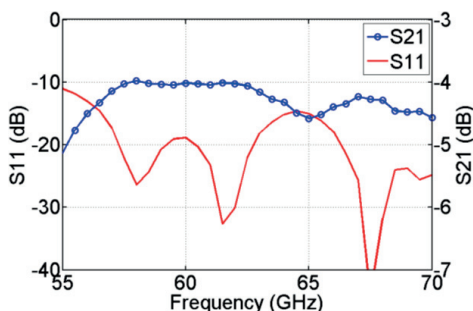
Figure 3.28: Measured results of the back-to-back balun and CPW to microstrip transition.

Figure 3.29 shows the measured and simulated S11 of the antenna prototype as well as the simulated and measured antenna gain. The measured S11 is shifted to higher frequency by about 1 GHz (1.7% refers to 60 GHz) compared to the simulation. This is probably due to the use of prepreg 1080 as an additional substrate. Its dielectric constant (E_r=4.2) was only characterized at 5 GHz, and its thickness can be reduced during the laminating process with high temperature and pressure. When an effective dielectric constant of 3.6 for the prepreg is used in the re-simulation, better agreement can be observed. The directly measured gain, simulated gain by using E_r=4.2 and E_r=3.6 for prepreg, and the calibrated measured gain (after de-embedding the loss of the balun and transition) are plotted together. The simulated gain with E_r=3.6 for prepreg still have better agreement with the directly measured gain. The calibrated measured 3-dB gain bandwidth is from 58 GHz to 68 GHz with a peak value of 12.3 dBi at 65 GHz.
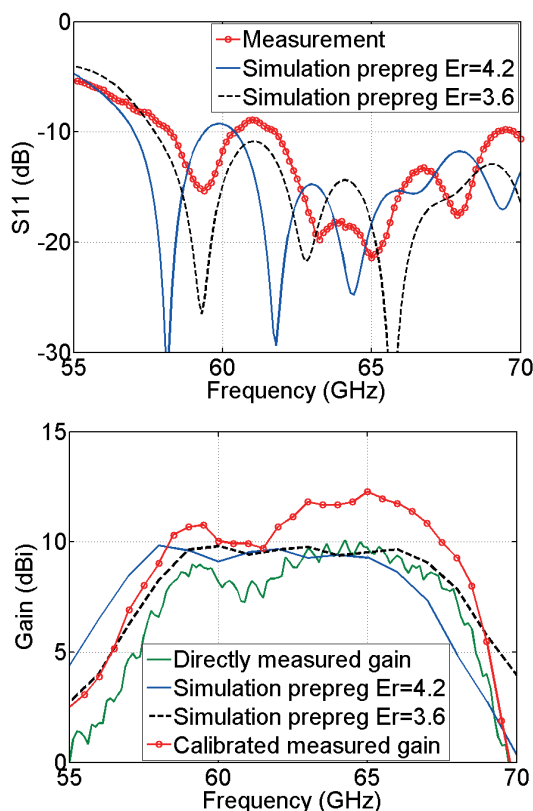
Figure 3.29: Simulated and measured results of the patch array antenna.

The simulated and measured normalized radiation patterns at 62 GHz in E- (y-z plane) and H-plane (x-z plane) are plotted in Figure 3.30. They have very good agreement except the measured sidelobe level of E-plane is higher and the H-plane in negative angles cannot be precisely measured due to the measurement setup (existence of the probe and measurement table). The higher level side-lobe in H-plane is caused by the spurious radiation from the balun. The measurement verifies the simulation so that the simulated patterns without the balun in Figure 3.26 can be trusted.

The demonstrator module has been successfully used in the demonstration of a high data rate communication system with an integrated high-resolution ranging feature [37] [38] as shown in Figure 3.31. The demonstration system consists of a master station and a slave station. A commercial industrial high-definition video camera provides a high data rate stream for the communication path of up to 1 Gbps. The ranging system determines the distance between two stations using the round trip time of flight method. The measurement is from 40 cm distance up to 800 cm with steps of 20 cm, and 200 measurements were implemented for each distance to obtain a statistical mean value. It can be seen from the measured results that the distance between the stations was measured in good precision, i.e. with a standard deviation of about 0.5 cm for most distances, which benefits from the large channel bandwidth (2.16 GHz) in 60 GHz band. As the distance exceeds 500 cm, the multipath reflections (mainly from the ground) for some distances can add destructively with the signal in direct path, resulting in low signal to noise ratio and hence higher standard deviations.
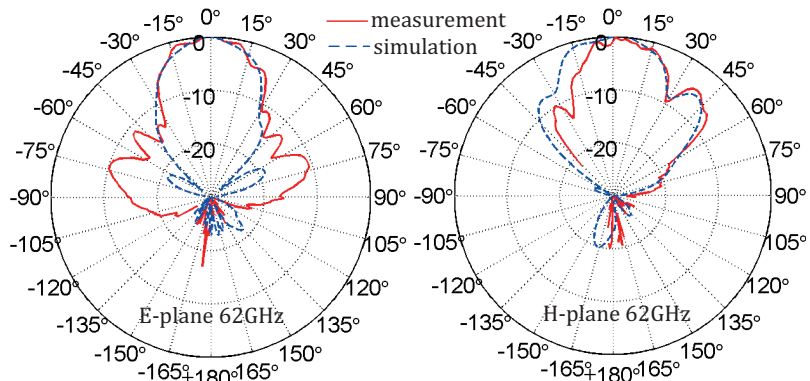
Figure 3.30: Measured and simulated normalized E- (y-z plane) and H-plane (x-z plane) patterns (in dB) at 62 GHz.
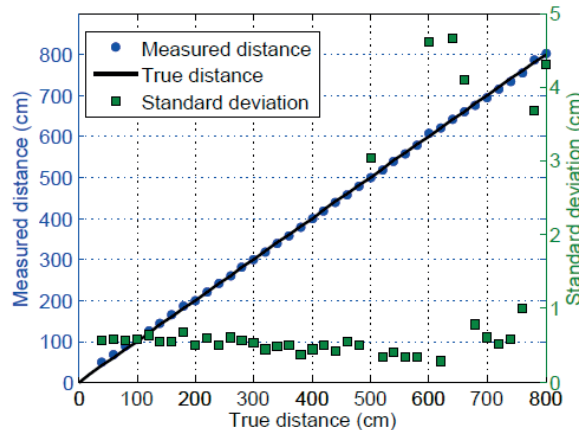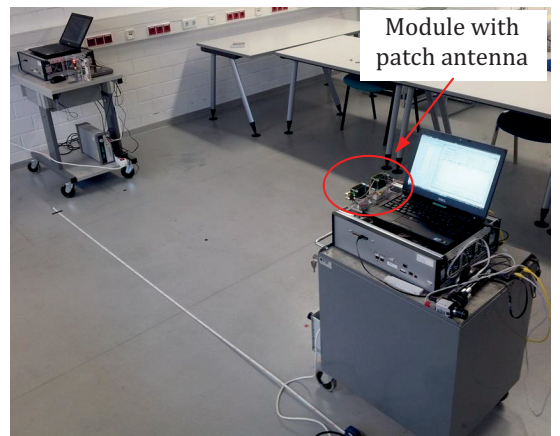
Figure 3.31: (Top) Demonstrator measurement setup; (Bottom) Ranging measurement results [38].

3.4.4   Differential Patch Array Antenna with Beamforming Function

The line-of-sight (LOS) radio link is often obstructed by the moving people or any other obstacles in an indoor environment. In this case a wireless system with beamforming function can maintain its radio link by steering the main beam to the best available transmit/receive direction. A 4-element differential patch antenna linear array has been designed, and the transmitter evaluation board is shown in Figure 3.32. The antenna array is fabricated on RO3003 with a thickness of 250 µm. The 4 patch antenna elements are placed a half-wavelength apart (2.5 mm at 60 GHz), and they are fed individually and differentially by the chip through bond-wire matching structures. The size of the array is about 8.8×8.2 mm^2.
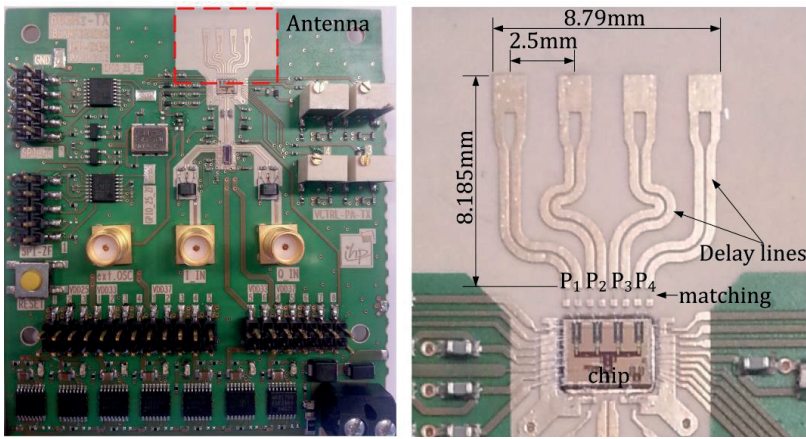
Figure 3.32: Transmitter demonstrator board with 4-element linear phased array antenna.

The feeding network is one important issue for antenna phased arrays. The antenna elements are placed a half-wavelength apart, but the size of the IC is much smaller. The differential feeding lines have to be routed to the IC end with much smaller separation as shown in Figure 3.33. The separation will be limited by the minimum line spacing (typically 100 µm) of PCB technology as well as the ports coupling level. The differential lines should offer similar phase delay and magnitude decay besides lower return loss so that the phased array elements can have the same phase reference plane at their inputs. Sharp bends must be avoided, which will introduce considerable parasitic effects to destroy the impedance matching and change the phase abruptly. Round bends are used in this design, and the simulated results are shown in Figure 3.33. The ports P1–P8 are marked on the drawing of the lines. Due to the symmetric structure, not all the ports are discussed. S11 and S22 are well below -13 dB, showing good input matching to 100 Ω. The ports isolation of S61, S52, and S72 are smaller than -20 dB. S51 and S62 have similar phase and magnitude around 60 GHz, offering the same phase reference plane at the inputs of the patches.

The evaluation board has not yet been measured. Figure 3.34 shows the simulated S-parameters and 3-D radiation patterns at 60 GHz. The ports P1–P4 are marked in Figure 3.32. S11 and S22 are slightly different from each other but both better than -10 dB in the band of 58–62.5 GHz, covering the second channel (59.4–61.56 GHz) of IEEE 802. 15. 3c standard. The coupling between neighboring elements S21 and S32 are below -15 dB. The 3-D radiation patterns are plotted in linear scale for better visualization of radiation direction. The antenna array has a broadside radiation direction with in-phase equal
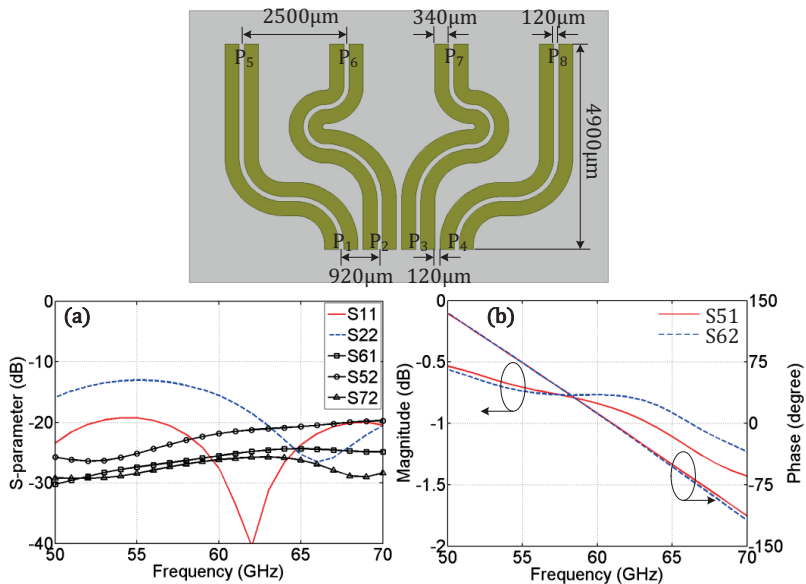
Figure 3.33: Phase delay lines and their simulated S-parameter.
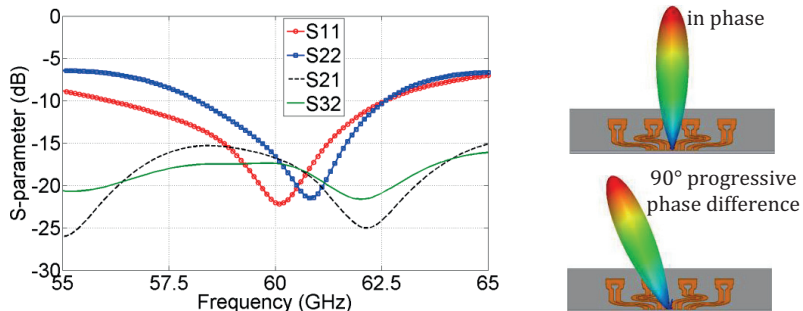
Figure 3.34: Simulated S-parameters and 3-D radiation patterns at 60 GHz (in linear scale) of the phased array antenna.

amplitude excitations, while the main beam is steered by about 24° degrees when they are excited by 90° progressive phase difference from the left to the right. The maximum gain is 13.5 dBi at 60 GHz with a radiation efficiency of 95% for the in-phase excitation, and a maximum gain of 12.4 dBi with a radiation efficiency of 91% is achieved for the latter.

3.5   Conclusions

This chapter demonstrates the possibility and flexibility of designing integrated PCB antennas with good performance in a very low-cost fashion for 60 GHz applications. The design started with characterization and selection of the RF

dielectric substrates. Three commercially available low-cost dielectrics were characterized by using simple planar transmission line method in a wide band, and then verified by a patch resonator in a narrow band around 60 GHz. The mm-Wave interconnects of bond-wire and flip-chip were both studied experimentally. A novel double-bond-wire (about 0.5 mm for each bond-wire in length) compensation structure was proposed, and experimentally proven to have large bandwidth, good repeatability and low-loss of 0.2–0.3 dB at 62 GHz per interconnect [27]. A bunny-ear antenna with end-fire radiation direction, and a patch array antenna with broad-side radiation direction have been designed, fabricated and measured [39]. The bunny-ear antenna features a larger size but a higher gain and bandwidth. The demonstrator with bunny-ear antenna achieved a data rate of 3.6 Gbit/s over a 15-meter distance, which was the best reported analog front-end in silicon technology without beamforming regarding both the data rate and transmission distance at the time of its publication [33]. The patch array has a much more compact size with a moderate gain and bandwidth, which has been successfully demonstrated in a high data rate communication system with an integrated high-resolution ranging feature [37] [38]. A differential linear patch array antenna with one dimensional beamforming function was also been designed. The differential feeding lines were carefully designed to offer similar phase delay and amplitude decay as well as good impedance matching, which is important for the phased array to operate properly.

References

[1]   J. Wells, "Faster than fiber: the future of multi-G/s wireless," *Microwave Magazine*, *IEEE*, vol. 10, no. 3, pp. 104-112, May 2009.

[2]   T. S. Rappaport, N. J. Murdock, and F. Gutierrez, "State of the art in 60-GHz integrated circuits and systems for wireless communications," *Proceedings of the IEEE*, vol. 99, no. 8, pp. 1390-1436, Aug. 2011.

[3]   F. Gutierrez, K. Parrish, and T. S. Rappaport, "On-chip integrated antenna structures in CMOS for 60 GHz WPAN systems," *Global Telecommunications Conference, 2009, IEEE*, pp. 1-7, Nov.-Dec. 2009.

[4]   P. –J. Guo, and H. –R. Chuang, "A 60-GHz millimeter-wave CMOS RFIC-on-chip meander-line planar inverted-F antenna for WPAN applications," *Antennas and Propagation Society International Symposium, 2008, IEEE*, pp. 1-4, Jul. 2008.

[5]   Y. P. Zhang, M. Sun, and L. H. Guo, "On-chip antennas for 60-GHz radios in silicon technology," *Electron Devices, IEEE Transactions on*, vol. 52, no. 7, pp. 1664-1668, Jul. 2005.

[6]   X. Chen, K. Wu, L. Han, and F. He, "Low-cost high gain planar antenna array for 60-GHz band applications," *Antennas and Propagation*, *IEEE Transactions on*, vol. 58, no. 6, pp. 2126-2129, Mar. 2010.

[7]   H. –H. Yeh, and K. L. Melde, "Development of 60-GHz wireless interconnects for interchip data transmission," *Components, Packaging and Manufacturing Technology*, *IEEE Transactions on*, vol. 3, no. 11, pp. 1946-1952, Jul. 2013.

[8]   F. Wollenschläger *et al.*, "Measurement of a 60-GHz antenna array fed by a planar waveguide-to-microstrip transition integrated in low-temperature co-fired ceramics," *Antennas and Propagation*, *2009*, *3rd European Conference on*, pp. 1001-1005, Mar. 2009.

[9]   D. Kam, D. Liu, A. Natarajan, S. Reynolds, and B. A. Floyd, "Low-cost antenna-in-package solutions for 60-GHz phased-array systems," *Electrical Performance of Electronic Packaging and Systems*, *2010 IEEE 19th Conference on*, pp. 93-96, Oct. 2010.

[10] H. Sun, Y. –X. Guo, and Z. Wang, "60-GHz circularly polarized u-slot patch antenna array on LTCC," *Antennas and Propagation*, *IEEE Transactions on*, vol. 61, no. 1, pp. 430-435, Jan. 2013.

[11] D. Titz *et al.*, "60 GHz patch antenna using IPD technology," *Antennas and Propagation Conference (LAPC)*, *2012 Loughborough*, pp. 1-4, Nov. 2012.

[12] U. R. Pfeiffer *et al.*, "A chip-scale packaging technology for 60-GHz wireless chipsets," *Microwave Theory and Techniques*, *IEEE Transactions on*, vol. 54, no. 8, pp. 3387-3397, Aug. 2006.

[13] D. J. Chung, A. L. Amadjikpe, and J. Papapolymerou, "Multilayer integration of low-cost 60-GHz front-end transceiver on organic LCP," *Antennas and Wireless Propagation Letters*, *IEEE*, vol. 10, pp. 1329-1332, 2011.

[14] A. L. Amadjikpe, D. Choudhury, G. E. Ponchak, and J. Papapolymerou, "A compact conformal end-fire antenna for 60 GHz wireless applications," *Antennas and Propagation Society International Symposium*, *2009*, *IEEE*, pp. 1-4, Jun. 2009.

[15] Y. Ma, K. Kawasaki, and H. Msuda, "A wideband bond-wire antenna for millimeter wave intra-communication systems," *Antennas and Propagation*, *IEEE Transactions on*, vol. 61, no. 9, Sep. 2009.

[16] Y. Tsutsumi *et al.*, "Bonding wire loop antenna in standard ball grid array package for 60-GHz short-range wireless communication," *Antennas and Propagation*, *IEEE Transactions on*, vol. 61, no. 4, pp. 1557-1563, Apr. 2013.

[17] T. Kim, and S. Jung, "A multi-antenna 60 GHz CMOS transmitter using wire-bond antenna for high output power," *Circuits and Systems (MWS-*

CAS), *2011 IEEE 54th International Midwest Symposium on*, pp. 1-4, Aug. 2011.

[18] T. Mitomo *et al.*, "A 2-Gb/s throughput CMOS transceiver chipset with in-package antenna for 60-GHz short-range wireless communication," *Solid-State Circuits*, *IEEE Journal of*, vol. 47, no. 12, pp. 3160-3071, Dec. 2012.

[19] P. Herrero, *Millimeter-wave systems and technologies for multi-gigabit wireless transmission applications*, doctorial dissertation, TU Braunschweig, 2010.

[20] http://www.rogerscorp.com/

[21] http://www.arlon-med.com/

[22] A. M. Mangan, S. P. Voinigescu, M. –T. Yang, and M. Tazlauanu, "De-embedding transmission line measurements for accurate modeling of IC designs," *Electron Devices*, *IEEE Transactions on*, vol. 53, no. 2, pp. 235-241, Feb. 2006.

[23] D. Pozar, *Microwave Engineering*, 4th edition, John Wiley & Sons, New York, 2011.

[24] C. A. Balanis, *Advanced Engineering Electromagnetics*, John Wiley & Sons, New York, 1989.

[25] T. P. Budka, "Wide-bandwidth millimeter-wave bond-wire interconnects," *Microwave Theory and Techniques*, *IEEE Transactions on*, vol. 49, no. 4, Apr. 2001.

[26] Y. P. Zhang, M. Sun, K. M. Chua, L. L. Wai, and D. Liu, "Antenna-in-package design for wirebond interconnection to highly-integrated 60 GHz radios," *Antennas and Propagation*, *IEEE Transactions on*, vol. 57, no. 10, Oct. 2009.

[27] R. Wang, Y. Sun, C. Wipf, and J. C. Scheytt, "An on-board differential patch array antenna and interconnects design for 60 GHz applications," *Microwave, Communications, Antennas, and Electronics Systems (COM-CAS)*, *2011 IEEE International Conference on*, pp. 1-5, Nov. 2011.

[28] http://www.finetech.de/home.html

[29] www.epoteck.com

[30] R. Sturdivant, "Balun designs for wireless, mixers, amplifiers and antennas," *Applied Microwave*, pp. 34-44, summer 1993.

[31] S. Glisic, K. Schmalz, F. Herzel, R. Wang, M. Elkhouly, Y. Sun, and J. C. Scheytt, "A fully integrated 60 GHz transmitter front-end in SiGe BiCMOS technology," *Silicon Monolithic Integrated Circuits in RF systems (SiRF)*, *2011 IEEE 11th Topical Meeting on*, pp. 149-152, Jan. 2011.

[32] Y. Sun, K. Schmalz, S. Glisic, R. Wang, and J. C. Scheytt, "An integrated differential 60 GHz sliding-IF receiver in SiGe BiCMOS," *Computer Research and Development (ICCRD)*, *2011 3rd International Conference on*, pp. 297-300, Mar. 2011.

[33] S. Glisic, J. C. Scheytt, Y. Sun, F. Herzel, R. Wang, K. Schmalz, M. Elk-houly, and C. –S. Choi, "Fully integrated 60 GHz transceiver in SiGe BiCMOS, RF modules, and 3.6 Gbit/s OFDM data transmission," *International Journal of Microwave and Wireless Technologies*, vol. 3, special issue 02, pp. 139-145, Apr. 2011.

[34] J. F. Zücher, and F. E. Gardiol, *Broadband patch antennas*, Artech House, MA, 1995.

[35] D. Pozar, "Considerations for millimeter wave printed antennas," *Antennas and Propagation*, *IEEE Transactions on*, vol. 31, no. 5, pp. 740-747, Sep. 1983.

[36] S. Beer, H. Gulan, C. Rusch, and T. Zwick, "Coplanar 122-GHz antenna array with air cavity reflector for integration in plastic packages," *Antennas and Wireless Propagation Letters*, *IEEE*, vol. 11, pp. 160-163, 2012.

[37] M. Ehrig, and M. Petri, "60 GHz broadband MAC system design for cable replacement in machine vision applications," *AEU-International Journal of Electronics and Communications*, vol. 67, no. 12, pp. 1118-1128, Dec. 2013.

[38] M. Ehrig, M. Petri, V. Sark, J. Teran, and E. Grass, "Combined high-resolution ranging and high data rate wireless communication system in the 60 GHz band," *11th workshop on Positioning, Navigation and Communication 2014*, pp. 1-6, Mar. 2014.

[39] R. Wang, Y. Sun, and J. C. Scheytt, "An on-board differential bunny-ear antenna design for 60 GHz applications," *German Microwave Conference*, *2010*, pp. 9-12, Mar. 2010.

4 Integrated On-Chip Antennas

Nowadays all components for transceivers operating in the millimeter-wave frequency range can be realized in silicon technologies with fairly good electrical performance, which makes millimeter-wave systems attractive and affordable for mass products. As frequency goes up to above 100 GHz or even 200 GHz the packaging and assembly of the system, especially the realization of very high frequency interconnects with low-loss becomes extremely difficult, and it takes a significant part of the overall system cost due to the use of special technology and process control. On the other hand the wavelength is getting smaller, e.g. 2.5 mm at 120 GHz, making it both possible and practical for on-chip antenna implementations. However, the substrate of mainstream silicon technologies, either CMOS or BiCMOS, is not suitable for on-chip antenna designs. The doped silicon substrate has a low resistivity, typically 1~50 Ω·cm, which is beneficial for integrated circuit to avoid latch-up but detrimental for on-chip antenna to achieve an acceptable radiation efficiency. In addition, silicon has a dielectric constant as high as 11.9 so that it can support higher order surface waves at high frequencies even with a thin thickness (see Figure 2.10) which will further reduce the efficiency and cause spurious radiation from the truncated chip edges. The insulation layer of the back-end-of-line (BEOL) process in silicon technologies is typically around 15 μm in thickness, which is too thin to make a ground shielded antenna (shielding the antenna from lossy silicon) with acceptable radiation efficiency. Table 4.1 lists some published results of on-chip antenna designs in ordinary low-resistivity silicon technologies. Their gain is negative, and the efficiency is very low (Effi. ≤ 10%) which are not acceptable for most of the applications.

Table 4.1: Reported On-Chip Antennas in Low-Resistivity Si. Technologies

Ref.	Process	Architecture	f_0 (GHz)	-10dB BW (GHz)	Gain (dBi)	Effi. (%)	Chip size (mm^2)
[1]	BEOL CMOS	Inverted-F	61	55–67.5	-19	3.5	2×0.2
[2]	0.18 μm CMOS	Yagi	60	55–65	-10.6	10	1.1×0.95
[3]	0.13 μm CMOS	Slot-ring	89	87.5–90.5	-5.7	7	1.5×1.5
[4]	0.18 μm CMOS	Inverted-F	60	57–64	-15.7	10	0.82×0.71
[5]	0.18 μm CMOS	Loop	65	34–105	-4.4	NA	1.8×1.8

4.1   State-of-the-Art On-Chip Antenna Solutions in Silicon Technologies

Different approaches and technologies have been developed to improve the performance of on-chip antennas. Some state-of-the-art approaches are summarized as following:

A. Substrate Thinning and Antenna Position Optimization

Substrate thinning can cut off higher order mode surface waves, thus improving the radiation efficiency. However, the substrate thinning method is difficult to be implemented for higher frequencies, e.g. above 200 GHz. The cutoff frequency of the surface wave mode TE_1 is about 114 GHz for a grounded silicon substrate with a thickness of 200 µm as shown in Figure 2.10. Further thinning the substrate to increase the cutoff frequency of surface waves is possible, but the mechanical stability and reliability of the too thin wafer becomes an issue. Optimizing the position of the on-chip antenna, i.e. place the antenna close to the edges of the chip, can also improve the radiation performance. It is reported in [6] that the gain of an on-chip dipole antenna was increased from -13.6 dBi to -7.3 dBi with an efficiency of 9% at 60 GHz when it was moved from the center of the chip to the edge of the chip. In the same paper a 2-element Yagi antenna was placed in the corner of the chip, achieving a highest gain of -3.55 dBi with a radiation efficiency of 15.8% at 60 GHz. In [7] a bowtie slot antenna was also placed in the corner of the chip, achieving a measured gain of 0–1 dBi at 94 GHz with a simulated radiation efficiency of 18%. Obviously, this approach requires very high precision of chip dicing process, and the improvement in gain and efficiency is also very limited. The advantage of both substrate thinning and antenna position optimization approaches is that they can be done in a standard volume process without applying any additional technologies.

B. Proton Implantation

The high conductive loss of the silicon substrate is from its low-resistivity, which is beneficial for the circuits. A proton implantation process has been developed to increase the resistivity of the standard silicon substrates from 10 $\Omega \cdot cm$ to 10^6 $\Omega \cdot cm$ only under the selected devices [8]. In their work the implantation energy was reduced to about 4 MeV (resulting in effective implantation depth of 175 µm), which was unavailable in commercial ion implanters, in a special way to avoid contamination issue of degradation of the gate oxide integrity. A coplanar transmission line and a monopole antenna were fabricated by using 4 µm-thick aluminum on 1.5 µm-thick isolation oxide on a silicon substrate of 525 µm-thick. The measured results showed that the loss was considerably lower for both the transmission line and antenna on the proton-implanted silicon than that on the standard silicon. The average and peak gain

of the antenna with proton implantation is 4.2 and 6.4 dB higher (at 103 GHz) than that on standard silicon, respectively. This approach can reduce the conductive loss of the substrate, but it is not beneficial for the suppression of surface waves, which can also largely degrade the radiation performance of the antenna. Furthermore, it requires special equipment in the foundry and non-standard process, thus increasing the cost.

C. Superstrate and Dielectric Resonator Antenna on Silicon

Bosch published a parasitic half-wavelength patch resonator fabricated on a quartz superstrate in [9], which is glued on top of an on-chip patch antenna by epoxy adhesive to improve the radiation performance. It achieved a radiation efficiency of more than 50% for 77 GHz applications, and it was afterwards scaled for 122 GHz applications with nearly the same efficiency of 50% and a gain of 6 dBi [10]. A similar method, a slot-ring resonator fabricated on a quartz superstrate and glued on top of the chip, has been employed in [11] for 94 GHz applications, achieving a gain of 2 dBi with an efficiency of 50–60%. The antenna gain was further increased to 3–6 dBi and 6–9 dBi by placing a metallic short horn antenna (1 mm in height) and a long horn antenna (5 mm in height) on top of the slot-ring antenna. They were the highest reported gains of on-chip antennas at the time of its publication [11]. However, the on-chip antenna with metallic horn is not a planar structure any more, which would be more difficult for packaging. Instead of a metallic resonator on superstrate, one and two dielectric resonators as reported in [12] were glued on top of an on-chip meander slot antenna, achieving a gain of 2.7 dBi and 4.7 dBi with a radiation efficiency of 43% at 130 GHz, respectively. The superstrate antenna and dielectric resonator antenna on silicon can significantly improve the radiation efficiency of an on-chip antenna, and they do not occupy additional chip area since they are vertically positioned on the chip. However, they require precise alignment and gluing process to place the resonator on the right position of the chip, which complicates the assembly process and eventually increases the total cost.

D. Localized Backside Etched On-Chip Antenna

Localized backside etching (LBE) process (also named silicon micromachining process in literature) can selectively remove the lossy silicon with high dielectric constant in critical areas to reduce the loss and suppress the surface waves simultaneously. The silicon backside etching can be performed by wet etching or dry etching. A wet etching process will yield slanted silicon walls around the etched cavity due to the anisotropic nature of the chemical etching [13] [14], which results in larger silicon removal area and restrictions on the etched shape. The modern dry etching is based on deep reactive ion etching technology, which enables very high aspect ratio. It allows the etched areas with arbi-

trary shapes to be in the close vicinity of the active devices, thus obtaining a more compact chip size. More importantly, the localized backside etching process based on dry etching is part of the standard through silicon vias technology, and is available in all IHP's SiGe BiCMOS technologies [15] as well as other semiconductor technologies. There is compromise between the antenna performance and other issues like mechanical stability and chip size. A larger silicon etched area under the antenna can enhance the radiation efficiency [16], but it leads to reduced mechanical stability of the chip due to the fact that the very thin insulator layer suspended in the air is fragile without the support of silicon. Moreover, the chip size will be larger because no active components can be placed in the etched areas. A micromachined meander dipole antenna, which was designed to be integrated with 24 GHz differential SiGe circuits, was presented in [17]. The silicon under the dipole antenna was removed, and a measured gain of 0.7 dBi was achieved. Afterwards, the same author published a full wave-length square wire-loop and a slot-loop antenna in [18]. The silicon was only removed under the radiating slot and the wire by forming trenches instead of forming complete cavities so that the majority of the bulk silicon within the aperture of the antennas is preserved to enable the integration of active devices, thus saving the chip area. A positive gain of 1.0 dBi at 24 GHz for the wire-loop antenna and 1.5 dBi at 29.5 GHz for the slot-loop antenna have been achieved.

A comparison of the state-of-the-art on-chip antennas in low-resistivity silicon processes is given in Table 5.1 in chapter 5. Extensive study and discussions of on-chip antennas based on IHP's standard SiGe BiCMOS technologies are presented in the following sections. Several on-chip antenna designs as well as fully integrated mm-Wave transceivers are developed and demonstrated, targeting higher performance, better mechanical stability, better immunity to fabrication tolerances, and more compact size.

4.2   Technology Overview

All on-chip designs in this chapter are based on IHP's 0.25 μm and 0.13 μm SiGe: C BiCMOS technologies with cut-off frequency of up to 500 GHz for integrated HBTs, which are especially suited for applications in the higher GHz bands. The on-chip antennas are implemented in the BEOL process, whose schematic views are shown in Figure 4.1. The BEOL process offers 5 aluminum layers in 0.25 μm technology and 7 aluminum layers in 0.13 μm technology buried in the insulator of silicon dioxide (SiO_2), respectively. The top thick metal layers of TM2 and TM1 are usually used to construct RF passive components to reduce the metallic loss. All metal layers can be interconnected by stacked via arrays. The silicon substrate has a low-resistivity of 50 Ω·cm. The original thickness of the wafer is 750 μm, but it can be back-grinded to a
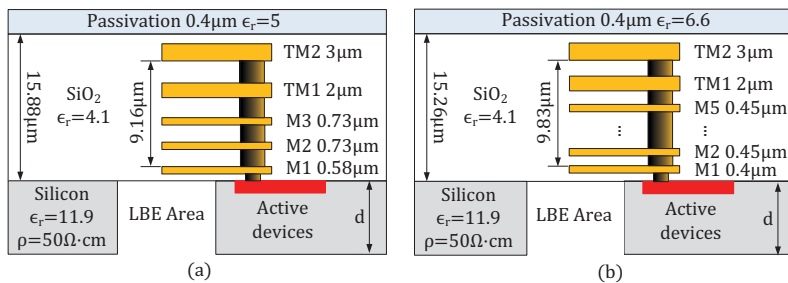
*Figure 4.1: Schematic view of the technologies (a) 0.25 µm; (b) 0.13 µm. (not to scale)*

minimum thickness of 100 µm by request to have a desired silicon thickness d. The LBE process is available for all technologies.

4.3   On-Chip Antenna Designs with Air Cavity Under the Radiator

The radiation performance of the on-chip antenna can be greatly improved by removing the silicon under the radiator. In this way the antenna is only supported by the very thin (~16 µm) membrane (SiO$_2$ + passivation), and suspended in the air.

4.3.1   130 GHz Antenna Design and Prototype Measurement

Figure 4.2 shows a conceptual drawing of a double folded dipole on-chip antenna design. The microstrip line fed double dipole antenna is realized on TM2 layer in 0.25 µm technology. M1 is used to form the ground plane for both the microstrip line and the antenna. The dipoles are grounded by stacked vias from TM2 to M1 layer. The chip is usually glued on a relatively large ground plane of a package or module, so an infinitely large ground plane is included in the simulation that forms a reflector for the antenna. The operation principle of horizontally oriented dipole antennas above a reflector has been theoretically discussed in chapter 2. The dimension of the dipoles is fixed by 3-D electromagnetic simulations. Larger LBE area is beneficial for the antenna performance but it is prohibited to be made excessively large because the very thin membrane of large size is easy to be damaged, and a large chip area is expensive. Therefore, the silicon is in the vicinity of the antenna (e.g. the silicon side-frames with width b), still having non-negligible influence over the radiation especially when the chip is thick. The distance between the dipoles and the reflector, which is approximately the thickness (d) of the silicon, is an important parameter for the antenna radiation characteristics (Figure 2.5 in chapter 2) as well as the input impedance. The parameters w (etching size), d (sili-

con thickness), and b (silicon side-frame width) were studied in simulations by keeping two parameters constant and sweeping the rest one as shown in Figure 4.3. The gain in Figure 4.3 is the product of the directivity and the radiation efficiency, which takes into account the conductor loss and the dielectric loss, but excludes the impedance mismatching loss at the input of the antenna. The radiation efficiency and gain at 130 GHz increase monotonically as the size of LBE area (w) is increasing as shown in Figure 4.3 (a), while the directivity does not change much. The increase of efficiency and gain slows down when w is larger than 1600 μm, so the LBE size is fixed to be $1600 \times 1600 \ \mu m^2$ as a balance between the antenna performance and mechanical stability. The directivity, gain and efficiency all fluctuate with the distance (d) between the dipole and reflector, which are shown in Figure 4.3 (b). When d is small, there is strong coupling between the antenna and the reflector so that the metal ohmic loss is high and the radiation efficiency is low. The efficiency increases with d until d=300 μm, achieving a peak radiation efficiency of 71%. As the silicon substrate becomes further thicker it absorbs more radiated fields from the antenna and reflected waves from the reflector so that the dielectric loss dominates, and there is stronger spurious radiation from the truncated edges of the silicon, which can significantly affect the directivity and gain. d=700 μm is chosen in the design which gives a high gain (~8.5 dBi) and a moderate efficiency (~63%) at 130 GHz, and more importantly, it is feasible to be achieved from its original thickness of 750 μm even with a relatively large LBE area. However, with thick silicon substrate the strong spurious radiations must be seriously considered, and the chip size should be carefully optimized. Figure 4.3 (c) shows that the radiation characteristics change drastically with the substrate geometry, i.e. the width (b) of the silicon side-frames. b is swept in steps of 170 μm, which is approximately a quarter wavelength in silicon at 130 GHz.
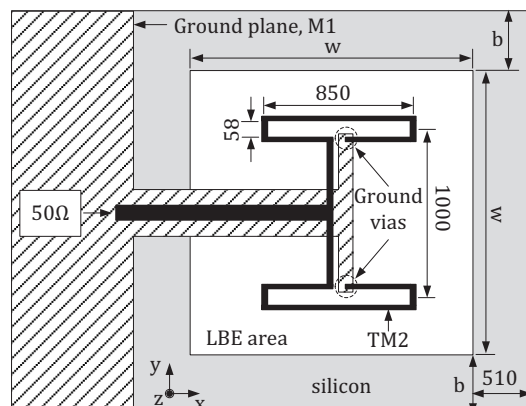

Figure 4.2: Conceptual drawing of the 130 GHz double folded dipole antenna with LBE process in 0.25 μm technology. (Unit in μm, not to scale)
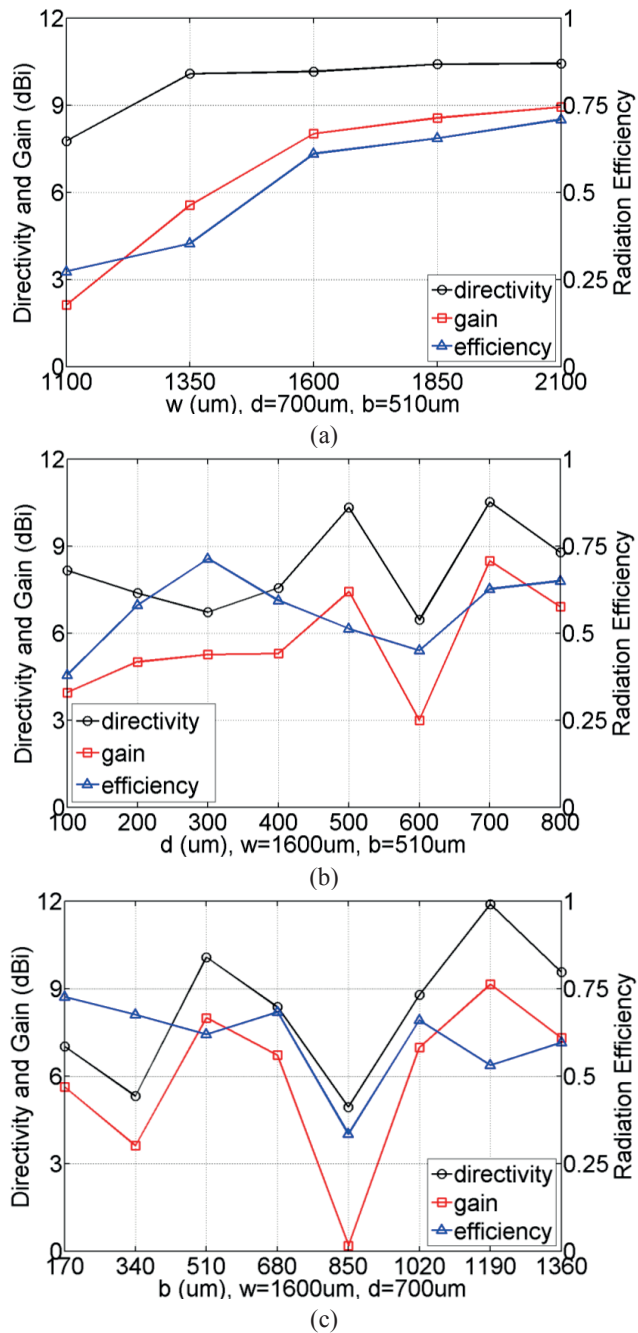
Figure 4.3: Parameters study of the on-chip antenna at 130 GHz with LBE process by sweeping (a) LBE size w, (b) silicon thickness d, and (c) silicon side-frame width b.
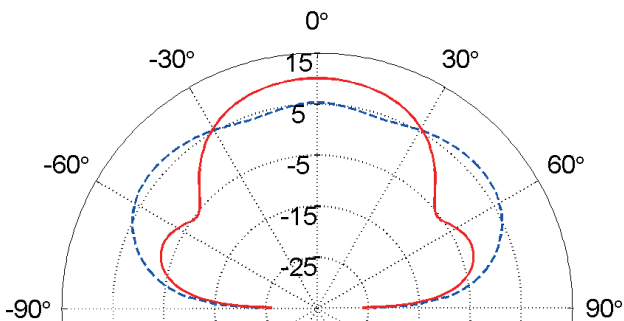
Figure 4.4: Simulated radiation patterns (directivity in dBi) in H-plane (yz plane) at 130 GHz for b=340 µm (dashed line) and b=510 µm (solid line).

Figure 4.4 compares the radiation patterns (directivity) at 130 GHz in the H-plane (yz-plane) for b=340 µm and b=510 µm, which has a lower directivity and a higher directivity, respectively. We can clearly see that the spurious radiations from the silicon side-frames distort the radiation pattern and lower the directivity for the case of b=340 µm, although its radiation efficiency is as high as about 68%.

An antenna prototype was fabricated and shown with measured dimensions in Figure 4.5. The LBE area is not a perfect square, and the maximum value of parameter w is 1630 µm due to the large etching area and some over-etching effects. The thickness of the silicon substrate (d) is about 710 µm, and the width of the silicon side-frames (b) is about 520 µm. The chip was glued on the copper plane of a PCB in the measurement by thermally conductive but electrically nonconductive adhesive (WLK 30 from Fischer Elektronik). This adhesive and a similar one (thermally conductive but electrically nonconductive) of Epo-TEK 930-4 from Epoxy Technology were used for all on-chip antennas presented in this thesis. It can be seen that there is little glue inside the air cavity after curing by leaving the cavity area free of glue when applying the thin glue on-board. The antenna was measured by a microwave probe with 100 µm pitch (calibrated to 50 Ω at the probe tips). The probing pads and the transition introduce impedance mismatching and loss to the antenna measurement. The loss of the probing pads was estimated by the measurement of a back-to-back calibration structure, and then calibrated out from the measured gain.

Figure 4.6 shows the S11 and the gain of the antenna prototype. The simulated (with measured dimensions) and measured S11 agree with each other. The small discrepancy is probably from the fabrication tolerances which were not fully modeled in the simulation. The measured S11 is better than -10 dB over a wide frequency band of 127–170 GHz. The calibration structure was measured up to 140 GHz, so the gain of the antenna was calibrated up to this frequency, too. The antenna gain is higher than 0 dBi almost over the entire measured
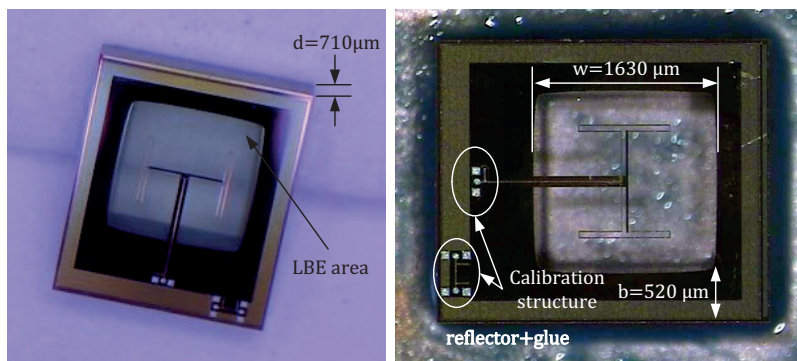
Figure 4.5: (Left) Perspective view of the on-chip antenna without reflector; (Right) Top view of the on-chip antenna with reflector and glue.
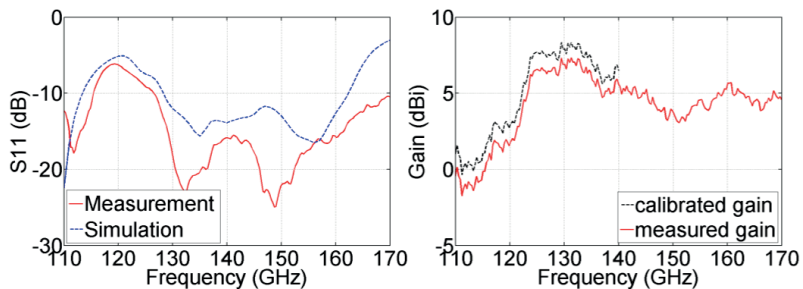

Figure 4.6: (Left) Simulated and measured S11; (Right) Measured gain and calibrated gain.
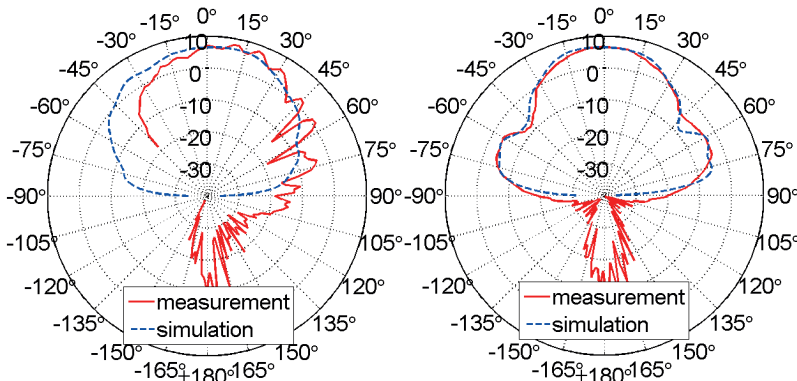

Figure 4.7: Simulated and measured E-plane (left) and H-plane (right) radiation patterns at 130 GHz. Unit in dBi.

bandwidth from 110 GHz to 170 GHz. The calibrated gain is about 7.5–8.4 dBi in the band of 124–134 GHz, which is comparable to on-board or in-package antennas. To the best of my knowledge, the achieved peak gain is the highest reported value to date for planar on-chip antennas based on low-resistivity silicon technologies. The simulated (with probing pads) and measured E-plane (xz-plane) and H-plane (yz-plane) radiation patterns at 130 GHz are compared in Figure 4.7, and they have excellent agreement. The simulated radiation efficiency at 130 GHz is 60%. The ripples in E-plane are from the waveguide probe (Figure 2.13) in the measurement setup for D-band (110–170 GHz), which is in the close vicinity of the small on-chip antenna under test (AUT). The spurious radiations from the probe as well as reflections at its structures can interfere with the radiations from the AUT (especially in the E-plane), and the interference can be constructive or destructive, depending on the frequency and observation angle [7]. The H-plane is smooth. The 3-dB beamwidth is about 60° and 46° in E- and H-plane, respectively.

4.3.2   245 GHz Transceiver with Integrated On-Chip Antenna

A 245 GHz sensor system for gas spectroscopy has been realized, which includes a SiGe TX and a SiGe RX with the same integrated on-chip antenna in IHP's 0.13 µm technology. The photographs of the transmitter and receiver are shown in Figure 4.8. The TX takes a chip area of 2.34×1.35 mm^2, consisting of a 120 GHz push-push voltage controlled oscillator (VCO) tuned by external PLL, a PA, a frequency doubler, and an on-chip antenna [19]. The RX takes a chip area of 2.7×1.3 mm^2, consisting of a push-push VCO for the 122 GHz range, which can be tuned by an external PLL, an LNA, a Gilbert-cell subharmonic mixer, and an integrated antenna [20]. The on-chip antenna is interconnected to the TX/RX by a 50 Ω on-chip microstrip transmission line. It would be extremely difficult to interconnect the circuit and off-chip antenna at this frequency by any external interconnects due to excessively large parasitic effects and losses. The on-chip antenna was a scaled and modified design of the 130 GHz antenna as depicted in Figure 4.9. A smaller LBE area with a size of 800×400 µm^2 is applied under each dipole so that a silicon bridge with a thin width of 100 µm is left in the middle. This can significantly improve the mechanical stability of the structure, allowing a thinner and optimized chip thickness of 200 µm with high yield to suppress substrate waves and reduce spurious radiations for higher performance.

The silicon around the antenna is covered by the ground plane in M1 layer, and this antenna also works with a reflector. The M1 layer and the reflector form a parallel plate waveguide locally, which has higher cut-off frequencies for higher order substrate waves than a grounded dielectric for the same thickness (Figure 2.12 in chapter 2).

The antenna gain was estimated in both demonstrator and as a standalone component which was cut out from the transmitter chip with the probing pads of the transmitter. The measurement setup of the demonstrator is shown in Figure 4.10 (left). The demonstrator consists of an optical bench for movable mounting of TX and RX. A base module provides all the supply voltages, the controllable reference frequency for PLL, and data converters in a microcontroller. The carrier board holds the transmitter chip on a small socket with plugs. The transmitted signal is received by a standard WR-3.4 horn antenna with 25 dBi gain (specified at 270 GHz), and it is then down-converted by a harmonic mixer and analyzed using a spectrum analyzer. The receiver is calibrated by using a power meter. The whole setup of the demonstrator is controlled by a laptop through USB connection. The transmitter and receiver were placed 0.5 m (measured from TX antenna to RX antenna) apart to have a far-field condition. Knowing the distance and frequency, the free-space loss L_0 can be calculated by equation (2.8). Then the effective isotropic radiated power (EIRP) can be extracted as (in dB)

$$EIRP = P_t + G_t = P_r - G_r + L_0 \qquad (4.1)$$
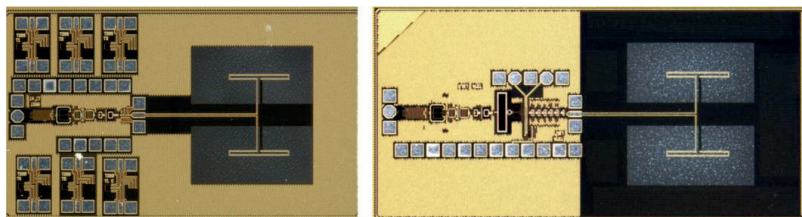
Figure 4.8: Photographs of the 245 GHz transmitter (left, 2.34 × 1.35 mm^2) and receiver (right, 2.7 × 1.3 mm^2) chip with integrated antenna.
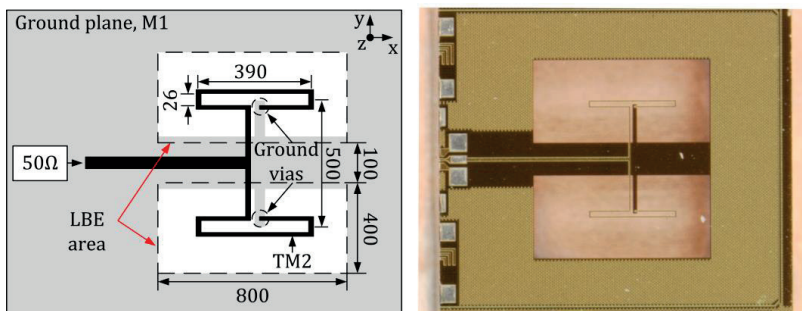
Figure 4.9: (Left) Conceptual drawing of the 245 GHz double-folded dipole antenna with LBE process in 0.13 μm technology (Unit in μm, not to scale), and (Right) the photograph of the antenna cut out from the transmitter as a standalone component for measurement.
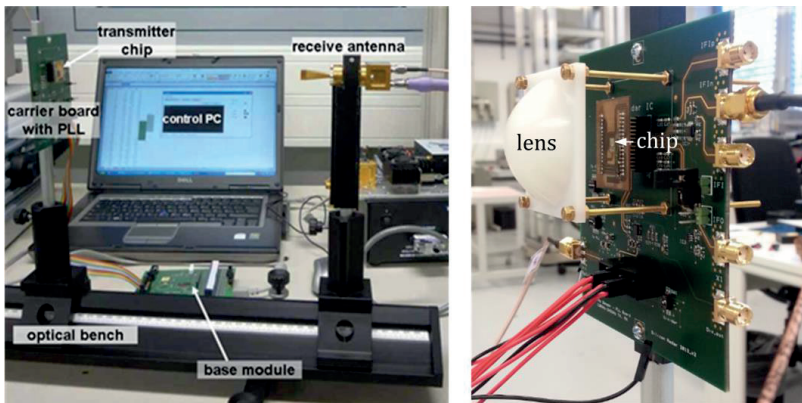
Figure 4.10: (Left) 245 GHz demonstrator measurement setup, and (Right) demonstrator with lens.
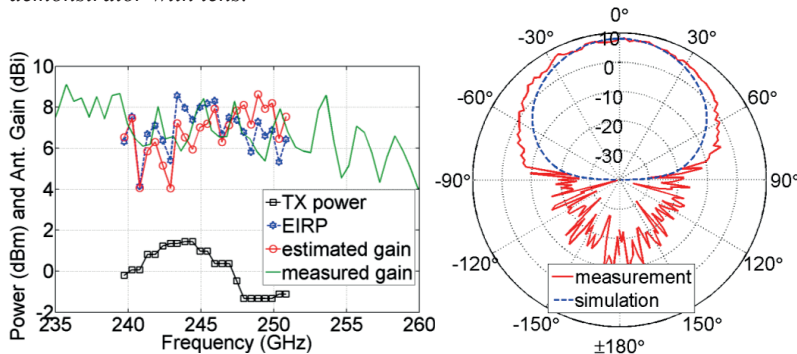
Figure 4.11: (Left) Measured results of the demonstrator; (Right) Measured and simulated H-plane patterns at 245 GHz (Unit in dBi).

where P_r is the measured received power, G_r is the gain of the standard receive horn antenna, P_t is the transmitted power, and G_t is the gain of the on-chip antenna. Therefore, the antenna gain G_t can be estimated by subtracting the on-wafer measured output power of the transmitter P_t (without antenna) from the EIRP. The standalone antenna was also measured to verify the estimated gain in the demonstrator.

Figure 4.11 shows the measured results. The estimated gain, measured gain, EIRP, and the output power of the transmitter are plotted in the same figure. The measurement for 245 GHz is extremely challenging that both the estimated gain and measured gain show some fluctuation, but they generally agree with each other. The measured gain varies between 6 to 8 dBi in a wide band of 235–252 GHz, while the estimated gain shows a similar result in the band of 244 to 251 GHz. The EIRP reaches 7–8 dBm at 245 GHz. To the best of our knowledge, this is the highest reported EIRP at 245 GHz for a SiGe transmitter with a single on-chip antenna to date. The simulated and measured H-plane

patterns at 245 GHz have good agreement, and they do not have sidelobes as that in Figure 4.4 for the 130 GHz antenna, indicating less spurious radiation from the thinner substrate. The simulated radiation efficiency is about 75%. With high radiation efficiency the gain of the antenna can be significantly increased by placing a lens above it to focus the radiated energy as shown in Figure 4.10 (right). The lens was developed by the Karlsruhe Institute of Technology (KIT). It is made of High Density Polyethylene (ϵ_r=2.32) with a diameter of 40 mm and a focal length of 25 mm. The estimated gain (on-chip antenna plus lens) in the far-field (>2.6 m) is about 25 dBi. The 245 GHz transmitter and receiver were used for a gas spectroscopy application demonstrated in [21].

Another way to obtain a high EIRP in the 245 GHz band is the implementation of a TX array with integrated antenna array as shown in Figure 4.12, achieving spatial power combing. The chip takes an area of 5.4 × 3.7 mm^2 with a thickness of 200 µm. The TX array consists of 4 transmitters, which includes a 120 GHz two-stage PA, a frequency doubler, and an integrated antenna. The transmitters are fed by a local oscillator (LO) through a Wilkinson divider network. The LO is comprised of a 120 GHz push-push VCO with an 1/64 frequency divider for the fundamental frequency, a 120 GHz differential two-stage PA as used also for the TX, and an external PLL [22]. The folded dipole elements of the antennas are placed 600 µm apart from each other, which is approximately half-wavelength in free-space at 245 GHz. The TX array was measured on-wafer. The transmitted mm-Wave signal was received by a commercial receiver (R&S ZVA-Z325 Converter) attached to a standard WR-3.4 horn antenna with a gain of 25 dBi (specified at 270 GHz). The distance between the horn
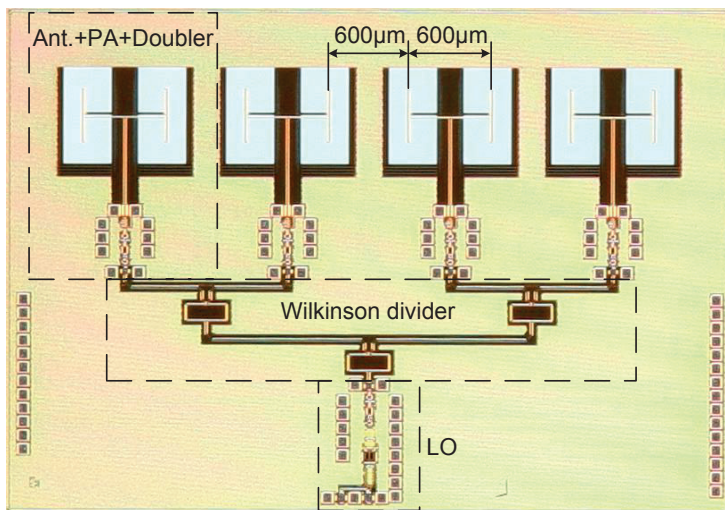
Figure 4.12: Photograph of the fabricated 245 GHz TX array chip. Chip size: 5.4 × 3.7 mm^2.

antenna and the TX array on-wafer was set to 9.9 cm. We also measured a single TX with a single on-chip antenna by the same measurement setup. Figure 4.13 presents the uncalibrated received power by the receiver for the TX array and the single TX. We observe that the received power from the TX array is about 11 dB (theoretically 6 dB more output power of the circuit due to the 4 TXs) higher than that of the single TX, which is the gain in EIRP of the TX array by spatial power combining.
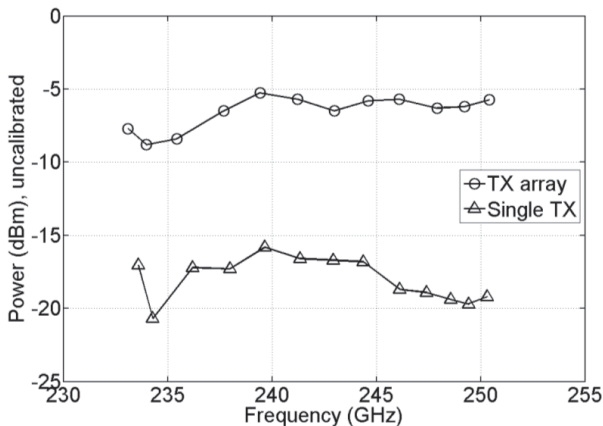
Figure 4.13: The uncalibrated received power by the receiver from the TX array and the single TX.

4.4   On-Chip Antenna Designs with Air Trenches Around the Radiator

The antenna with air cavity under the radiator shows superior performance in the transceiver, but the thin membrane supported radiator is possibly damaged by external forces. In that case the antenna is broken together with the fragile membrane, and the transceiver can no longer function. On-chip antennas with air trenches around the radiators have been developed to overcome this problem by sacrificing a little antenna gain and some bandwidth. In the designs no silicon is removed under any metal structures so that the antenna could work even if the suspended membrane over the air trenches is damaged. Furthermore, since the radiators are placed over the silicon substrate with high permittivity, the size of the radiators is smaller than that on the suspended membrane.

4.4.1   Patch Antenna

A patch antenna has been designed as shown in Figure 4.14 for 122 GHz applications. The radiator and the feeding transmission line are realized on the TM2 layer, while the ground plane of the feeding line is formed on M1 layer. The

patch radiator is surrounded by closely spaced ground conductor, which looks similar as a slot-loop antenna. However, studies [23] [24] have shown that this antenna configuration behaves more similar to a microstrip patch antenna, whose resonant frequency is determined by the patch length (half-wavelength). It is known that the field is strongest at the two end edges along the patch length. Therefore, the silicon is removed only in the critical areas near the maximum field to minimize the loss. The dimensions of the etched air trenches are determined by compromising between the antenna performance and the chip area. All metal structures, including the patch radiator and the feeding transmission line, are completely supported by the silicon bulk so that this chip is mechanically robust. The total area of the antenna, including the air trenches and the patch, is only 780×685 μm^2 due to the high permittivity of the silicon substrate. As the previous on-chip antenna designs, the antenna chip will be glued on a metal plane which acts as a reflector. The thickness of the chip was designed to be a standard thickness of 370 µm of the used technology, which also offers good radiation performance.

The LBE process normally has over-etching effects, especially at the boundary between the SiO_2 and the silicon, due to the process nature as shown in Figure 4.15. The over-etched corners were assumed to be rounded with a radius of r instead of right angles in the study, but in reality the profile will probably be irregular. The silicon is extended out from the two most important edges of the patch antenna for δ=10 µm to partially compensate the over-etching effects without sacrificing much of the radiation efficiency, guaranteeing the firm support for the radiator. Figure 4.16 shows the simulated S11 for r=0 (no over-etching), 20, 40, and 60 µm, which represent different extent of the over-etching effects. The resonant frequency gradually moves towards higher band as r increases, because the effective dielectric constant is reduced when the
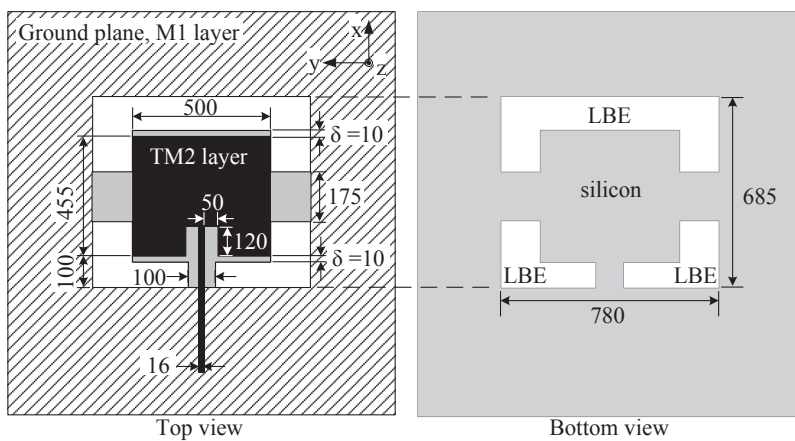
Figure 4.14: Patch antenna design with LBE. (Unit: µm, not to scale.)
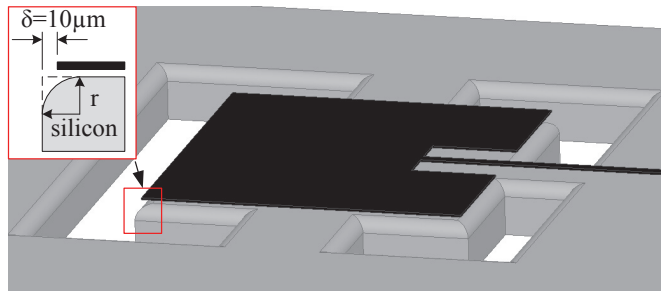
Figure 4.15: Illustration of the possible over-etching effects of the LBE pro-cess. The on-chip ground plane in M1 layer is not drawn for better visualiza-tion.
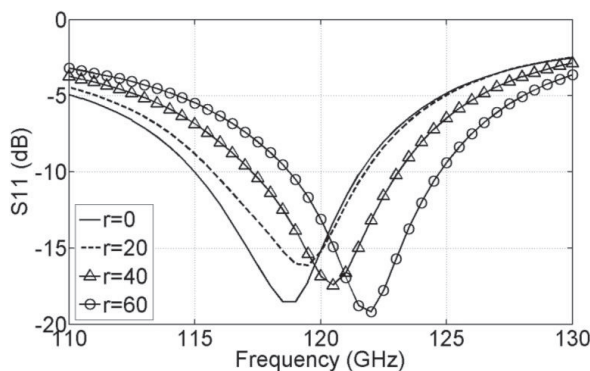
Figure 4.16: Simulated S11 of the patch antenna for different extent of over-etching effects. (r = 0, 20, 40, and 60 μm.)

silicon under the radiator is partially removed. Apparently, a wider bandwidth in the design is desired to tolerate the possible fabrication and assembly toler-ances.

The fabricated antenna prototype is shown in Figure 4.17, and we can observe the over-etching effects. The antenna was characterized by a microwave probe with 100 μm pitch (calibrated to 50 Ω at the probe tips). The signal pad (S) for probing is realized on TM2 layer, and designed to be close to the 50 Ω mi-crostrip feeding line in width (W_s=30 μm for the pad, and 16 μm for the mi-crostrip line) and short in length (L_s=60 μm), which was experimentally proven sufficient to land the probe. The ground pads (G) are interconnected from the TM2 layer to the on-chip ground plane (M1 layer) by the stacked via arrays, which are modeled in the simulation as a solid box as depicted in Figure 4.17. The simulation and measurement show that the pads have little influence over either the S11 or the gain measurement, so no de-embedding technique is re-quired. The S11 has been measured for 6 samples in different positions of a wafer, including the sample close to the edge and in the central area of the wa-

fer to take into account the non-uniform over-etching effects. In Figure 4.18 we can see that the resonant frequencies of the samples vary from about 122 GHz to 124 GHz. However, the -10 dB impedance bandwidth covers 120–125 GHz for all measured samples. The wafer is large in size and the silicon substrate is lossy, so we can expect that there is almost no reflection of the substrate waves coming back from the truncated edges of the wafer to disturb the S11 measurement. The wafer was fixed on the metal chuck of the probe station by vacuum, and the metal chuck serves as the reflector for the antenna in the on-wafer measurement.

Two samples were characterized on-board. The adhesive will raise the chip slightly above the PCB, and its thickness after curing was estimated to be 10–30 µm, which is thin compared with the chip thickness of 370 µm. In the simulations the thickness (t) of the adhesive was assumed to be 10, 20, 30, and 40 µm to study its influence, but no over-etching effects were included. Figure 4.19 compares the measured and simulated S11. The measurement and simulation have agreement despite of some difference in resonant frequency probably due to the exclusion of over-etching effects in the simulation. The simulated S11 for different adhesive thickness is almost identical, because the chip is thick so that small variations in adhesive thickness do not noticeably change the input matching. The difference in S11 for the two measured samples could be from the fabrication tolerances. Figure 4.20 shows the simulated and measured antenna gain. Their shapes agree with each other. There are variations in gain for different adhesive thickness in the simulations due to the changed distance between the radiator and the reflector. The measured gain is 4–6 dBi for both samples in the frequency band of 117–125 GHz, covering the ISM band of 122–123 GHz. The simulated and measured normalized radiation patterns at
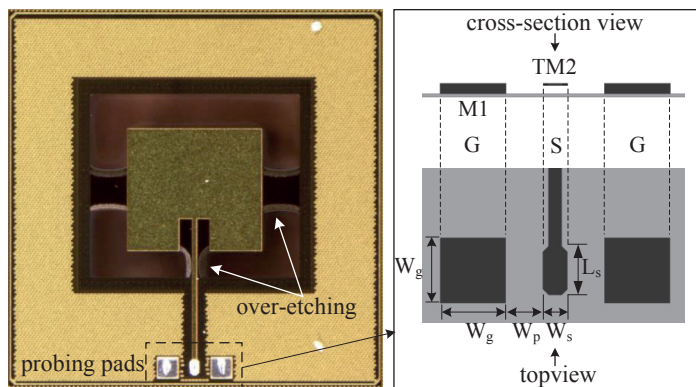
Figure 4.17: Fabricated prototype of the patch antenna (chip size: 1.35 × 1.35 mm²), and the schematic drawing of its probing pads. (W_g=80, W_p=45, W_s=30, and L_s=60, unit in µm.)
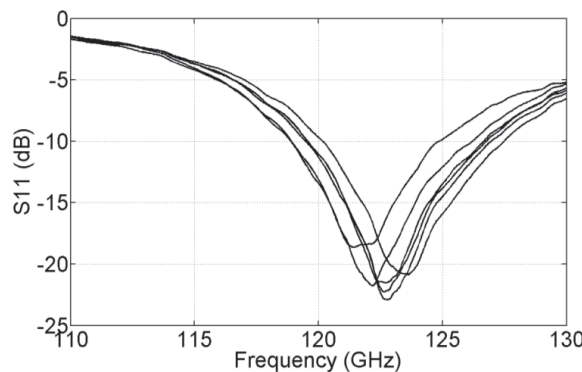
Figure 4.18: On-wafer measured S11 for 6 samples of the on-chip patch antenna.
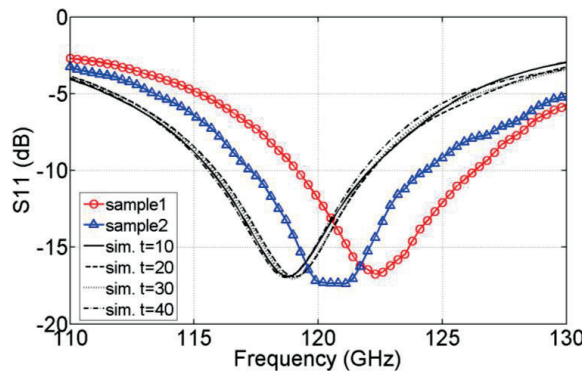
Figure 4.19: On-board measured (meas.) and simulated (sim.) S11 of the patch antenna. Adhesive thicknesses are t=10, 20, 30, and 40 μm in the simulations.
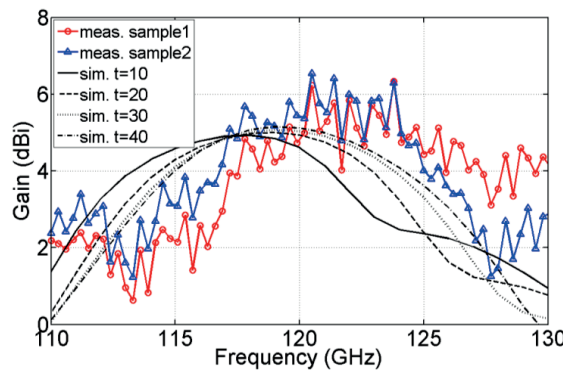
Figure 4.20: On-board measured and simulated (adhesive thickness t=10, 20, 30, and 40μm) gain of the patch antenna.
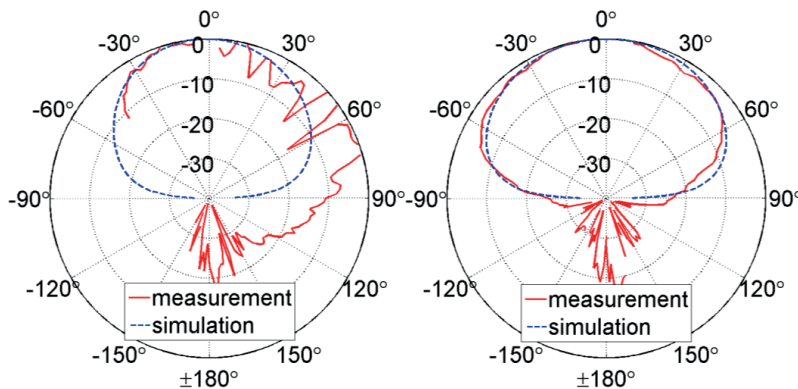
Figure 4.21: Simulated and measured normalized radiation patterns of the patch antenna at 122 GHz in E- (left) and H-plane (right). Unit in dB.

122 GHz are compared in Figure 4.21. They agree with each other. The simulated 3-dB beamwidth is 60° in E-plane (xz-plane) and 94° in H-plane (yz-plane). The measured gain is about 5–6 dBi at 122 GHz with a simulated radiation efficiency of 70–75%.

4.4.2   Double Folded Dipole Antenna

A double folded dipole antenna with surrounding air trenches was designed as shown in Figure 4.22 with detailed dimensions given in Table 4.2. The model of planar asymmetrical folded dipole antenna has been studied in section 2.2.1, whose input impedance (Z_{in}) can be optimized by tuning the widths of the driven element (w_{d1}) and the parasitic element (w_{d2}) as well as their separation (s_{d2}).

The dipoles and their microstrip feeding lines are realized on the TM2 layer, while the ground plane is formed on the M1 layer. The antenna will be glued on the metal plane of the package, which acts as a reflector for the antenna. The two folded dipoles together with the reflector form a 2-element broadside array. As discussed in section 3.4.3, the radiation efficiency of printed broadside antennas can be improved by forming an antenna array with cophasal excitation of the array elements placed half wavelength apart. The two folded dipole elements are placed $2L_{ds}$ (1030 µm, measured from the folded dipole slot center) apart from each other in this design, which is close to half-wavelength (1250 µm) in free-space at 120 GHz. The chip thickness is the same as the patch antenna design presented in last section (370 µm), which is a standard wafer thickness of the used technology and offering good performance. Air trenches are formed around the dipoles by the LBE process, while no silicon is removed under any metal structures. The air trenches with width (w_{tr}) of 200
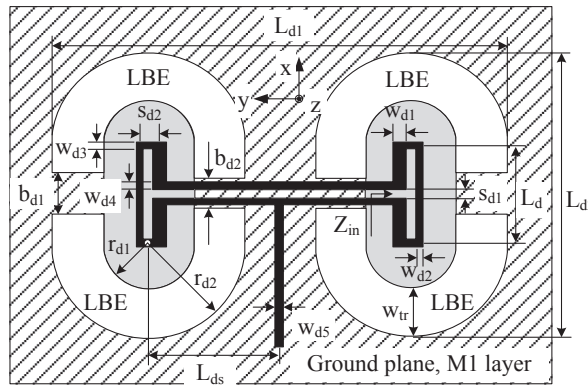
Figure 4.22: Double folded dipole antenna design (not to scale).

Table 4.2: Dimension of the Double Folded Dipole Antenna (in µm)

w_{d1}	w_{d2}	w_{d3}	w_{d4}	w_{d5}	w_{tr}	s_{d1}	s_{d2}
70	5	14	5	16	200	25	57.5
b_{d1}	b_{d2}	r_{d1}	r_{d2}	L_d	L_{ds}	L_{d1}	L_{d2}
150	100	175	375	380	515	1790	1130
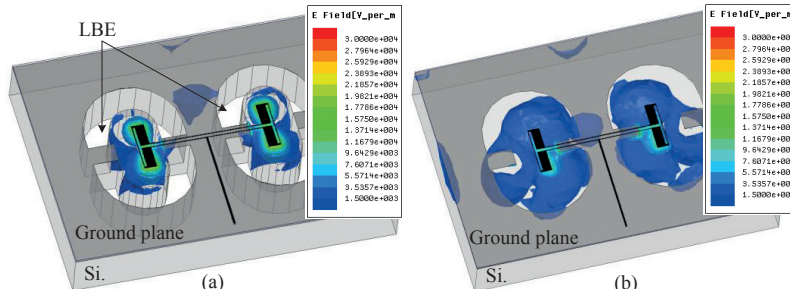
Figure 4.23: Simulated magnitude of the E-field in the silicon at 110 GHz: (a) with LBE process, (b) without LBE process. (The field is plotted in the same color scale.)

µm, which is optimized by taking into account both the performance and chip area considerations, can limit the propagation of the surface waves and reduce the loss. Figure 4.23 shows the simulated magnitude of the E-field in the silicon at 110 GHz for the same antenna with and without LBE, respectively. We can see that most of the E-field is well confined within the silicon islands for the antenna with LBE, while the E-field spreads out as substrate waves for the antenna without LBE. The size and shape of the silicon islands are optimized carefully so that the loss is limited, and the spurious radiation is constructively added to the main radiation. The ends of the silicon islands were optimized to be rounded with a radius of r_{d1}=175 µm. In this way the distance from the slot

center at the end of the folded dipole to the truncated rounded edge of the silicon island is the same. Since the edge of the silicon islands is far away from the dipole radiators, we can expect that this design is much more immune to the over-etching effects of the LBE process. This antenna takes a chip area of $1790 \times 1130 \ \mu m^2$ including the air trenches. This structure was applied for an international patent, and it is pending [25].

The photograph of the fabricated prototype is shown in Figure 4.24. The measurement method for the double folded dipole antenna is the same as that for the patch antenna, and it was also characterized both on-wafer at IHP and on-board at KIT. The on-wafer and on-board measurements as well as the simulation of S11 of the antenna are plotted together in Figure 4.25. They agree with each other. The over-etching effects and the adhesive were not included in the simulation. 6 samples were measured on-wafer, and their resonant frequency is identical at about 111 GHz, indicating that this antenna design is more immune to the fabrication tolerances. The measured –10 dB impedance bandwidth is about 103–126 GHz. The measured and simulated gain is shown in Figure 4.26. They have very good agreement in the band of 120–135 GHz, although there is up to 3 dB difference in the 110–120 GHz band probably due to the interference caused by the probe [7] and measurement setup. The measured 3-dB gain bandwidth is from 110 GHz to 135 GHz with a peak value of about 6 dBi, covering the ISM band of 122 GHz. The simulated radiation efficiency is about 54% at 122 GHz. The simulated and measured normalized radiation patterns at 122 GHz are shown in Figure 4.27. They agree with each other with 3-dB beamwidth of 44° in E-plane (xz-plane) and 50° in H-plane (yz-plane), respectively. Table 5.1 in chapter 5 presents a comparison of the state-of-the-art on-chip antennas in low-resistivity silicon technologies.
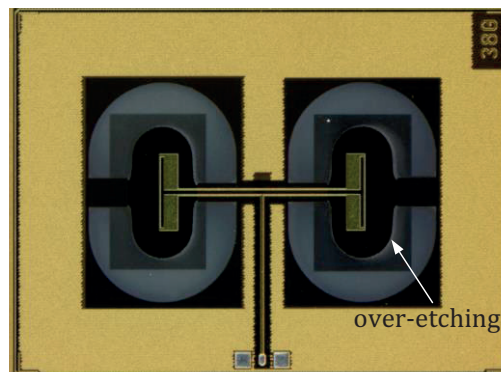
Figure 4.24: Fabricated prototype of the double folded dipole antenna (chip size: 2.5 × 1.85 mm².)
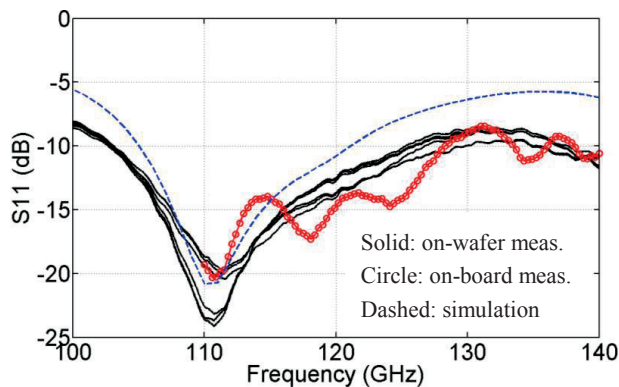
Figure 4.25: On-wafer (6 samples) and on-board measurements as well as the simulation of S11 of the double folded dipole antenna.
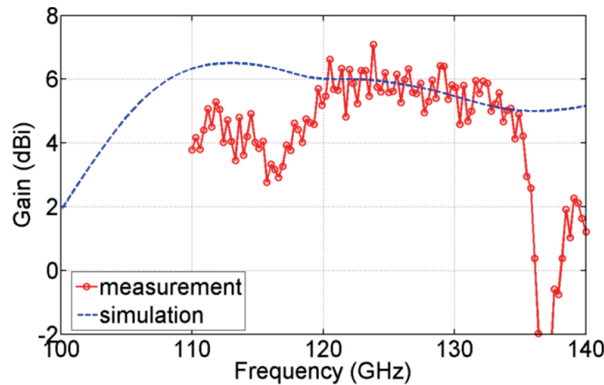
Figure 4.26: Measured and simulated gain of the double folded dipole antenna.
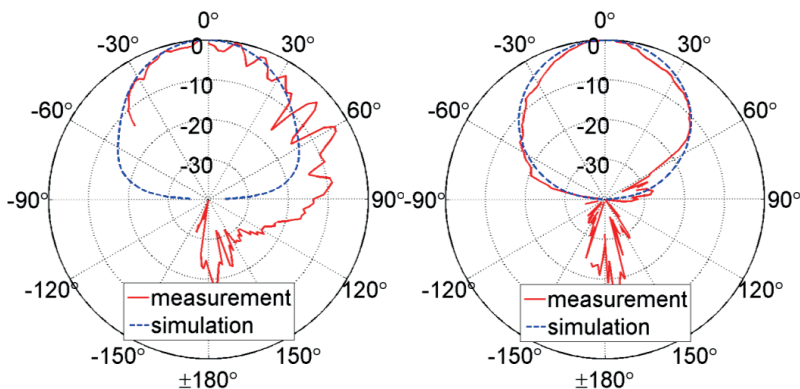
Figure 4.27: Measured and simulated normalized radiation patterns at 122 GHz of the double folded dipole antenna in (left) E-plane (xz-plane), and (right) H-plane (yz-plane). Unit in dB.

4.5   Conclusions

Several on-chip antenna designs have been presented and discussed based on both simulated and measured results. The discussions are not only limited to the radiation performance, but also cover the practical considerations of their mechanical stability, form factor, and fabrication tolerance. The presented antennas can give a peak gain of 6–8.4 dBi with radiation efficiency of more than 50% by applying the LBE process [19]–[21] [26], which is available in all IHP's technologies as well as other semiconductor technologies. The antennas with air cavity under the radiator have higher gain and wider bandwidth, while the antennas with air trenches around the radiator offer smaller form factor and better mechanical stability. To the best of my knowledge, the achieved gain of 7.5–8.4 dBi in the band of 124–134 GHz for the 130 GHz on-chip antenna is the highest reported result for planar on-chip antennas in low-resistivity silicon technologies to date. The double folded dipole on-chip antenna with surrounded air trenches was applied for an international patent, and it is pending [25]. There are antenna designs that can be used for 122 GHz and 245 GHz ISM band applications. The 245 GHz transmitter and receiver chip with integrated on-chip antenna have been demonstrated. The gain of the antenna was estimated to be 6–8 dBi in the band of 244–251 GHz in the demonstrator so that an EIRP of 7–8 dBm was achieved for the transmitter [19], which is the highest reported EIRP at 245 GHz for a SiGe transmitter with a single on-chip antenna to date. The receiver has the highest reported integration level for any 245 GHz SiGe receiver [20]. A 245 GHz 4-channel-transmitter array with integrated antenna array was also realized. It offers 11 dB higher EIRP than a single TX by achieving spatial power combining in this higher band of mm-Wave range [22], where the output power of the circuit is limited and the free-space loss is high.

References

[1]   Y. P. Zhang, M. Sun, and L. H. Guo, "On-chip antennas for 60-GHz radios in silicon technology," *Electron Devices, IEEE Transactions on*, vol. 52, no. 7, pp. 1664-1668, Jul. 2005.

[2]   S. –S. Hsu, K. –C. Wei, C. –Y. Hsu, and H. –R. Chuang, "A 60-GHz millimeter-wave CPW-fed Yagi antenna fabricated by using 0.18-µm CMOS technology," *Electron Device Letters, IEEE*, vol. 29, no. 6, pp. 625-627, Jun. 2008.

[3]   M. J. Edwards, and G. M. Rebeiz, "High-efficiency silicon RFIC millimeter-wave elliptical slot-antenna with a quartz lens," *Antennas and Propagation, 2011 IEEE International Symposium on*, pp. 899-902, Jul. 2011.

[4]   P. –J. Guo, and H. –R. Chuang, "A 60-GHz millimeter-wave CMOS RFIC-on-chip meander-line planar inverted-F antenna for WPAN applica-

tions," *Antennas and Propagation Society International Symposium*, *AP-S 2008. IEEE*, pp. 1-4, Jul. 2008.

[5]   X. –Y. Bao, Y. –X. Guo, and Y. –Z. Xiong, "60-GHz AMC-based circularly polarized on-chip antenna using standard 0.18-µm CMOS technology," *Antennas and Propagation*, *IEEE Transactions on*, vol. 60, no. 5, pp. 2234-2241, May. 2012.

[6]   F. Gutierrez, S. Agarwal, K. Parrish, and T. S. Rappaport, "On-chip integrated antenna structures in CMOS for 60 GHz WPAN systems," *Selected Areas in Communications*, *IEEE Journal on*, vol. 27, no. 8, pp. 1367-1378, Oct. 2009.

[7]   S. Pan, L. Gilreath, P. Heydari, and F. Capolino, "Investigation of a wideband BiCMOS fully on-chip W-band bowtie slot antenna," *Antennas and Wireless Propagation Letters*, *IEEE*, vol. 12, pp. 706-709, May 2013.

[8]   K. T. Chan *et al.*, "Integrated antennas on Si with over 100 GHz performance, fabricated using an optimized proton implantation process," *Microwave and Wireless Components Letters*, *IEEE*, vol. 13, no. 11, pp. 487-489, Nov. 2009.

[9]   J. Hasch, U. Wostradowski, S. Gaiser, and T. Hanse, "77 GHz radar transceiver with dual integrated antenna elements," *German Microwave Conference*, *2010*, pp. 280-283, Mar. 2010.

[10] I. Sarkas, J. Hasch, A. Balteanu, and S. P. Voinigescu, "A fundamental frequency 120-GHz SiGe BiCMOS distance sensor with integrated antenna," *Microwave Theory and Techniques*, *IEEE Transactions on*, vol. 60, no. 3, pp. 795-812, Mar. 2012.

[11] Y. –C. Ou, and G. M. Rebeiz, "On-chip slot-ring and high-gain horn antennas for millimeter-wave wafer-scale silicon systems," *Microwave Theory and Techniques*, *IEEE Transactions on*, vol. 59, no. 8, pp. 1963-1972, Aug. 2011.

[12] D. Hou *et al.*, "130-GHz on-chip meander slot antennas with stacked dielectric resonators in standard CMOS technology," *Antennas and Propagation*, *IEEE Transactions on*, vol. 60, no. 9, pp. 4102-4109, Sep. 2012.

[13] E. Ojefors *et al.*, "Micromachined inverted F antenna for integration on low resistivity silicon substrates," *Microwave and Wireless Components Letters*, *IEEE*, vol. 15, no. 10, pp. 627-629, Oct. 2005.

[14] V. K. Singh, "Ka-band micromachined microstrip patch antenna," *Microwaves, Antennas & Propagation*, *IET*, vol. 4, no. 3, pp. 316-323, Mar. 2010.

[15] http://www.ihp-microelectronics.com/en/services/mpw-prototyping/sigec-bicmos-technologies.html

[16] I. Papapolymerou, R. F. Drayton, and L. P. B. Katehi, "Micromachined patch antennas," *Antennas and Propagation*, *IEEE Transactions on*, vol. 46, no. 2, pp. 275-283, Feb. 1998.

[17] E. Ojefors *et al.*, "Compact micromachined dipole antenna for 24 GHz differential SiGe integrated circuits," *Microwave Conference*, *2004*, *34th European*, vol. 2, 1081-1084, Oct. 2004.

[18] E. Ojefors *et al.*, "Micromachined loop antennas on low resistivity silicon substrates," *Antennas and Propagation*, *IEEE Transactions on*, vol. 54, no. 12, pp. 3593-3601, Dec. 2006.

[19] K. Schmalz *et al.*, "245 GHz SiGe transmitter with integrated antenna and external PLL," *Microwave Symposium Digest (IMS)*, *2013 IEEE MTT-S International*, pp. 1-3, Jun. 2013.

[20] K. Schmalz *et al.*, "Subharmonic 245 GHz SiGe receiver with antenna," *Microwave Integrated Circuits Conference (EuMIC)*, *2013 European*, pp. 121-124, Oct. 2013.

[21] K. Schmalz *et al.*, "Tunable 245 GHz transmitter and receiver in SiGe technology for gas spectroscopy," *Electronics Letters*, vol. 50, no. 12, pp. 881-882, Jun. 2014.

[22] K. Schmalz, J. Borngräber, W. Debski, M. Elkhouly, R. Wang, P. Neumaier, and H. Hübers, "245 GHz SiGe transmitter array for gas spectroscopy," *2014 IEEE Compound Semiconductor IC Symposium*, pp.1-4, Oct. 2014.

[23] K. Li, C. H. Cheng, T. Matsui, and M. Izutsu, "Coplanar patch antennas: principle, simulation and experiment," *Antennas and Propagation Society International Symposium*, *2001 IEEE*, pp. 402-405, Jul. 2001.

[24] K. F. Tong, K. Li, T. Matsui, and M. Izutsu, "Broad-band double-layered coplanar patch antennas with adjustable CPW feeding structure," *Antennas and Propagation*, *IEEE Transactions on*, vol. 52, no. 11, pp. 3153-3156, Nov. 2004.

[25] R. Wang, Y. Sun, M. Kaynak, and J. C. Scheytt, "Chip-Antenne, Elektronisches Bauelement und Herstellungsverfahren dafür," *International Patent*, *PCT/EP2013/077951*, *2013*, pending.

[26] R. Wang, Y. Sun, M. Kaynak, S. Beer, and J. C. Scheytt, "A micromachined double-dipole antenna for 122-140 GHz applications based on a SiGe BiCMOS technology," *Microwave Symposium Digest (MTT)*, *2012 IEEE MTT-S International*, pp. 1-3, Jun. 2012.

5 Antenna Designs by Applying Wafer-Level Integration Technology

The thin-film multilayer multichip module with deposited interconnects (MCM-D) technology has been developed for many years, which is fabricated by a sequential deposition of conductors, and insulating layers, usually polyimide or Benzocyclobutene (BCB), on a ceramic, silicon, metal or laminate substrate carrier [1]. The BCB based MCM-D technology has been employed for many high performance RF module and antenna designs, because the BCB has low losses, low mechanical stress, and better planarization [2]–[7]. The SiGe BiCMOS process in IHP offers the possibility to realize all components for millimeter-wave transceivers on a single chip with fairly good electrical performance. This chapter will present 122 GHz patch antenna designs based on BCB above IHP's SiGe BiCMOS wafer process for system-on-chip (SoC) applications. The patch antenna has a ground plane which can isolate the radiator from the lossy silicon. However, as discussed in previous chapters the maximum separation of the metal layers offered by silicon technology is too small to design an antenna with acceptable efficiency. In the presented designs two BCB layers as well as two copper layers are deposited on the wafer, which can increase the thickness of the substrate for the patch antenna, thus improving its radiation efficiency and offering another choice for on-chip antenna implementation. The antenna and the circuits can be interconnected by on-chip interconnects with low parasitics and losses. A measured gain of 3.4 dBi at 122.5 GHz with a simulated efficiency of about 50% has been achieved for the presented antennas, which is sufficient for short range applications. At the beginning of this chapter the technology will be briefly introduced, and then the antenna design and measurement as well as the interconnects characterization are presented and discussed.

5.1   Technology Overview

Figure 5.1 shows the schematic drawing and the scanning electron microscope (SEM) photograph of the cross-section of the technology. The IHP's 0.25 μm BiCMOS wafer has been finalized without any change from the original process flow, having the pad opening as the last step. After that the above-wafer process has been implemented. Two layers of BCB (12 μm for each layer with ϵ_r=2.7 and tanδ=0.002) were spin-coated onto the wafer, and the thick copper layers were realized by using electroplating. All metal layers, including the 5 aluminum layers in the BEOL process of the silicon technology and the 2 copper layers in the above-wafer process, can be interconnected by vias. The via connection (via1) between copper 1 and TM2 has a minimum pitch of 2 μm, which helps to prevent from using large pad areas. The via between copper 1
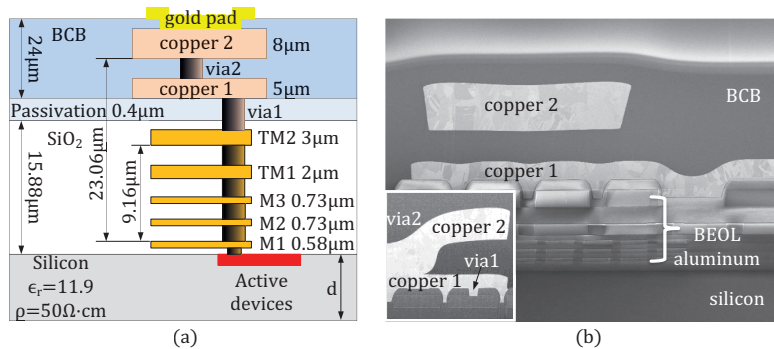
Figure 5.1: (a) Schematic drawing, and (b) the scanning electron microscope (SEM) photograph of the cross-section of the technology.

and copper 2 (via2) has relatively big minimum feature size due to the structuring limitations of BCB material. The above-wafer process was finalized by sputtering/structuring the gold layer on the opening pad in order to have a good contact.

5.2   122 GHz Antenna Design

Two half-wavelength patch antennas were designed and manufactured for 122 GHz applications. They are fed by different feeding methods, i.e. microstrip transmission line direct feed (design A) and proximity-coupled feed (design B). As it will be shown later that the two antennas have very similar performance, and the two feeding methods can be combined to use when more antenna elements are required on one chip that routing the feed lines in the same metal layer arises a problem. An infinitely large reflector under the chip is assumed in the simulations for both designs to represent the relatively large ground plane or heat sink of a package.

A. Patch Antenna with Microstrip Transmission Line Direct Feed (design A)

Design A is shown in Figure 5.2 (a). The patch radiator is realized in the thick copper 2 layer as well as the microstrip feeding line, while the ground plane is formed in M1 layer. The microstrip feeding line has a characteristic impedance of 50 Ω, and an inset cut is introduced to the patch to optimize the position of the feeding point, achieving a good impedance matching. The distance between the radiator and the ground plane is about 23.06 μm which corresponds to 0.015 wavelength at 122 GHz in BCB or 0.019 wavelength in silicon dioxide. This distance is more than twice as much as the separation between the top aluminum layer (TM2) and the bottom aluminum layer (M1) in the BEOL of the BiCMOS process, which is only 9.16 μm.

The chip is usually small in size and so is the on-chip ground plane of the antenna. For instance, it is 2000 μm × 2200 μm in this design which is smaller than $\lambda_0 \times \lambda_0$, where λ_0=2449 μm is the wavelength in free-space at 122.5 GHz. The field of patch antennas diffracts on the edges of the chip and finite ground plane, and the diffracted field superposes to the total radiation patterns [8]–[11]. Therefore, a change in the size of the chip or on-chip ground plane will influence the radiation performance of the antenna. Furthermore, part of the radiated energy will be reflected by the ground plane of the package, i.e. it is like a reflector of the on-chip antenna. The height of the antenna above the reflector, which is determined by the thickness of the silicon d, will affect the antenna's radiation performance, too. Figure 5.3 (a) shows the simulated antenna gain and efficiency at 122.5 GHz for different antenna's height with two chip and on-chip ground plane sizes, 2000×2200 μm^2 and 3000×3000 μm^2. It can be observed that the antenna with different chip size gives different gain (up to 1.5 dB of difference for the silicon thickness of 750 μm), but with lower available chip height (d=150~650 μm) the difference is within 1 dB. It indicates that the finite size of the chip and on-chip ground plane should be included in the design. The influence of the chip height is more obvious for the antenna with the chip size of 3000×3000 μm^2, whose gain for d=450 μm is about 2 dB higher than that for d=750 μm while the radiation efficiency is almost constantly 50%. Figure 5.3 (b) compares the radiation patterns for the two chip heights. Apparently, the radiation patterns for the case with higher gain, especially in the E-plane, have narrower beamwidth than that with lower gain, so their efficiency is almost the same. The original thickness of the wafer is 750 μm, but it can be thinned down to the desired thickness according to the applications.
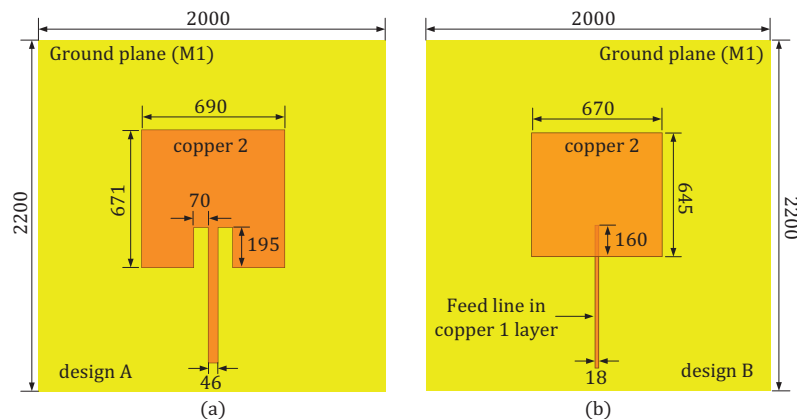
Figure 5.2: Patch antenna designs: (a) with microstrip direct feed, (b) with proximity-coupled feed. Unit: μm.
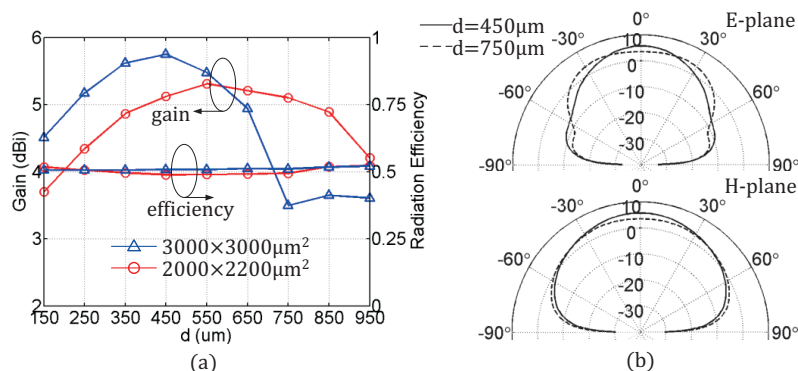
Figure 5.3: (a) Simulated antenna gain and efficiency at 122.5 GHz for different antenna's height with two chip and on-chip ground plane sizes, 2000 × 2200 μm^2 and 3000 × 3000 μm^2; (b) Simulated radiation patterns (in dBi) at 122.5 GHz with chip size of 3000 × 3000 μm^2 for d=450 μm and d=750 μm.

B. Patch Antenna with Proximity-Coupled Feed (design B)

Figure 5.2 (b) shows the patch antenna design with proximity-coupled feed. The main difference from design A is that the 50 Ω feeding transmission line is designed in copper 1 layer instead of copper 2 layer. It feeds the radiator by field coupling rather than physical contacting. A good impedance matching can be achieved by tuning the insertion length (160 μm in this design) of the feeding line. The size of the patch was also optimized accordingly. It is shown later that this antenna has similar radiation performance to that of design A.

5.3   Prototype Measurement

The photographs of the fabricated antenna prototypes are shown in Figure 5.4. The size of the chip and the on-chip ground plane is designed to be 2000 × 2200 μm^2, and the wafer thickness is kept as its original value of 750 μm. The antennas were measured with CPW to microstrip transitions by microwave probe with 100 μm pitch. The antenna chip is glued on the copper plane of PCB for the radiation measurement.

5.3.1   Transition Structure and Interconnect Characterization

The transition structures for antenna measurement as well as the interconnects among metal layers are illustrated in Figure 5.5. The copper 2 layer was connected to the copper 1 layer by a big via. The copper plating process does not support stacked vias, so the via connection between copper 1 layer and TM2 layer of the BEOL has to be offset from the via between the copper layers.

Standard stacked vias are then used to interconnect the aluminum metal layers in the BEOL, i.e. TM2–M1.

The transitions with interconnects are measured in a back-to-back configuration, as shown in Figure 5.6. Two identical transitions are connected by microstrip lines with 50 Ω characteristic impedance, which are the same as that used for the antennas. A half of the insertion loss will be calibrated out from the measured gain of the antenna to estimate the actual gain. The S11 is below -18 dB in 90–140 GHz for both structures, which indicates that the transitions are well matched to 50 Ω, and will introduce little impedance mismatch to the antenna. The insertion loss (S21) is increasing as the frequency goes up to higher band. The loss of design A, including two transitions and a 600 µm-long transmission line, is less than 1 dB. Design B has a little higher loss than that in design A, because it contains 2 more vias connection, and the 50 Ω transmission line in copper 1 layer is narrower in width. From the measurement we can
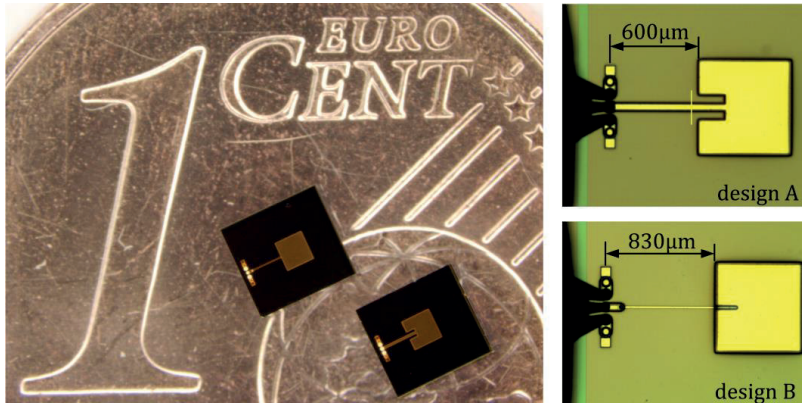

Figure 5.4: Photographs of the fabricated antenna prototypes.
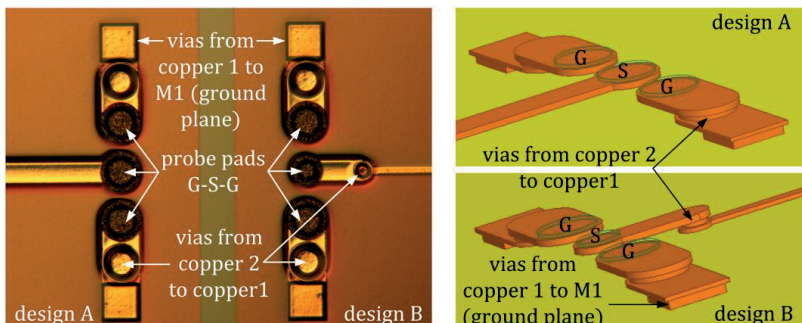

Figure 5.5: (Left) Photograph of the CPW to microstrip line transition; (Right) Schematic drawing of the CPW to microstrip transition. (The stacked vias in the BEOL and vias between copper 1 and TM2 are represented together by a square via, i.e. vias from copper 1 to M1.)
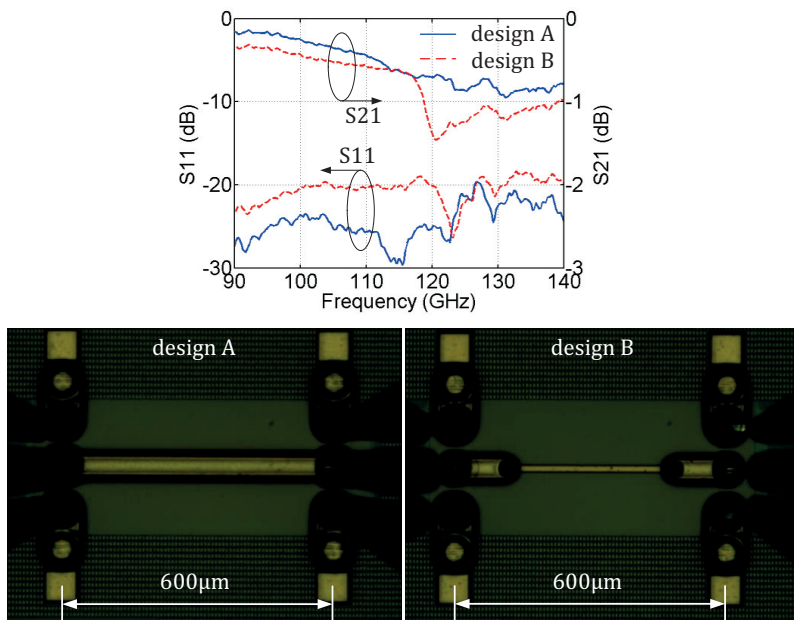
Figure 5.6: The measured S-parameter (top), and the photographs (bottom) of the back-to-back transition characterization structures.

see that the interconnects among metal layers can perform very well with low parasitic effects and low-loss.

5.3.2   Antenna Measurement

The simulated and measured S11 of the two antenna designs are shown in Figure 5.7. The antennas resonate at 122 GHz, which is 0.5 GHz or 0.4% lower than 122.5 GHz in the simulation for both designs. 10 samples of design A and 6 samples of design B were measured. The measurements have good repeatability. The measured -10 dB impedance bandwidth is about 2 GHz (121–123 GHz) for design A, covering the ISM band of 122–123 GHz. The measured -10 dB impedance bandwidth for design B is about 1.5 GHz, from 121.2–122.7 GHz. It can be expected that by depositing one more BCB layer as well as copper layer the bandwidth can be enlarged.

The simulated and measured normalized radiation patterns in E- and H-plane are compared in Figure 5.8 and 5.9 for design A and design B, respectively. The radiation patterns are very similar for the two designs. The measured E-plane has some ripples, which are caused by reflections and spurious radiations from the waveguide probe at the measurement setup. The simulated 3-dB beamwidth is 56°. The simulation and measurement agree with each other in H-plane. The measured 3-dB beamwidth is also 56°.

The simulated gain and calibrated measured gain of the antennas are shown in Figure 5.10. The calibrated measured gain is obtained by subtracting a half of the insertion loss of the transition calibration structures (Figure 5.6) from the directly measured gain. The shape of the simulated and measured gain curves have good agreement. The calibrated measured gain is about 3.4 dBi at 122.5 GHz for both designs, while the simulated gain is about 5.1 dBi with a radiation efficiency of 50%. The measured 3-dB gain bandwidth is 120.5–125.5 GHz for design A, and 120–124 GHz for design B, covering the 122 GHz ISM band. The discrepancy between the simulated and measured gain can be from several factors. For instance, the radiation and reflection of the waveguide probe in the vicinity of the antenna distorts the E-plane considerably in the measurement, causing many ripples and high magnitude side lobes (Figure 5.8 and 5.9). This can lower the gain in the broadside direction. The manufacture tolerance, for example the dicing of the chip was not intended to be well controlled so that the size of the chip is larger than that in the design, could also lower the gain slightly (Figure 5.3). Table 5.1 presents a comparison of the state-of-the-art on-chip antennas in low-resistivity silicon technologies.
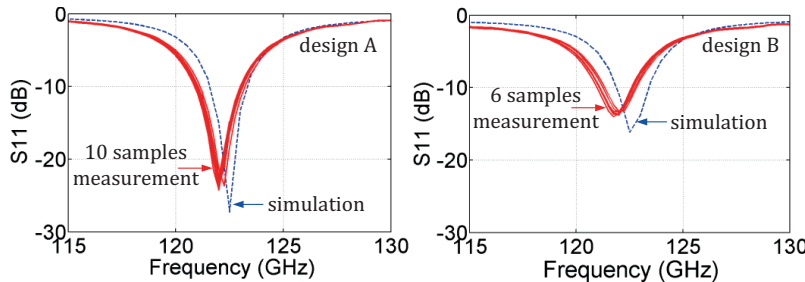
Figure 5.7: Simulated and measured S11 of the antenna designs.
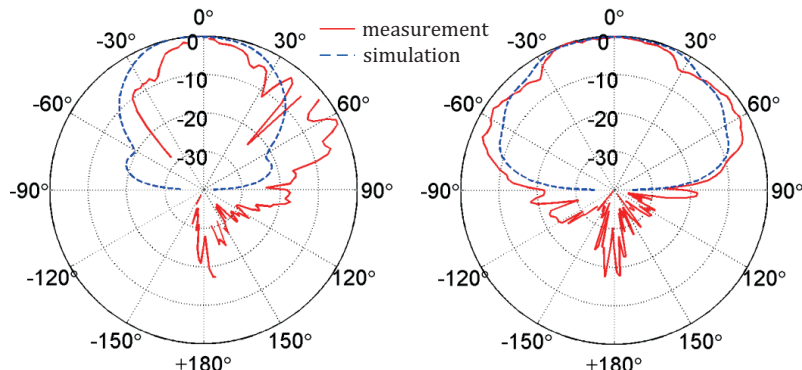
Figure 5.8: Simulated and measured normalized radiation patterns in E- (left) and H-plane (right) of design A at 122.5 GHz. Unit in dB.
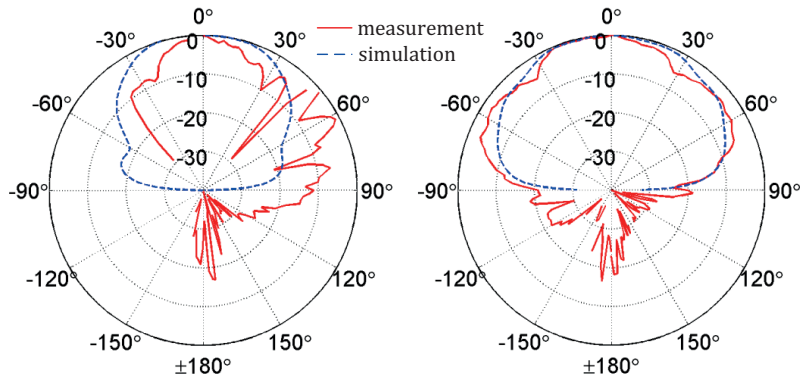
Figure 5.9: Simulated and measured normalized radiation patterns in E- (left) and H-plane (right) of design B at 122.5 GHz. Unit in dB.
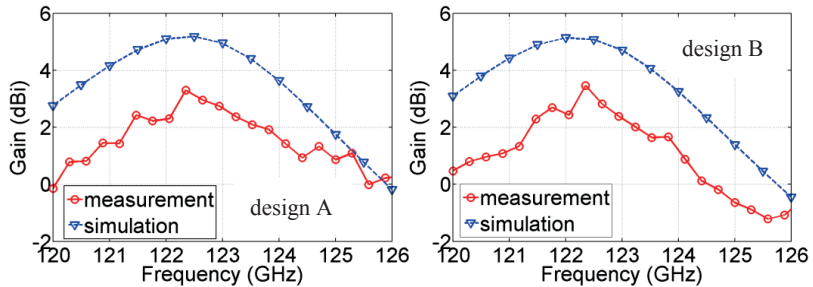
Figure 5.10: Simulated and measured gain of the antenna designs.

Table 5.1: Comparison of On-Chip Antennas in Low-Resistivity Silicon Tech.

Category	Process	Architecture	-10dB BW(GHz)	f_0 (GHz)	Gain (dBi)	Effi. (%)	Mecha. Stability	Ref.
Ordinary on-silicon antenna	BEOL CMOS	Inverted-F	55–67.5	61	-19	3.5	High	[12]
	0.18µm CMOS	Yagi	55–65	60	-10.6	10		[13]
	0.13µm CMOS	Slot-ring	87.5–90.5	89	-5.7	7		[14]
	0.18µm CMOS	Inverted-F	57–64	60	-15.7	10		[15]
	0.18µm CMOS	Loop	34–105	65	-4.4	NA		[16]
	0.18µm BiCMOS	*Bowtie slot	70–110	94	0–1	18		[17]

Table 5.1: Comparison of On-Chip Antennas in Low-Resistivity Silicon Tech.
(Continue)

Category	Process	Architecture	-10dB BW(GHz)	f_0 (GHz)	Gain (dBi)	Effi. (%)	Mecha. Stability	Ref.
Superstrate and DRA antennas on IC	0.13μm BiCMOS	Slot-ring	87–97	94	2	50–60	High	[18]
	0.13μm BiCMOS	Patch	NA	122	6	50		[19]
	0.18μm BiCMOS	**DRA	123–137	130	4.7	43		[20]
On-chip antennas LBE under radiators	SiGe	Meander dipole	NA	24.1	0.7	NA	Low	[21]
	BiCMOS	Inverted-F	22.5–25.5	24.1	-0.7	56		[22]
	Silicon	Slot-loop	NA	29.5	1.5	70		[23]
	Silicon	Wire-loop	NA	24	1	50		[23]
	0.25μm BiCMOS	Folded dipole	127–170	130	8	60		Thesis work 1
	0.13μm BiCMOS	Folded dipole	240–260	245	6–8	75		Thesis work 2
On-chip antennas LBE around radiators	0.13μm BiCMOS	Patch	>120–125	122	5–6	70–75	Medium	Thesis work 3
	0.13μm BiCMOS	Folded dipole	103–126	122	6	54		Thesis work 4
Wafer-level integrated on-chip antennas	BCB + BiCMOS	Patch	121–123	122.5	3.4	50	High	Thesis work 5
	BCB + BiCMOS	Patch	121.2–122.7	122.5	3.4	50		Thesis work 6

* The antenna is placed in the corner of the chip (position optimization).

** Two stacked dielectric resonators are placed on the IC.

5.4   Conclusions

Two patch antenna designs by using BCB as an additional dielectric above Si-Ge BiCMOS wafer have been demonstrated and discussed in this chapter. It enables the full integration of the mm-Wave transceiver and antenna on a single chip to achieve a system-on-chip. The critical parameters for on-chip an-

tenna designs, i.e. the chip size and chip thickness, were investigated. The two antenna designs with different feeding methods implemented in different metal layers have similar performance. It offers flexibility in routing the feed lines, which can be an advantage when more antenna elements are required within the very limited chip area.

The measured S11 is consistent for all measured 10 samples of design A and 6 samples of design B, which implies a tight fabrication tolerance of this post-wafer process. The interconnects among the metal layers were also experimentally verified, which have low parasitic effects and low-loss. The measured gain is 3.4 dBi at 122.5 GHz with simulated efficiency of about 50%, which is considerably higher than that of antennas realized on ordinary low-resistivity silicon. The 3-dB gain bandwidth covers the 122–123 GHz ISM band [24]. Only two layers of BCB and copper layers were deposited on the wafer for trial of the technology and verification of antenna integration method in this design. No additional processes like making metalized and polymer-filled cavity under the radiator were applied to keep the fabrication procedure simple and low-cost. It demonstrates a promising approach for short range applications for high volume products. It can be expected that with one more deposition layer the efficiency, gain, and bandwidth of antenna could be further increased. Moreover, the antenna and circuits can be integrated vertically on the same chip, thus saving the chip area and reducing the cost.

References

[1] D. Liu, B. Gaucher, U. Pfeiffer, and J. Grzyb, *Advanced Millimeter-wave Technologies: Antennas, Packaging and Circuits*, John Wiley & Sons Ltd., 2009.

[2] R. Carrillo-Ramirez, and R. W. Jackson, "A highly integrated millimeter-wave active antenna array using BCB and silicon substrate," *Microwave Theory and Techniques*, *IEEE Transactions on*, vol. 52, no. 6, pp. 1648-1653, Jun. 2004.

[3] S. B. Yeap *et al.*, "135GHz antenna array on BCB membrane backed by polymer-filled cavity," *Antennas and Propagation (EUCAP)*, *2012 6th European Conference on*, pp. 1337-1340, Mar. 2012.

[4] P. Abele *et al.*, "Wafer level integration of a 24 GHz differential SiGe-MMIC oscillator with a patch antenna using BCB as a dielectric layer," *Microwave Conference, 2003. 33rd European*, pp. 293-296, Oct. 2003.

[5] I. Ju *et al.*, "V-band beam-steering ASK transmitter and receiver using BCB-based system-on-package technology on silicon mother board," *Microwave and Wireless Components Letters, IEEE*, vol. 21, no. 11, pp. 619-621, Nov. 2011.

[6]   S. Hu, Y. –Z. Xiong, L. Wang, R. Li, and T. G. Lim, "A millimeter-wave wideband high-gain antenna and its 3D system-in-package solution in a TSV-compatible technology," *Electronic Components and Technology Conference, 2011 IEEE 61st*, pp. 869-872, May-Jun. 2011.

[7]   S. Seok, N. Rolland, and P. –A. Rolland, "A 60 GHz quarter-wave patch antenna based on BCB polymer," *Antennas and Propagation Society International Symposium, 2008*, pp. 1-4, Jul. 2008.

[8]   P. Vaudon, T. Aubreton, P. Dufrane, and B. Jecko, "Influence of the ground plane structure on the radiation of microstrip antennas," *annals of telecommunications*, vol. 48, no. 5-6, pp. 319-329, May 1993.

[9]   J. A. Aas, and K. Jakobsen, "Radiation patterns of rectangular microstrip antennas on finite ground planes," *Microwave Conference, 1982. 12th European*, pp. 384-389, Sep. 1982.

[10] S. A. Bokhari, J. R. mosig, and F. E. Gardiol, "Hybrid approach to compute radiation pattern of finite microstrip antennas," *Electronics Letters*, vol. 27, no. 22, pp. 2091-2093, Oct. 1991.

[11] J. Huang, "The finite ground plane effect on the microstrip antenna radiation patterns," *Antennas and Propagation, IEEE Transactions on*, vol. 31, no. 4, pp. 649-653, Jul. 1983.

[12] Y. P. Zhang, M. Sun, and L. H. Guo, "On-chip antennas for 60-GHz radios in silicon technology," *Electron Devices, IEEE Transactions on*, vol. 52, no. 7, pp. 1664-1668, Jul. 2005.

[13] S. –S. Hsu, K. –C. Wei, C. –Y. Hsu, and H. –R. Chuang, "A 60-GHz millimeter-wave CPW-fed Yagi antenna fabricated by using 0.18-µm CMOS technology," *Electron Device Letters, IEEE*, vol. 29, no. 6, pp. 625-627, Jun. 2008.

[14] M. J. Edwards, and G. M. Rebeiz, "High-efficiency silicon RFIC millimeter-wave elliptical slot-antenna with a quartz lens," *Antennas and Propagation, 2011 IEEE International Symposium on*, pp. 899-902, Jul. 2011.

[15] P. –J. Guo, and H. –R. Chuang, "A 60-GHz millimeter-wave CMOS RFIC-on-chip meander-line planar inverted-F antenna for WPAN applications," *Antennas and Propagation Society International Symposium, AP-S 2008. IEEE*, pp. 1-4, Jul. 2008.

[16] X. –Y. Bao, Y. –X. Guo, and Y. –Z. Xiong, "60-GHz AMC-based circularly polarized on-chip antenna using standard 0.18-µm CMOS technology," *Antennas and Propagation, IEEE Transactions on*, vol. 60, no. 5, pp. 2234-2241, May 2012.

[17] S. Pan, L. Gilreath, P. Heydari, and F. Capolino, "Investigation of a wideband BiCMOS fully on-chip W-band bowtie slot antenna," *Antennas and Wireless Propagation Letters, IEEE*, vol. 12, pp. 706-709, May 2013.

[18] Y. –C. Ou, and G. M. Rebeiz, "On-chip slot-ring and high-gain horn antennas for millimeter-wave wafer-scale silicon systems," *Microwave The-*

ory and Techniques, *IEEE Transactions on*, vol. 59, no. 8, pp. 1963-1972, Aug. 2011.

[19] I. Sarkas, J. Hasch, A. Balteanu, and S. P. Voinigescu, "A fundamental frequency 120-GHz SiGe BiCMOS distance sensor with integrated antenna," *Microwave Theory and Techniques*, *IEEE Transactions on*, vol. 60, no. 3, pp. 795-812, Mar. 2012.

[20] D. Hou *et al.*, "130-GHz on-chip meander slot antennas with stacked dielectric resonators in standard CMOS technology," *Antennas and Propagation*, *IEEE Transactions on*, vol. 60, no. 9, pp. 4102-4109, Sep. 2012.

[21] E. Ojefors *et al.*, "Compact micromachined dipole antenna for 24 GHz differential SiGe integrated circuits," *Microwave Conference*, *2004*, *34th European*, vol. 2, 1081-1084, Oct. 2004.

[22] E. Ojefors *et al.*, "Micromachined inverted F antenna for integration on low resistivity silicon substrates," *Microwave and Wireless Components Letters*, *IEEE*, vol. 15, no. 10, pp. 627-629, Oct. 2005.

[23] E. Ojefors *et al.*, "Micromachined loop antennas on low resistivity silicon substrates," *Antennas and Propagation*, *IEEE Transactions on*, vol. 54, no. 12, pp. 3593-3601, Dec. 2006.

[24] R. Wang, Y. Sun, M. Kaynak, J. Borngräber, B. Göttel, S. Beer, and J. C. Scheytt, "122 GHz patch antenna designs by using BCB above SiGe BiCMOS wafer process for system-on-chip applications," *Personal Indoor and Mobile Radio Communications (PIMRC)*, *2013 IEEE 24th International Symposium on*, pp. 1392-1396, Sep. 2013.

6 Conclusions and Future Work

This thesis started with the introduction of fundamental antenna parameters with the emphasis on their effects in mm-Wave systems. The basic antenna models were theoretically studied, which offered insight into the operation principle of the presented antennas and the directions for optimization. Various substrate characterization methods were reviewed, and the excitation and propagation of substrate waves were investigated. The probe based antenna measurement setup and its special calibration procedure were illustrated. The state-of-the-art antenna integration and packaging methods were extensively reviewed and discussed regarding their advantages and limitations. A design flow and methodology for mm-Wave integrated planar antenna designs was proposed by taking all the aforementioned factors into account and condensing the design experience in this thesis work into a methodology.

A number of millimeter-wave integrated planar antenna designs have been investigated using different integration approaches and technologies, i.e. on-PCB, on-chip and in BCB above-wafer process. The designs target not only high performance, but also the practical considerations of low-cost, feasibility, better reliability, and good reproducibility. They cover the ISM bands of 60 GHz, 122 GHz, and 245 GHz with outstanding performance in low-cost fashions by using the appropriate integration method and sophisticated design.

Chapter 3 demonstrated the possibility and flexibility of designing integrated PCB antennas with good performance in a very low-cost fashion for 60 GHz applications. Three commercially available low-cost dielectrics were characterized, and one of them was selected for antenna designs. The mm-Wave interconnects of bond-wire and stud bumps for flip-chip interconnects were experimentally studied. A novel double-bonding structure for compensating the parasitic effects of bond-wire was proposed, and proven to have good repeatability, large bandwidth, and low-loss of 0.2–0.3 dB at 62 GHz per interconnect [1]. A differential bunny-ear antenna with end-fire radiation direction and a differential patch array antenna with broadside radiation direction have been designed, fabricated, and measured [2]. A 4-element differential linear patch phased array antenna was also designed to achieve beamforming function. Special attention has been paid to the design of the feeding networks of the phased array. The demonstrator with bunny-ear antenna achieved a data rate of 3.6 Gbit/s over a 15-meter distance [3] [4], which was the best reported analog front-end without beamforming function in silicon technology regarding both the data rate and transmission distance at the time of its publication [5]. The differential patch array antenna was also successfully demonstrated in a high data rate communication system with an integrated high-resolution ranging feature [6] [7].

Several on-chip antenna designs by applying LBE process in IHP's SiGe BiCMOS technology have been presented in chapter 4. The antennas have measured peak gains of 6–8.4 dBi with simulated efficiencies of 54–75% which are comparable to that of on-board or in-package antennas. To the best of my knowledge, the achieved gain of 7.5–8.4 dBi in the band of 124–134 GHz for the 130 GHz on-chip antenna [8] is the highest reported result for planar on-chip antennas in low-resistivity silicon technologies to date. Besides good radiation performance, efforts were made to achieve better mechanical stability, reduced form factor, and better immunity to fabrication tolerances. The double folded dipole on-chip antenna with surrounded air trenches was applied for an international patent, and it is pending [9]. The single-channel 245 GHz transmitter and single-channel receiver with integrated on-chip antenna were demonstrated [10]–[13]. An EIRP of 7–8 dBm was achieved for the transmitter, which is the highest reported value so far at 245 GHz for a SiGe transmitter with a single antenna [10]. The receiver has the highest reported integration level for any 245 GHz SiGe receiver [11]. A 245 GHz 4-channel-transmitter array with integrated antenna array was also realized to achieve spatial power combining [14]. It offers 11 dB higher EIRP than a single-channel TX in this higher band of mm-Wave range, where the output power of the circuit is limited and the free-space loss is high.

Chapter 5 presented patch antenna designs with microstrip direct feeding and proximity-coupled feeding by applying wafer-level integration technology. Two layers of BCB polymer as well as two thick copper layers were deposited onto the SiGe BiCMOS wafer. The antenna efficiency and gain were improved to 50 % and 3.4 dBi at 122.5 GHz [15], respectively, which are suitable for short range applications, demonstrating a promising approach to realize system-on-chip at low-cost for high volume products. The critical parameters for on-chip antenna designs with on-chip ground shielding, i.e. the chip size and chip thickness, were investigated. Many samples of the antennas were measured, and they show reproducible results which imply tight fabrication tolerance of this technology. The interconnects among the metal layers were also experimentally verified, which have low parasitic effects, and low loss. Table 5.1 in chapter 5 presents a comparison of the state-of-the-art on-chip antennas in low-resistivity silicon technologies.

From the presented results of the thesis it is feasible to realize high performance integrated planar antennas in the entire mm-Wave range and even beyond in a cost-effective fashion. There is overlapping in frequencies of different antenna integration approaches, e.g. the 122 GHz antenna were realized both on-chip and in BCB post-wafer process. The selection will depend on applications.

The future work could be the further miniaturization of the on-chip antennas to further reduce the cost.

References

[1]   R. Wang, Y. Sun, C. Wipf, and J. C. Scheytt, "An on-board differential patch array antenna and interconnects design for 60 GHz applications," *Microwaves, Communications, Antennas and Electronics Systems (COMCAS), 2011 IEEE International Conference on*, pp. 1-5, Nov. 2011.

[2]   R. Wang, Y. Sun, and J. C. Scheytt, "An on-board differential bunny-ear antenna design for 60 GHz applications," *German Microwave Conference, 2010*, pp. 9-12, Mar. 2010.

[3]   S. Glisic, K. Schmalz, F. Herzel, R. Wang, M. Elkhouly, Y. Sun, and J. C. Scheytt, "A fully integrated 60 GHz transmitter front-end in SiGe BiCMOS technology," *Silicon Monolithic Integrated Circuits in RF systems (SiRF), 2011 IEEE 11th Topical Meeting on*, pp. 149-152, Jan. 2011.

[4]   Y. Sun, K. Schmalz, S. Glisic, R. Wang, and J. C. Scheytt, "An integrated differential 60 GHz sliding-IF receiver in SiGe BiCMOS," *Computer Research and Development (ICCRD), 2011 3rd International Conference on*, vol. 3, pp. 297-300, Mar. 2011.

[5]   S. Glisic, J. C. Scheytt, Y. Sun, F. Herzel, R. Wang, K. Schmalz, M. Elkhouly, and C. S. Choi, "Fully integrated 60 GHz transceiver in SiGe BiCMOS, RF modules, and 3.6 Gbit/s OFDM data transmission," *International Journal of Microwave and Wireless Technologies*, vol. 3, special issue 02, pp. 139-145, Apr. 2011.

[6]   M. Ehrig, and M. Petri, "60 GHz broadband MAC system design for cable replacement in machine vision applications," *AEU-International Journal of Electronics and Communications*, vol. 67, no. 12, pp. 1118-1128, Dec. 2013.

[7]   M. Ehrig, M. Petri, V. Sark, J. Teran, and E. Grass, "Combined high-resolution ranging and high data rate wireless communication system in the 60 GHz band," *11th workshop on Positioning, Navigation and Communication 2014*, pp. 1-6, Mar. 2014.

[8]   R. Wang, Y. Sun, M. Kaynak, S. Beer, and J. C. Scheytt, "A micromachined double-dipole antenna for 122-140 GHz applications based on a SiGe BiCMOS technology," *Microwave Symposium Digest (MTT), 2012 IEEE MTT-S International*, pp. 1-3, Jun. 2012.

[9]   R. Wang, Y. Sun, M. Kaynak, and J. C. Scheytt, "Chip-Antenne, Elektronisches Bauelement und Herstellungsverfahren dafür," *International Patent, PCT/EP2013/077951, 2013*, pending.

[10] K. Schmalz, R. Wang, J. Borngräber, W. Debski, W. Winkler, and C. Meliani, "245 GHz SiGe transmitter with integrated antenna and external

PLL," *Microwave Symposium Digest (IMS)*, *2013 IEEE MTT-S International*, pp. 1-3, Jun. 2013.

[11] K. Schmalz, J. Borngräber, R. Wang, W. Debski, W. Winkler, and C. Meliani, "Subharmonic 245 GHz SiGe receiver with antenna," *Microwave Integrated Circuits Conference (EuMIC)*, *2013 European*, pp. 121-124, Oct. 2013.

[12] K. Schmalz *et al.*, "Tunable 245 GHz transmitter and receiver in SiGe technology for gas spectroscopy*," Electronics Letters*, vol. 50, no. 12, pp. 881-882, Jun. 2014.

[13] K. Schmalz, R. Wang, Y. Mao, W. Debski, H. Gulan, H. Hübers, P. Neumaier, and J. Borngräber, "245 GHz SiGe sensor system for gas spectroscopy," *European Microwave Conference 2014*, pp. 644-647, Oct. 2014.

[14] K. Schmalz, J. Borngräber, W. Debski, M. Elkhouly, R. Wang, P. Neumaier, and H. Hübers, "245 GHz SiGe transmitter array for gas spectroscopy," *2014 IEEE Compound Semiconductor IC Symposium*, pp. 1-4, Oct. 2014.

[15] R. Wang, Y. Sun, M. Kaynak, J. Borngräber, B. Göttel, S. Beer, and J. C. Scheytt, "122 GHz patch antenna designs by using BCB above SiGe BiCMOS wafer process for system-on-chip applications," *Personal Indoor and Mobile Radio Communications (PIMRC)*, *2013 IEEE 24th International Symposium on*, pp. 1392-1396, Sep. 2013.

Appendix A

General Solutions for TEM, TM, and TE Waves

The time-harmonic electric and magnetic fields with an $e^{j\omega t}$ (omitted in the expressions for simplicity) dependence in rectangular coordinates can be written as

$$\vec{E}(x,y,z) = \hat{x}E_x(x,y,z) + \hat{y}E_y(x,y,z) + \hat{z}E_z(x,y,z) \qquad (A.1a)$$

$$\vec{H}(x,y,z) = \hat{x}H_x(x,y,z) + \hat{y}H_y(x,y,z) + \hat{z}H_z(x,y,z) \qquad (A.1b)$$

Assuming that the wave is propagating along the $+z$ direction with a propagation constant β, (A.1) can then be written as

$$\vec{E}(x,y,z) = [\hat{x}e_x(x,y) + \hat{y}e_y(x,y) + \hat{z}e_z(x,y)]e^{-j\beta z} \qquad (A.2a)$$

$$\vec{H}(x,y,z) = [\hat{x}h_x(x,y) + \hat{y}h_y(x,y) + \hat{z}h_z(x,y)]e^{-j\beta z} \qquad (A.2b)$$

where e_x, e_y and h_x, h_y are the transverse electric and magnetic field components, while e_z and h_z are the longitudinal electric and magnetic field components. A wave propagating in $-z$ direction can be obtained by replacing the propagation constant β by $-\beta$. If the loss is present, $j\beta$ should be replaced by $\gamma = \alpha + j\beta$. When the wave is propagating in a source free region, Maxwell's equations are written as

$$\nabla \times \vec{E} = -j\omega\mu\vec{H} \qquad (A.3a)$$

$$\nabla \times \vec{H} = j\omega\epsilon\vec{E} \qquad (A.3b)$$

Taking the vector operation

$$\nabla \times \vec{E} = \hat{x}\left(\frac{\partial E_z}{\partial y} - \frac{\partial E_y}{\partial z}\right) + \hat{y}\left(\frac{\partial E_x}{\partial z} - \frac{\partial E_z}{\partial x}\right) + \hat{z}\left(\frac{\partial E_y}{\partial x} - \frac{\partial E_x}{\partial y}\right) = -j\omega\mu\vec{H} \qquad (A.4a)$$

$$\nabla \times \vec{H} = \hat{x}\left(\frac{\partial H_z}{\partial y} - \frac{\partial H_y}{\partial z}\right) + \hat{y}\left(\frac{\partial H_x}{\partial z} - \frac{\partial H_z}{\partial x}\right) + \hat{z}\left(\frac{\partial H_y}{\partial x} - \frac{\partial H_x}{\partial y}\right) = j\omega\epsilon\vec{E} \qquad (A.4b)$$

With an $e^{-j\beta z}$ dependence and matching the $\hat{x}, \hat{y}, \hat{z}$ component, (A.4) leads to

$$\frac{\partial E_z}{\partial y} + j\beta E_y = -j\omega\mu H_x \qquad (A.5a)$$

$$-j\beta E_x - \frac{\partial E_z}{\partial x} = -j\omega\mu H_y \qquad (A.5b)$$

$$\frac{\partial E_y}{\partial x} - \frac{\partial E_x}{\partial y} = -j\omega\mu H_z \qquad (A.5c)$$

$$\frac{\partial H_z}{\partial y} + j\beta H_y = j\omega\epsilon E_x \qquad (A.5d)$$

$$-j\beta H_x - \frac{\partial H_z}{\partial x} = j\omega\epsilon E_y \qquad (A.5e)$$

$$\frac{\partial H_y}{\partial x} - \frac{\partial H_x}{\partial y} = j\omega\epsilon E_z \tag{A.5f}$$

From (A.5) the transverse field components can be solved and expressed in terms of the longitudinal field components as

$$H_x = \frac{j}{k_c^2}\left(\omega\epsilon\frac{\partial E_z}{\partial y} - \beta\frac{\partial H_z}{\partial x}\right) \tag{A.6a}$$

$$H_y = \frac{-j}{k_c^2}\left(\omega\epsilon\frac{\partial E_z}{\partial x} + \beta\frac{\partial H_z}{\partial y}\right) \tag{A.6b}$$

$$E_x = \frac{-j}{k_c^2}\left(\beta\frac{\partial E_z}{\partial x} + \omega\mu\frac{\partial H_z}{\partial y}\right) \tag{A.6c}$$

$$E_y = \frac{j}{k_c^2}\left(-\beta\frac{\partial E_z}{\partial y} + \omega\mu\frac{\partial H_z}{\partial x}\right) \tag{A.6d}$$

where

$$k_c^2 = k^2 - \beta^2 \tag{A.7a}$$

$$k = \omega\sqrt{\mu\epsilon} \tag{A.7b}$$

is the cutoff wavenumber and the wavenumber in a material, respectively. Transverse electromagnetic (TEM) waves are defined by $E_z = H_z = 0$. In this case we must have $k_c^2 = 0$ ($k^2 = \beta^2$) in (A.6), otherwise the transverse fields are zero, too. Transverse magnetic (TM) waves are characterized by $E_z \neq 0$ and $H_z = 0$, while transverse electric (TE) waves are characterized by $E_z = 0$ and $H_z \neq 0$. The longitudinal fields of E_z for TM waves and H_z for TE waves as well as their cutoff wavenumbers k_c of various modes can be obtained by solving Helmholtz wave equation by applying specific boundary conditions. And afterwards, their transverse fields can be derived from (A.6).

Publications

[1] **R. Wang**, Y. Sun, M. Kaynak, and J. C. Scheytt, "Chip-Antenne, Elektronisches Bauelement und Herstellungsverfahren dafür," *International Patent*, *PCT/EP2013/077951*, *2013*, pending.

[2] **R. Wang**, Y. Sun, M. Kaynak, J. Borngräber, B. Göttel, S. Beer, and J. C. Scheytt, "122 GHz patch antenna designs by using BCB above SiGe BiCMOS wafer process for system-on-chip applications," *Personal Indoor and Mobile Radio Communications (PIMRC)*, *2013 IEEE 24th International Symposium on*, pp. 1392-1396, Sep. 2013.

[3] **R. Wang**, Y. Sun, M. Kaynak, S. Beer, and J. C. Scheytt, "A micromachined double-dipole antenna for 122-140 GHz applications based on a SiGe BiCMOS technology," *Microwave Symposium Digest (MTT)*, *2012 IEEE MTT-S International*, pp. 1-3, Jun. 2012.

[4] **R. Wang**, Y. Sun, C. Wipf, and J. C. Scheytt, "An on-board differential patch array antenna and interconnects design for 60 GHz applications," *Microwaves, Communications, Antennas and Electronics Systems (COMCAS)*, *2011 IEEE International Conference on*, pp. 1-5, Nov. 2011.

[5] **R. Wang**, Y. Sun, and J. C. Scheytt, "An on-board differential bunny-ear antenna design for 60 GHz applications," *German Microwave Conference*, *2010*, pp. 9-12, Mar. 2010.

[6] K. Schmalz, **R. Wang**, W. Debski, H. Gulan, J. Borngräber, P. Neumaier, and H. –W. Hübers, "245 GHz SiGe sensor system for gas spectroscopy," *International Journal of Microwave and Wireless Technologies*, doi: 10.1017/S1759078715000082, published online: Feb. 2015.

[7] K. Schmalz, J. Borngräber, W. Debski, P. Neumaier, **R. Wang**, and H. –W. Hübers, "Tunable 500 GHz transmitter array in SiGe technology for gas spectroscopy," *Electronics Letters*, vol. 51, no. 3, pp. 257-259, Feb. 2015.

[8] K. Schmalz, **R. Wang**, Y. Mao, W. Debski, H. Gulan, H. Hübers, P. Neumaier, and J. Borngräber, "245 GHz SiGe sensor system for gas spectroscopy," *European Microwave Conference 2014*, pp. 644-647, Oct. 2014.

[9] K. Schmalz, J. Borngräber, W. Debski, M. Elkhouly, **R. Wang**, P. Neumaier, and H. Hübers, "245 GHz SiGe transmitter array for gas spectroscopy," *2014 IEEE Compound Semiconductor IC Symposium*, pp. 1-4, Oct. 2014.

[10] K. Schmalz, **R. Wang**, J. Borngräber, W. Debski, W. Winkler, and C. Meliani, "245 GHz SiGe transmitter with integrated antenna and external PLL," *Microwave Symposium Digest (IMS)*, *2013 IEEE MTT-S International*, pp. 1-3, Jun. 2013.

[11] K. Schmalz, J. Borngräber, **R. Wang**, W. Debski, W. Winkler, and C. Meliani, "Subharmonic 245 GHz SiGe receiver with antenna," *Micro-*

wave Integrated Circuits Conference (EuMIC), 2013 European, pp. 121-124, Oct. 2013.

[12] J. C. Scheytt, Y. Sun, K. Schmalz, Y. Mao, **R. Wang**, W. Debski, and W. Winkler, "Towards mm-wave system-on-chip with integrated antennas for low-cost 122 and 245 GHz radar sensors," *Silicon Monolithic Integrated Circuits in RF Systems (SiRF)*, 2013 IEEE Topical Meeting on, pp. 246-248, Jan. 2013.

[13] J. C. Scheytt, Y. Sun, K. Schmalz, and **R. Wang**, "SiGe BiCMOS transceivers, antennas, and ultra-low-cost packaging for the ISM bands at 122 and 245 GHz," *Microwave Symposium Digest (MTT)*, 2012 IEEE MTT-S International, pp.1-3, Jun. 2012.

[14] S. Glisic, K. Schmalz, F. Herzel, **R. Wang**, M. Elkhouly, Y. Sun, and J. C. Scheytt, "A fully integrated 60 GHz transmitter front-end in SiGe BiCMOS technology," *Silicon Monolithic Integrated Circuits in RF systems (SiRF)*, 2011 IEEE 11th Topical Meeting on, pp. 149-152, Jan. 2011.

[15] Y. Sun, K. Schmalz, S. Glisic, **R. Wang**, and J. C. Scheytt, "An integrated differential 60 GHz sliding-IF receiver in SiGe BiCMOS," *Computer Research and Development (ICCRD)*, 2011 3rd International Conference on, vol. 3, pp. 297-300, Mar. 2011.

[16] S. Glisic, J. C. Scheytt, Y. Sun, Frank Herzel, **R. Wang**, K. Schmalz, M. Elkhouly, and C. S. Choi, "Fully integrated 60 GHz transceiver in SiGe BiCMOS, RF modules, and 3.6 Gbit/s OFDM data transmission," *International Journal of Microwave and Wireless Technologies*, vol. 3, special issue 02, pp. 139-145, Apr. 2011.

Das Heinz Nixdorf Institut –
Interdisziplinäres Forschungszentrum
für Informatik und Technik

Das Heinz Nixdorf Institut ist ein Forschungszentrum der Universität Paderborn. Es entstand 1987 aus der Initiative und mit Förderung von Heinz Nixdorf. Damit wollte er Ingenieurwissenschaften und Informatik zusammenführen, um wesentliche Impulse für neue Produkte und Dienstleistungen zu erzeugen. Dies schließt auch die Wechselwirkungen mit dem gesellschaftlichen Umfeld ein.

Die Forschungsarbeit orientiert sich an dem Programm „Dynamik, Mobilität, Vernetzung: Eine neue Schule des Entwurfs der technischen Systeme von morgen". In der Lehre engagiert sich das Heinz Nixdorf Institut in Studiengängen der Informatik, der Ingenieurwissenschaften und der Wirtschaftswissenschaften.

Heute wirken am Heinz Nixdorf Institut acht Professoren mit insgesamt 200 Mitarbeiterinnen und Mitarbeitern. Etwa ein Viertel der Forschungsprojekte der Universität Paderborn entfallen auf das Heinz Nixdorf Institut und pro Jahr promovieren hier etwa 30 Nachwuchswissenschaftlerinnen und Nachwuchswissenschaftler.

Heinz Nixdorf Institute –
Interdisciplinary Research Centre
for Computer Science and Technology

The Heinz Nixdorf Institute is a research centre within the University of Paderborn. It was founded in 1987 initiated and supported by Heinz Nixdorf. By doing so he wanted to create a symbiosis of computer science and engineering in order to provide critical impetus for new products and services. This includes interactions with the social environment.

Our research is aligned with the program "Dynamics, Mobility, Integration: Enroute to the technical systems of tomorrow." In training and education the Heinz Nixdorf Institute is involved in many programs of study at the University of Paderborn. The superior goal in education and training is to communicate competencies that are critical in tomorrows economy.

Today eight Professors and 200 researchers work at the Heinz Nixdorf Institute. The Heinz Nixdorf Institute accounts for approximately a quarter of the research projects of the University of Paderborn and per year approximately 30 young researchers receive a doctorate.

Zuletzt erschienene Bände der Verlagsschriftenreihe des Heinz Nixdorf Instituts

Bd. 308 KAHL, S.: Rahmenwerk für einen selbst-optimierenden Entwicklungsprozess fortschrittlicher mechatronischer Systeme. Dissertation, Fakultät für Maschinenbau, Universität Paderborn, HNI-Verlagsschriftenreihe, Band 308, Paderborn, 2013 – ISBN 978-3-942647-27-4

Bd. 309 WASSMANN, H.: Systematik zur Entwicklung von Visualisierungstechniken für die visuelle Analyse fortgeschrittener mechatronischer Systeme in VR-Anwendungen. Dissertation, Fakultät für Maschinenbau, Universität Paderborn, HNI-Verlagsschriftenreihe, Band 309, Paderborn, 2013 – ISBN 978-3-942647-28-1

Bd. 310 GAUSEMEIER, J.; RAMMIG, F.; SCHÄFER, W.; TRÄCHTLER, A. (Hrsg.): 9. Paderborner Workshop Entwurf mechatronischer Systeme. HNI-Verlagsschriftenreihe, Band 310, Paderborn, 2013 – ISBN 978-3-942647-29-8

Bd. 311 GAUSEMEIER, J.; GRAFE, M.; MEYER AUF DER HEIDE, F. (Hrsg.): 11. Paderborner Workshop Augmented & Virtual Reality in der Produktentstehung. HNI-Verlagsschriftenreihe, Band 311, Paderborn, 2013 – ISBN 978-3-942647-30-4

Bd. 312 BENSIEK, T.: Systematik zur reifegradbasierten Leistungsbewertung und -steigerung von Geschäftsprozessen im Mittelstand. Dissertation, Fakultät für Maschinenbau, Universität Paderborn, HNI-Verlagsschriftenreihe, Band 312, Paderborn, 2013 – ISBN 978-3-942647-31-1

Bd. 313 KOKOSCHKA, M.: Verfahren zur Konzipierung imitationsgeschützter Produkte und Produktionssysteme. Dissertation, Fakultät für Maschinenbau, Universität Paderborn, HNI-Verlagsschriftenreihe, Band 313, Paderborn, 2013 – ISBN 978-3-942647-32-8

Bd. 314 VON DETTEN, M.: Reengineering of Component-Based Software Systems in the Presence of Design Deficiencies. Dissertation, Fakultät für Elektrotechnik, Informatik und Mathematik, Universität Paderborn, HNI-Verlagsschriftenreihe, Band 314, Paderborn, 2013 – ISBN 978-3-942647-33-5

Bd. 315 MONTEALEGRE AGRAMONT, N. A.: Immunorepairing of Hardware Systems. Dissertation, Fakultät für Elektrotechnik, Informatik und Mathematik, Universität Paderborn, HNI-Verlagsschriftenreihe, Band 315, Paderborn, 2013 – ISBN 978-3-942647-34-2

Bd. 316 DANGELMAIER, W.; KLAAS, A.; LAROQUE, C.: Simulation in Produktion und Logistik 2013. HNI-Verlagsschriftenreihe, Band 316, Paderborn, 2013 – ISBN 978-3-942647-35-9

Bd. 317 PRIESTERJAHN, C.: Analyzing Self-healing Operations in Mechatronic Systems. Dissertation, Fakultät für Elektrotechnik, Informatik und Mathematik, Universität Paderborn, HNI-Verlagsschriftenreihe, Band 317, Paderborn, 2013 – ISBN 978-3-942647-36-6

Bd. 318 GAUSEMEIER, J. (Hrsg.): Vorausschau und Technologieplanung. 9. Symposium für Vorausschau und Technologieplanung, Heinz Nixdorf Institut, 5. und 6. Dezember 2013, Berlin-Brandenburgische Akademie der Wissenschaften, Berlin, HNI-Verlagsschriftenreihe, Band 318, Paderborn, 2013 – ISBN 978-3-942647-37-3

Bd. 319 GAUSEMEIER, S.: Ein Fahrerassistenzsystem zur prädiktiven Planung energie- und zeitoptimaler Geschwindigkeitsprofile mittels Mehrzieloptimierung. Dissertation, Fakultät für Maschinenbau, Universität Paderborn, HNI-Verlagsschriftenreihe, Band 319, Paderborn, 2013 – ISBN 978-3-942647-38-0

Bd. 320 GEISLER, J.: Selbstoptimierende Spurführung für ein neuartiges Schienenfahrzeug. Dissertation, Fakultät für Maschinenbau, Universität Paderborn, HNI-Verlagsschriftenreihe, Band 320, Paderborn, 2013 – ISBN 978-3-942647-39-7

Bd. 321 MÜNCH, E.: Selbstoptimierung verteilter mechatronischer Systeme auf Basis paretooptimaler Systemkonfigurationen. Dissertation, Fakultät für Maschinenbau, Universität Paderborn, HNI-Verlagsschriftenreihe, Band 321, Paderborn, 2014 – ISBN 978-3-942647-40-3

Bd. 322 RENKEN, H.: Acceleration of Material Flow Simulations - Using Model Coarsening by Token Sampling and Online Error Estimation and Accumulation Controlling. Dissertation, Fakultät für Wirtschaftswissenschaften, Universität Paderborn, HNI-Verlags-schriftenreihe, Band 322, Paderborn, 2014 – ISBN 978-3-942647-41-0

Zuletzt erschienene Bände der Verlagsschriftenreihe des Heinz Nixdorf Instituts

Bd. 323 KAGANOVA, E.: Robust solution to the CLSP and the DLSP with uncertain demand and online information base. Dissertation, Fakultät für Wirtschaftswissenschaften, Universität Paderborn, HNI-Verlags-schriftenreihe, Band 323, Paderborn, 2014 – ISBN 978-3-942647-42-7

Bd. 324 LEHNER, M.: Verfahren zur Entwicklung geschäftsmodell-orientierter Diversifikationsstrategien. Dissertation, Fakultät für Maschinenbau, Universität Paderborn, HNI-Verlagsschriftenreihe, Band 324, Paderborn, 2014 – ISBN 978-3-942647-43-4

Bd. 325 BRANDIS, R.: Systematik für die integrative Konzipierung der Montage auf Basis der Prinziplösung mechatronischer Systeme. Dissertation, Fakultät für Maschinenbau, Universität Paderborn, HNI-Verlagsschriftenreihe, Band 325, Paderborn, 2014 – ISBN 978-3-942647-44-1

Bd. 326 KÖSTER, O.: Systematik zur Entwicklung von Geschäftsmodellen in der Produkt-entstehung. Dissertation, Fakultät für Maschinenbau, Universität Paderborn, HNI-Verlagsschriftenreihe, Band 326, Paderborn, 2014 – ISBN 978-3-942647-45-8

Bd. 327 KAISER, L.: Rahmenwerk zur Modellierung einer plausiblen Systemstrukturen mechatronischer Systeme. Dissertation, Fakultät für Maschinenbau, Universität Paderborn, HNI-Verlagsschriftenreihe, Band 327, Paderborn, 2014 – ISBN 978-3-942647-46-5

Bd. 328 KRÜGER, M.: Parametrische Modellord-nungsreduktion für hierarchische selbstoptimierende Systeme. Dissertation, Fakultät für Maschinenbau, Universität Paderborn, HNI-Verlagsschriftenreihe, Band 328, Pader-born, 2014 – ISBN 978-3-942647-47-2

Bd. 329 AMELUNXEN, H.: Fahrdynamikmodelle für Echtzeitsimulationen im komfortrelevan-ten Frequenzbereich. Dissertation, Fakul-tät für Maschinenbau, Universität Pader-born, HNI-Verlagsschriftenreihe, Band 329, Paderborn, 2014 – ISBN 978-3-942647-48-9

Bd. 330 KEIL, R.; SELKE, H. (Hrsg):. 20 Jahre Lernen mit dem World Wide Web. Technik und Bildung im Dialog. HNI-Verlagsschriftenreihe, Band 330, Pader-born, 2014 – ISBN 978-3-942647-49-6

Bd. 331 HARTMANN, P.: Ein Beitrag zur Verhaltens-antizipation und -regelung kognitiver mechatronischer Systeme bei langfristiger Planung und Ausführung. Dissertation, Fakultät für Wirtschaftswissenschaften, Universität Paderborn, HNI-Verlagsschrif-tenreihe, Band 331, Paderborn, 2014 – ISBN 978-3-942647-50-2

Bd. 332 ECHTERHOFF, N.: Systematik zur Planung von Cross-Industry-Innovationen Dissertation, Fakultät für Maschinenbau, Universität Paderborn, HNI-Verlagsschrif-tenreihe, Band 332, Paderborn, 2014 – ISBN 978-3-942647-51-9

Bd. 333 HASSAN, B.: A Design Framework for Developing a Reconfigurable Driving Simulator. Dissertation, Fakultät für Maschinenbau, Universität Paderborn, HNI-Verlagsschriftenreihe, Band 333, Paderborn, 2014 – ISBN 978-3-942647-52-6

Bd. 334 GAUSEMEIER, J. (Hrsg.): Vorausschau und Technologieplanung. 10. Symposium für Vorausschau und Technologieplanung, Heinz Nixdorf Institut, 20. und 21. Novem-ber 2014, Berlin-Brandenburgische Aka-demie der Wissenschaften, Berlin, HNI-Verlagsschriftenreihe, Band 334, Pader-born, 2014 – ISBN 978-3-942647-53-3

Bd. 335 RIEKE, J.: Model Consistency Management for Systems Engineering. Dissertation, Fakultät für Maschinenbau, Universität Paderborn, HNI-Verlagsschriftenreihe, Band 335, Paderborn, 2014 – ISBN 978-3-942647-54-0

Bd. 336 HAGENKÖTTER S.: Adaptive prozess-integrierte Qualitätsüberwachung von Ultraschalldrahtbondprozessen. Dissertation, Fakultät für Elektrotechnik, Informatik und Mathematik, Universität Paderborn, HNI-Verlagsschriftenreihe, Band 336, Paderborn, 2014 – ISBN 978-3-942647-55-7

Bd. 337 PEITZ, C.: Systematik zur Entwicklung einer produktlebenszyklusorientierten Geschäftsmodell-Roadmap. Dissertation, Fakultät für Maschinenbau, Universität Paderborn, HNI-Verlagsschrif-tenreihe, Band 337, Paderborn, 2015 – ISBN 978-3-942647-56-4